

The Equilibrium Structure of CDM Halos

Paul R. Shapiro[‡], Ilian T. Iliev[‡], Hugo Martel[‡], Kyungjin Ahn[†], and Marcelo A. Alvarez[†]

June 23, 2021

Abstract

Dark-matter (DM) halos are the scaffolding around which galaxies and clusters are built. They form when the gravitational instability of primordial density fluctuations causes regions which are denser than average to slow their cosmic expansion, recollapse, and virialize. Understanding the equilibrium structure of these halos is thus a prerequisite for understanding galaxy and cluster formation. Numerical N-body simulations of structure formation from Gaussian-random-noise initial conditions in the Cold Dark Matter (CDM) universe find a universal internal structure for halos. Objects as different in size and mass as dwarf spheroidal galaxies and galaxy clusters are predicted to have halos with the same basic structure when properly rescaled, independent of halo mass, of the shape of the power spectrum of primordial density fluctuations, and of the cosmological background parameters. This remarkable universality is a fundamental prediction of the CDM model, but our knowledge is limited to the “empirical” N-body simulation results, with little analytical understanding. We summarize here our attempts to fill this gap, in an effort to derive and give physical insight to the numerical results and extend them beyond the range of numerical simulation: (1) Simulated halos which form from highly simplified initial conditions involving gravitational instability in a cosmological pancake show that many of the universal properties of CDM halos are generic to cosmological gravitational collapse and do not require Gaussian-random-noise density fluctuations or hierarchical clustering. (2) A fluid approximation derived from the Boltzmann equation yields an analytical theory of halo dynamics which can explain many of the N-body results if the complex mass assembly history of individual halos is approximated by continuous spherical infall. The universal mass growth history reported for CDM N-body halos corresponds to a time-varying infall rate which self-consistently determines the shape of the equilibrium halo profile and its evolution without regard for the complicated details of the merger process. (3) The first fully-cosmological, similarity solutions for halo formation in the presence of collisionality provide an analytical theory of the effect of the

*Department of Astronomy, University of Texas, Austin, 78712, US

†Canadian Institute for Theoretical Astrophysics, University of Toronto, 60 St. George Street, Toronto, ON M5S 3H8, Canada

‡Département de physique, de génie physique et d’optique, Université Laval, Sainte-Foy, QC G1K 7P4, Canada

self-interacting dark matter (SIDM) hypothesis on CDM halo density profiles. Collisions transport heat inward which flattens the central cusp, but continuous infall pumps energy into the halo to stabilize the core against gravothermal catastrophe. (4) The postcollapse equilibrium halo structure derived by matching spherical top-hat collapse to a unique, minimum-energy solution of the isothermal Lane-Emden equation – the Truncated Isothermal Sphere (TIS) model – reproduces well the average properties of simulated CDM halos. The TIS yields a universal, self-similar equilibrium structure whose parameters are determined by the halo’s total mass and collapse redshift. These latter two parameters are statistically correlated, however, since halos of the same mass form on average at the same epoch, with small-mass objects forming first and then merging hierarchically to form larger-mass objects. The structural properties (e.g. sizes, mass profiles, velocity dispersions and virial temperatures) of dark-matter dominated halos of different masses, therefore, should reflect this statistical correlation, an imprint of the statistical properties of the primordial density fluctuations which formed them. When combined with the Press-Schechter (PS) formalism, the TIS model can predict these statistical correlations of halo properties analytically, which we compare to observational data on these correlations, providing a fundamental test of the CDM model, which probes the shape of the power spectrum of primordial density fluctuations and the cosmological background parameters. (5) For observational tests which are sensitive to the shape of the inner mass profile at the very center, the TIS model provides a convenient analytical tool for studying the effect of a small nonsingular core on CDM halo predictions. As an example, strong gravitational lensing properties of CDM halos with nonsingular cores are contrasted with those with singular, cuspy cores.

1 Introduction

Numerical N-body simulations of structure formation in the Cold Dark Matter (CDM) universe show a cosmic web of lumps, filaments, and sheets. This web evolves in a self-similar way, with smaller mass structures forming first and merging to form larger-mass structures later, in a continuous sequence of mass assembly. At each epoch, the web produces gravitationally-bound, quasi-spherical “halos” in virial and hydrostatic equilibrium. These virialized halos are the sites of galaxy and cluster formation. Their universal equilibrium structure is a fundamental prediction of the CDM model, but our knowledge is limited to the numerical N-body results, with very little analytical understanding. We shall describe our attempts to fill this gap in what follows.

Most of the progress to date on the formation and evolution of virialized, dark-matter dominated halos in a CDM universe has been via numerical N-body simulations of collisionless dark matter involving Gaussian random noise initial conditions. According to those N-body simulations, the spherically-averaged mass distribution inside halos is universal, with a density profile which declines with radius, approaching $\rho \propto r^{-3}$ at large radii, flattening near the center to $\rho(r) \propto r^{-\alpha}$ with $\alpha < 2$. Two

“universal” profiles bracket the results (NFW, [108]; Moore, [100]). The NFW (Moore) profile has an inner density profile $\rho \propto r^{-1}(r^{-1.5})$. The actual value of α is still uncertain, even though the N-body results have advanced to the point of including millions of simulation particles within the virial radius of a given halo (e.g. [54, 55, 56, 58, 74, 75, 81, 112]). Since the true inner profile may not be a power-law, comparisons of the inner slope for different simulation results are typically referred to a particular radius (e.g. $r = 0.01r_{\text{vir}}$, where r_{vir} is some measure of the outer radius of the virialized region). The N-body results generally support the conclusion that the same halo density profile applies to objects as different as dwarf galaxies and galaxy clusters, independent of halo mass, of the shape of the density fluctuation power spectrum, and of the background cosmology. This universality is apparent when comparisons of different halo profiles are made with density expressed in units of the density $\rho_{-2} \equiv \rho(r_{-2})$ at the radius r_{-2} at which each profile has a logarithmic slope of -2 , while radii for each halo are expressed in units of r_{-2} [109]. An exception to this universality is claimed by [119], who reports that the value of α depends upon halo mass, shallower for dwarf galaxies than for clusters, reflecting the different slopes of the power spectrum at the different scales represented by these objects, but [33] has challenged this claim.

Much attention has been focused on the N-body results for this inner slope, since the observed rotation curves of dark-matter dominated dwarf and low surface brightness (LSB) disk galaxies tend to favor mass profiles with a flat-density core unlike the singular profiles of the CDM N-body simulations (e.g. [37, 38, 51, 98, 131]; but, for a different view, see also [138, 139]). On the cluster scale, too, there is some evidence from observations of strong gravitational lensing of background galaxies by foreground clusters which favors a flatter inner halo density profile than is found by the CDM N-body simulations (e.g. [57, 123, 146]; but see also [34]). However, the halo mass fraction contained within the disputed inner cusp is actually quite small, so there may yet be dynamical processes not fully accounted for in the pure N-body simulations which can affect this small central mass without disturbing the overall universality of the rest of the profile.

Along with their universal mass profiles, CDM N-body halos also exhibit several universal properties in their phase-space distributions. Over most of the halo volume inside the virial radius, the DM particles are approximately isothermal – i.e. their velocity dispersion is fairly constant with radius – with only a relatively small dip in “temperature” toward the center (e.g. [52, 144]). Halo particle velocities are also approximately isotropic, with only a mild radial bias in the outer halo, which gives way to increasing isotropy toward the center (e.g. [27, 31, 43, 54]). The spherically-averaged mass motion at each radius is quite small and “subsonic;” the halo is not only in a state of global virial equilibrium but is close to hydrostatic equilibrium at each radius, too – i.e. it satisfies the spherical Jeans equation (e.g. [144]).

Individual halos in CDM N-body simulations evolve over time, on average, through a continuous sequence of universal-shaped mass profiles of increasing to-

tal mass [141, 149, 150]. This Lagrangian mass evolution can be characterized by a universal mass accretion history: $M(a)/M(a_f)$, where a is the cosmic scale factor and a_f is some particular value of a , such as that at which $d \ln M / d \ln a = 2$ [150]. As the mass of each halo grows with time due to the average effect of mergers and smooth infall, so does the concentration parameter c of its density profile, where $c \equiv r_{\text{vir}}/r_{-2}$, roughly as $c(a)/c(a_f) \propto a/a_f$ for $a/a_f > 1$ [150], after hovering at low values $c \leq 3 - 4$ during the initial phase of most rapid mass assembly prior to a_f [141].

This description of the CDM halos of N-body simulations is a spherically-averaged one, which neglects many details. There is some scatter in the N-body results about this average description, of course. Individual halos are not truly spherically symmetric, either, but only approximately so. The neglect of net angular momentum is probably not a bad first approximation, since the specific angular momentum is typically found to be far below that required for rotational support (e.g. [12, 22])¹. However, the spherically-averaged description also averages out the small-scale density inhomogeneities inside each halo. This small-scale inhomogeneity may play an important role in the underlying dynamics which leads to halo formation and evolution in these N-body simulations. Regardless of its dynamical significance, this halo substructure has also been the subject of special attention for its own sake, once it was noticed that the number of subhalos which typically survive their merger into a larger halo in the N-body results is much larger than the number of galaxies observed within the Local Group (e.g. [80, 101]).

While N-body simulations have made the universal equilibrium structure of halos described above a fundamental prediction of the CDM model, much less progress has been made on the analytical side, to derive and understand the numerical results and extend them beyond the range of numerical simulation. Our purpose in what follows is to summarize our own attacks on this problem by a hierarchy of approximations, each one simpler than the last, from 3D gas and N-body simulations of halo formation involving simplified initial conditions (§2), to 1D, spherically-symmetric, dynamical models involving a fluid approximation derived from the Boltzmann equation (§3), to a model for the hydrostatic equilibrium of halos which follows from the virialization of top-hat density perturbations (§4). As we shall see, the last of these, known as the Truncated Isothermal Sphere (TIS) model, not only provides an excellent match to many of the average properties of the halos found by the N-body simulations of CDM from realistic initial conditions, but one which is conveniently coupled to the Press-Schechter formalism for the mass function of halos in CDM to predict the observed statistical properties of galaxies and clusters analytically. We summarize several such applications of this model in §4.3. In §5, motivated by the prospect that gravitational lensing will provide a direct observational test of

¹The specific angular momentum profile, $j(M)$, of individual CDM halos averaged over spherical shells encompassing mass M , also has a universal shape, which has been fitted by $j(M) \propto M^s$ with $s = 1.3 \pm 0.3$ [23].

the CDM halo density profile, we use the analytical theory of the TIS halo, with its small, flat-density core at the center of a halo which otherwise closely resembles the average CDM halos of N-body simulations, to contrast the lensing properties of nonsingular and singular CDM halos.

2 N-body Halos from Simplified Initial Conditions: 3D Halo Formation by Gravitational Instability of Cosmological Pancakes

A natural question which emerges from the results of N-body simulations of structure formation in CDM is whether the universal properties of dark matter halos, like their density profiles and mass accretion histories, are a consequence of hierarchical clustering from Gaussian-random-noise density fluctuations or are in fact more general. To address this question, we have analyzed the results of simulations with initial conditions that are much simpler than a CDM power spectrum with Gaussian-random-noise, while retaining the realistic features of continuous and anisotropic infall in three dimensions. Each simulation forms a single halo from the gravitational instability of a cosmological pancake. Because we focus on one halo at a time, we are able to follow its formation and evolution, and find that several of the trends reported for halo evolution in the CDM simulations are also present in the simplified pancake model. Thus, the pancake instability model serves as a convenient test-bed for halo formation which shares not only similar boundary conditions with more realistic models of halo formation, but also produces halos that have similar structural and evolutionary properties. Some of this work was summarized previously in [5, 6, 7].

2.1 Halo Formation via Pancake Instability

2.1.1 Unperturbed Pancake

Consider the growing mode of a single sinusoidal plane-wave density fluctuation of comoving wavelength λ_p and dimensionless wavevector $\mathbf{k}_p = \hat{\mathbf{x}}$ (length unit = λ_p) in an Einstein-de Sitter universe dominated by cold, collisionless dark matter [130]. Let the initial amplitude δ_i at scale factor a_i be chosen so that the first density caustic forms in the collisionless component at scale factor $a = a_c = a_i/\delta_i$.

2.1.2 Perturbations

Pancakes modeled in this way have been shown to be gravitationally unstable, leading to filamentation and fragmentation during the collapse [148]. As an example, we shall perturb the 1D fluctuation described above by adding to the initial primary pancake mode two transverse, plane-wave density fluctuations with equal wavelength

Figure 1: Dark matter particles at $a/a_c = 3$. (see jpg file)

$\lambda_s = \lambda_p$, wavevectors \mathbf{k}_s pointing along the orthogonal unit vectors $\hat{\mathbf{y}}$ and $\hat{\mathbf{z}}$, and smaller initial amplitudes, $\epsilon_y \delta_i$ and $\epsilon_z \delta_i$, respectively, where $\epsilon_y \ll 1$ and $\epsilon_z \ll 1$. A pancake perturbed by two such density modes will be referred to as $S_{1,\epsilon_y,\epsilon_z}$. All results presented here refer to the case $S_{1,0.2,0.2}$. The initial position, velocity, density, and gravitational potential are given by

$$r_l = q_l + \frac{\delta_i \epsilon_l}{2\pi k_p} \sin 2\pi k_p q_l \quad (1)$$

$$v_l = \frac{\epsilon_l}{2\pi k_p} \left(\frac{d\delta}{dt} \right)_i \sin 2\pi k_p q_l \quad (2)$$

$$\rho = \frac{\bar{\rho}}{1 + \delta_i (\cos 2\pi k_p q_x + \epsilon_y \cos 2\pi k_p q_y + \epsilon_z \cos 2\pi k_p q_z)}, \quad (3)$$

and

$$\phi = \langle \phi \rangle (\cos 2\pi k_p x + \epsilon_y \cos 2\pi k_p y + \epsilon_z \cos 2\pi k_p z), \quad (4)$$

where $l \equiv x, y, \text{ or } z$, $\epsilon_x \equiv 1$, q_x, q_y , and q_z are the unperturbed particle positions, and $\bar{\rho}$ is the cosmic mean matter density.

Such a perturbation leads to the formation of a quasi-spherical mass concentration in the pancake plane at the intersection of two filaments (Fig. 1).

2.2 N-body and Hydrodynamical Simulations

The code we use to simulate the formation of the halo couples the Adaptive SPH (ASPH) algorithm, first described in [111, 129], to a P³M gravity solver. The ASPH method improves on standard SPH by introducing nonspherical, ellipsoidal smoothing kernels to better track the anisotropic flow that generally arises during cosmological structure formation. Two simulations were carried out, one with gas and one without. In both cases, there were 64^3 particles of dark matter, while there were also 64^3 gas particles when gas was included. The P³M grid was 128^3 cells in a periodic cube size λ_p on a side, with a comoving softening length of $r_{\text{soft}} = 0.3\Delta x = 0.3\lambda_p/128$, where Δx is the cell size. The initial conditions were those described in § 2.1.2.

The adiabatic pancake problem (i.e. without radiative cooling) is self-similar and scale-free, once distance is expressed in units of the pancake wavelength λ_p and time is expressed in terms of the cosmic scale factor a in units of the scale factor a_c at which caustics first form in the dark matter and shocks in the gas [130] In the currently-favored, flat, cosmological-constant-dominated universe, however, this self-similarity is broken because Ω_M/Ω_Λ decreases with time, where Ω_M and Ω_Λ are the matter and vacuum energy density parameters, respectively. For objects which collapse at high redshift in such a universe (e.g. dwarf galaxies), the Einstein-de Sitter results are still applicable as long as we take $(\Omega_B/\Omega_{\text{DM}})_{\text{EdS}} = (\Omega_B/\Omega_{\text{DM}})_\Lambda$, where Ω_B and Ω_{DM} are the baryon and dark matter density parameters. If $\Omega_B = 0.045$, $\Omega_{\text{DM}} = 0.255$, and $\Omega_\Lambda = 0.7$ at present, then the EdS results are applicable if we take $\Omega_B = 0.15$ and $\Omega_{\text{DM}} = 0.85$, instead.

2.3 Profiles

2.3.1 Density

The density profiles at different epochs for the simulations without gas are shown in Fig. 2, along with the best-fitting NFW profile for each epoch, which has the form

$$\frac{\rho}{\bar{\rho}} = \frac{\delta_c}{(r/r_s)(1+r/r_s)^2}, \quad (5)$$

with δ_c given by

$$\delta_c = \frac{200}{3} \frac{c^3}{\ln(1+c) - c/(1+c)}, \quad (6)$$

where $r_s \equiv r_{-2}$, $c = r_{200}/r_s$, and r_{200} is the radius within which the mean density $\langle \rho \rangle = 200\bar{\rho}$. The NFW profile has only one free parameter, the concentration parameter c . Our pancake halo density profiles have concentrations which range from 3 to 15, increasing with time, and are usually within 20% of the best-fit NFW profile at all radii. This NFW profile is a fit to N-body results for CDM halos, but it is also consistent with the halos which form in simulations using Gaussian-random-noise

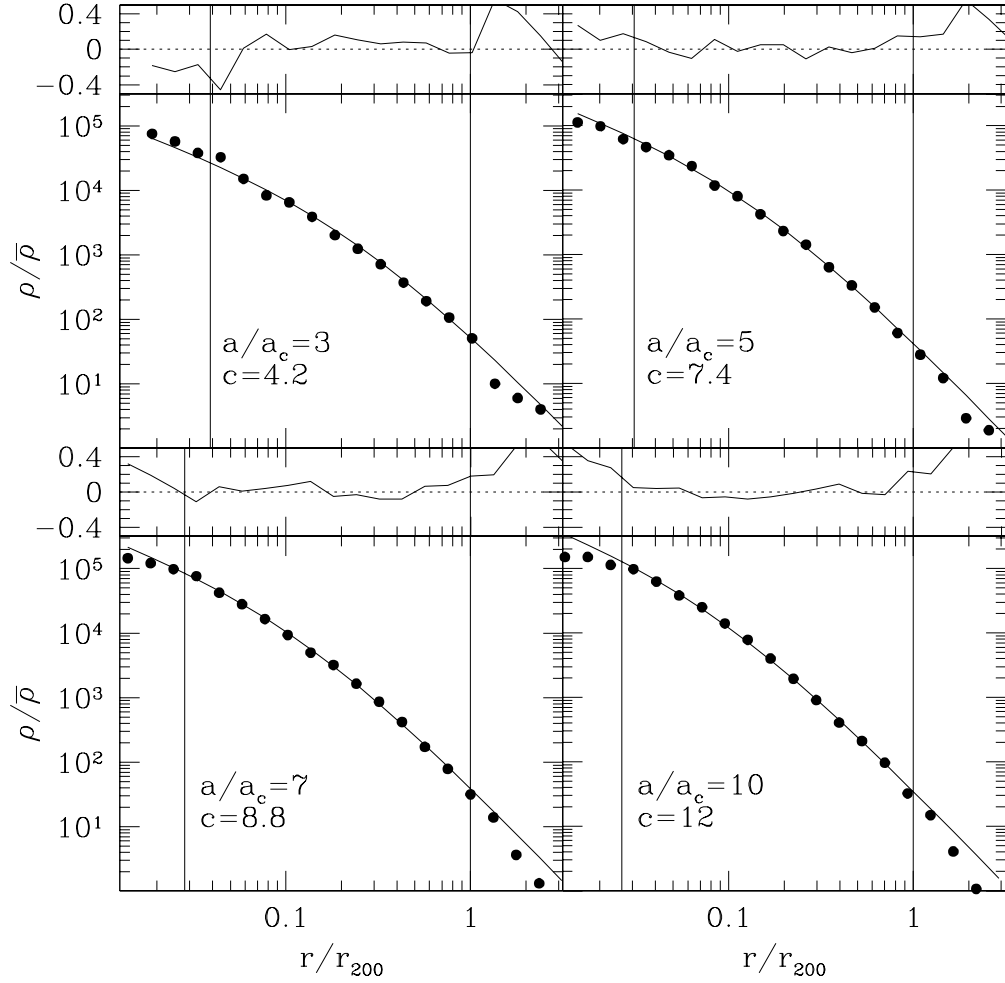


Figure 2: Density profile of the dark matter halo as simulated without gas at four different scale factors, $a/a_c = 3, 5, 7,$ and 10 , with spherically-averaged simulation results in radial bins (filled circles) and the best-fitting NFW profiles (solid curves) for several epochs, as labeled. Shown above each panel are fractional deviations $(\rho_{\text{NFW}} - \rho)/\rho_{\text{NFW}}$ from the best-fitting NFW profiles for each epoch. Vertical lines indicate the location of r_{soft} , the numerical softening-length, and r_{200} .

initial fluctuations with small-scale fluctuations suppressed [8, 18, 32, 67, 82], as is the case for the halos that form from pancake instability presented here.

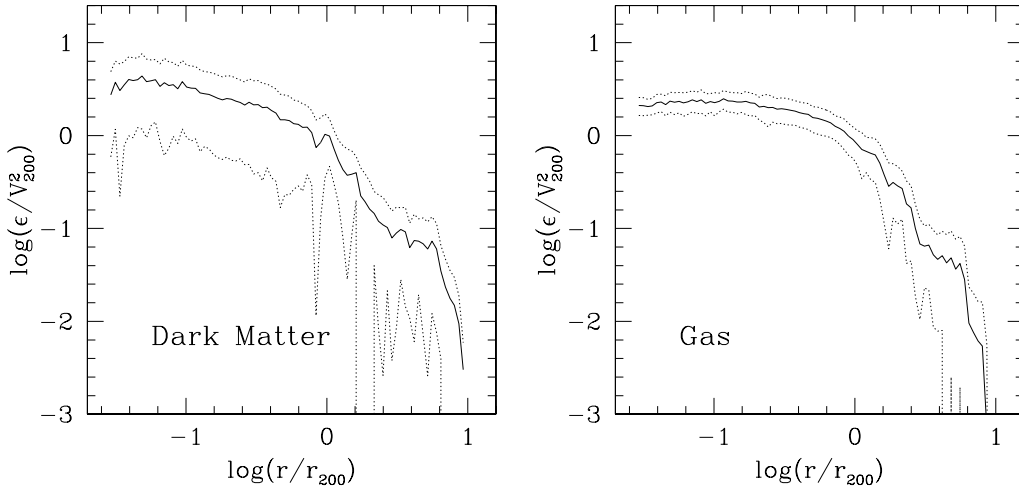


Figure 3: Dimensionless specific thermal energy profiles at $a/a_c = 7$ in the (gas+DM)-simulation, for the dark matter (left) and gas (right), with dotted lines indicating the rms scatter within each logarithmic bin.

2.3.2 Kinetic and Thermal Energy

The profiles of the dimensionless specific thermal kinetic energy $\epsilon_{\text{DM}} = \langle |\mathbf{v} - \langle \mathbf{v} \rangle|^2 \rangle / 2 = 3\sigma_{\text{DM}}^2/2$ of the dark matter and the dimensionless specific thermal energy $\epsilon_{\text{gas}} = 3k_{\text{B}}T/2m$ of the gas are shown in Fig. 3, for the simulation with gas and dark matter at $a/a_c = 7$. Although the dark matter velocity dispersion rises towards the center, the rise is shallow and the kinetic energy distribution is approximately isothermal inside the radius r_{200} . As seen from Fig. 3, the gas is even more isothermal than the dark matter, with $\epsilon_{\text{gas}}(r_{\text{soft}})/\epsilon_{\text{gas}}(r_{200}) \simeq 2.5$, while the density varies by more than three orders of magnitude over the same region. In Fig. 4 we show the ratio of the specific thermal energy of the dark matter to that of the gas. This ranges from $\epsilon_{\text{DM}}/\epsilon_{\text{gas}} \sim 1.6$ in the center to $\epsilon_{\text{DM}}/\epsilon_{\text{gas}} \sim 1$ at r_{200} .

2.3.3 Velocity Anisotropy

In Fig. 4, we plot the profile of the anisotropy parameter β , defined two different ways, according to the frame of reference in which the velocity dispersion is calculated. In the Eulerian case, where the bulk motion of the shell contributes to the anisotropy, it is defined as $\beta = \beta_{\text{E}} \equiv 1 - \langle v_t^2 \rangle / (2\langle v_r^2 \rangle)$. In the Lagrangian case, however, the bulk motion of the shell is subtracted out, $\beta = \beta_{\text{L}} \equiv 1 - \sigma_t^2 / (2\sigma_r^2)$, where $\sigma_t^2 = \langle (v_i - \langle v_i \rangle)^2 \rangle$. Because of the symmetry of the pancake initial conditions, $\langle v_t^2 \rangle = \sigma_t^2$ at all times. Differences between the two definitions therefore arise because of differences in the radial component. The values $\beta = 1, 0$, and $-\infty$

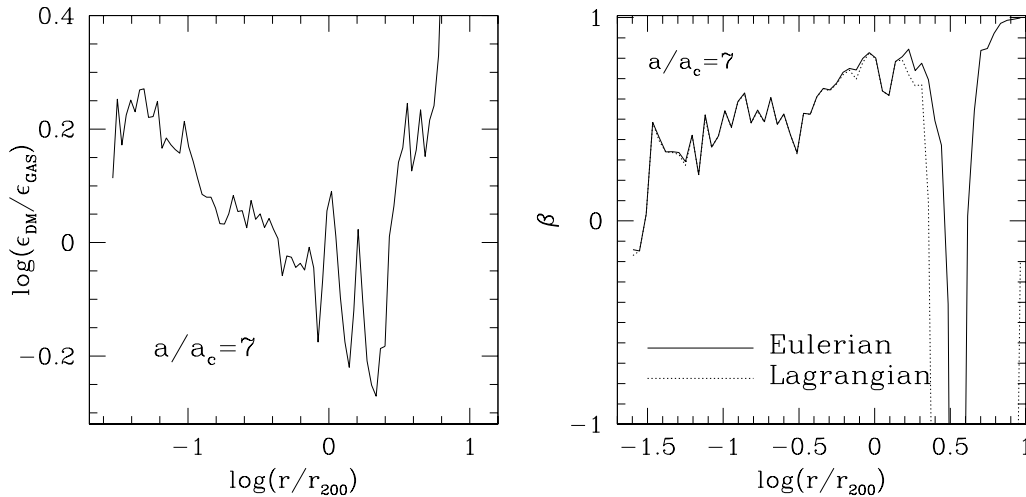


Figure 4: (left) Ratio of dimensionless specific thermal energy profiles at $a/a_c = 7$ in the (gas+DM)-simulation. (right) Anisotropy profile, defined two different ways, at $a/a_c = 7$. The curves are labeled according to the definitions given in the text.

correspond to motion which is purely radial, fully isotropic, and tangential, respectively. While the two definitions of anisotropy give nearly indistinguishable profiles at $r \leq r_{200}$, the two profiles depart significantly at $r > r_{200}$. This is expected, since the bulk radial motion is nearly zero inside the halo where equilibrium is a reasonable expectation. The two definitions of β are identical when the system is in equilibrium. Outside the halo, however, equilibrium is violated because the bulk radial motion is not zero, and the difference between the profiles arises due to the detailed nature of the region outside the halo.

Simulations of CDM typically find values of β near 0 at the center, slowly rising to a value of $\beta \approx 0.5$ at r_{200} [27, 31, 43, 54]. As seen from Fig. 4, the halo formed by pancake instability is more anisotropic, with values of β rising from ~ 0.2 near the center to ~ 0.8 at r_{200} . This reflects the strongly filamentary substructure of the pancake within which the halo forms, and perhaps the absence of strong tidal fields or mergers as well, which might otherwise help convert radial motions into tangential ones.

2.4 Virial Equilibrium

A state of equilibrium is commonly assumed in analytical modeling of dark matter halos [92]. Using N -body simulations, [144] found that halos which formed from CDM initial conditions roughly obey the Jeans equation for dynamical equilibrium in spherical symmetry, within a radius of order r_{200} , suggesting that CDM halos are in approximate virial equilibrium. In what follows, we will interpret the numerical

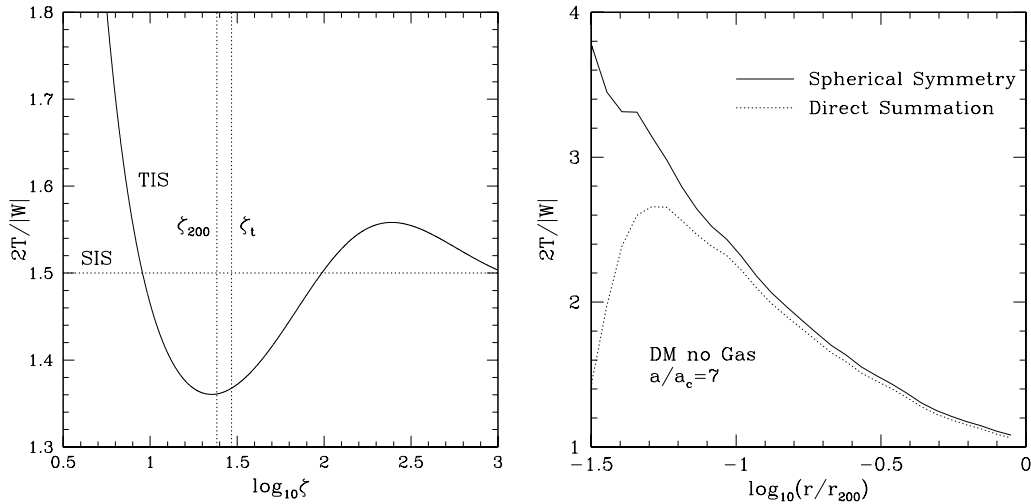


Figure 5: (left) Virial ratio versus dimensionless radius ζ for the TIS solution. The vertical dotted line on the right corresponds to the truncation radius, ζ_t , at which the total energy is a minimum at fixed mass and boundary pressure, while the one on the left corresponds to the radius within which the mean density is 200 times the background density. The horizontal dotted line is the virial ratio of the singular isothermal sphere. (right) Virial ratio vs. radius calculated two different ways: (1) direct summation and (2) assuming spherical symmetry.

halo results further by comparison with equilibrium halo models.

2.4.1 Virial Ratio

The scalar virial theorem states that for a self-gravitating system in static equilibrium ($\langle v \rangle = 0$) with no magnetic fields, $2\mathcal{T} + W + S_p = 0$, where W is the potential energy, \mathcal{T} is the thermal and kinetic energy, and S_p is a surface pressure term,

$$S_p = - \int p \mathbf{r} \cdot d\mathbf{S}, \quad (7)$$

where $d\mathbf{S}$ is the surface area element. If the system is isolated, there can be no material outside to create a boundary pressure, and we have $S_p = 0$, implying $2\mathcal{T}/|W| = 1$. Cosmological halos are not isolated systems, however, so we cannot expect $S_p = 0$ and $2\mathcal{T}/|W| = 1$. In fact, the presence of infalling matter creates a flux of momentum into the halo which can act as a surface pressure (even for collisionless matter) in the virial theorem. With infall present, we therefore expect $S_p/|W| < 0$, implying $2\mathcal{T}/|W| > 1$.

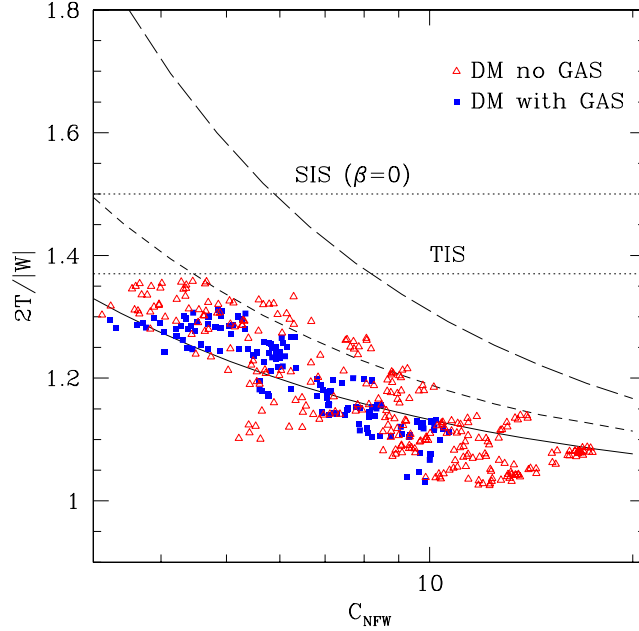


Figure 6: Virial ratio versus NFW concentration parameter for the halos as simulated with and without gas, as they evolve. Solid, dashed, and long-dashed lines represent expected values for $\beta = 0, 0.5, 1$, respectively. Shown also are the values corresponding to the simulated halos, the isotropic singular isothermal sphere (SIS), and the truncated isothermal sphere (TIS).

2.4.2 Singular Isothermal Sphere

The singular isothermal sphere (SIS) is the singular solution of the equation of hydrostatic equilibrium with uniform temperature. The density is given by

$$\rho(r) = \frac{\sigma_0^2}{2\pi G r^2} = \frac{k_B T}{2\pi G m r^2}, \quad (8)$$

where σ_0 is the 1D velocity dispersion, and T is the gas temperature. A more general class of solutions can be found, however, by allowing the anisotropy parameter β to be nonzero but remain independent of radius. The relevant equation is the Jeans equation [16],

$$\frac{d}{dr}(\rho \overline{v_r^2}) + \frac{2\rho\beta \overline{v_r^2}}{r} = -\rho \frac{d\Phi}{dr}, \quad (9)$$

where the anisotropy parameter is now the ‘‘Eulerian’’ quantity, $\beta = \beta_E$, as defined in §2.3. We can solve the Jeans equation in this case for the velocity dispersion σ_β as a function of β and the isotropic velocity dispersion σ_0 for the same mass

distribution as in equation (8), to show

$$\sigma_\beta^2 = \frac{3 - 2\beta}{3(1 - \beta)} \sigma_0^2. \quad (10)$$

If the anisotropy β does not vary with radius, we can determine the virial ratio of an SIS for a given value of the anisotropy, as follows. The potential energy at r is

$$W(r) = \int (\rho\phi) dV = -2M(r)\sigma_0^2. \quad (11)$$

The kinetic (or thermal) energy \mathcal{T} is given by

$$\mathcal{T} = \frac{1}{2} \int \rho \langle v^2 \rangle dV = \frac{3}{2} \int \rho \sigma^2 dV = \frac{3}{2} M(r) \sigma^2. \quad (12)$$

Using equation (10) to relate the actual σ^2 to the one in the isotropic case σ_0^2 , one obtains

$$\mathcal{T} = \frac{3 - 2\beta}{2(1 - \beta)} M \sigma_0^2. \quad (13)$$

The virial ratio is therefore

$$\frac{2\mathcal{T}}{|W|} = \frac{3 - 2\beta}{2(1 - \beta)}. \quad (14)$$

2.4.3 Nonsingular Truncated Isothermal Sphere

The Truncated Isothermal Sphere (TIS) model for the equilibrium halos which form from the collapse and virialization of top-hat density perturbations [128] (to be discussed here in §4) yields a virial ratio which differs significantly from the familiar value of $2\mathcal{T}/|W| = 1$ for isolated halos (i.e. with zero boundary pressure) with $\beta = 0$. The TIS model is the minimum energy solution of the isothermal Lane-Emden equation with non-singular, finite boundary condition for the central density. Since the TIS is a unique solution given by the minimum energy at fixed boundary pressure, the virial ratio is always the same value, namely $2\mathcal{T}/|W| \simeq 1.37$ at $\zeta_t = 29.4$, where ζ_t is the truncation radius in units of the core radius. This value is smaller than that for the isotropic singular isothermal sphere (with nonzero boundary pressure), $2\mathcal{T}/|W| = 1.5$, and is near the global minimum for all values of ζ , which is $2\mathcal{T}/|W| \simeq 1.36$ and occurs at $\zeta \simeq 22.6$. At the intermediate radius $\zeta_{200} \simeq 24.2$, defined to be the radius within which the mean density is 200 times the background density, the TIS virial ratio has a value $2\mathcal{T}/|W| \simeq 1.36$. As seen in Fig. 5, the inner core region of the TIS is dominated by kinetic (or thermal, in the gas case) energy, whereas the value approaches that of the SIS at large ζ , where the core region becomes small compared with the size of the TIS and the density profile asymptotically approaches that for the SIS ($\rho \propto r^{-2}$).

2.4.4 NFW Halos

The equilibrium structure of halos with an NFW density profile was investigated by [92]. Using different values of $\beta(r)$, they found several analytical solutions to the velocity dispersion of the halo by integrating the Jeans equation for a given $\rho(r)$ and $\beta(r)$. In order to integrate the Jeans equation to find the velocity dispersion, it is necessary to set the velocity dispersion at some r . In the absence of a physical value for σ_r at the boundary of the halo, as could be inferred from some infall solution, the only other reasonable choice is to have $\sigma_r \rightarrow 0$ as $r \rightarrow \infty$. The results obtained by fixing $\sigma_r = 0$ at infinity should reflect the general trends associated with a single halo evolving in a quasi-equilibrium state.

Shown in Fig. 6 is the virial ratio versus concentration parameter for different values of $\beta(r) = \beta_0$, as expected from the Jeans equation. The more isotropic the NFW halo, the lower the virial ratio. This is consistent with the fact that the surface pressure term is directly related to the radial velocity dispersion. The more concentrated the NFW halo, the lower the virial ratio. This is expected, since the more isolated a halo, the less relative importance of the boundary pressure, implying $2\mathcal{T}/|W| \rightarrow 1$.

2.4.5 Simulated Pancake Instability Halos

Virial ratios $2\mathcal{T}/|W|$ were calculated for both simulation runs, with and without gas. For the case with no gas,

$$\mathcal{T}(r) = \sum_i \frac{1}{2} m_i v_i^2, \quad (15)$$

where the sum is over all particles within r . For the simulation with gas included,

$$\mathcal{T}(r) = \sum_i \frac{1}{2} m_i v_i^2 + \sum_i \frac{3}{2} m_i k_B T_i. \quad (16)$$

The potential energy was found using the assumption of spherical symmetry,

$$W(R) = - \sum_i \frac{GM_i m_i}{r_i} f_i, \quad (17)$$

where M_i is the mass interior to r_i and $f_i \equiv f(r_i)$ is a function which represents the particular form of the softening used in the P³M algorithm, and the sum is over all particles within R . As shown in Fig. 5, the assumption of spherical symmetry yields results which are very close at $R = r_{200}$ to those arrived at from the more rigorous definition,

$$W(R) \equiv -\frac{1}{2} \sum_i \sum_j \frac{Gm_i m_j}{r_{ij}} f_{ij}, \quad (18)$$

where $r_{ij} = |\mathbf{r}_i - \mathbf{r}_j|$ and $f_{ij} \equiv f(r_{ij})$.

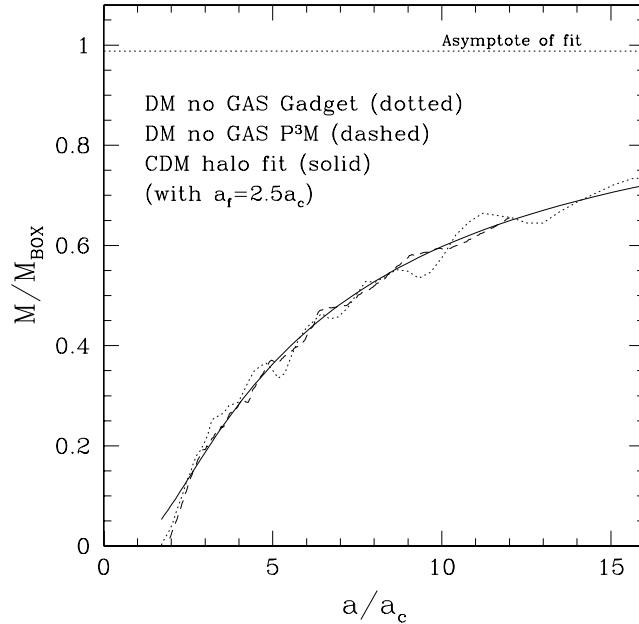


Figure 7: Mass accretion history of simulation with dark matter only (dashed) along with the best-fit functional form from CDM simulations by [150] (solid) with $S = 2$ and $a_f = 2.5a_c$ (see equation 19). Curve labeled “Gadget” was for the same initial conditions, run with the publicly available code of the same name [136].

Shown in Fig. 6 are the virial ratios of both halos, with and without gas, plotted versus their concentration parameter. Each point corresponds to a different time in the halo’s evolution, since the concentration of each halo changes with time. While the simulated halos lie below the expected curve for NFW halos of comparable anisotropy, the trend of smaller virial ratios for more concentrated halos is clearly evident, though there is significant scatter, particularly in the simulation without gas included.

2.5 Halo Evolution

2.5.1 Mass Accretion History

The mass growth of the halo proceeds in three stages (Figs. 7 and 8). Before $a/a_c \sim 3$, the mass within r_{200} grows very quickly, indicating initial collapse of the central overdensity. After $a/a_c \sim 3$, the infall rate drops, and can be well-described by $M \propto a$. Such an infall rate is reminiscent of self-similar spherical infall onto a point mass (e.g. [14]). This infall rate cannot persist indefinitely, since there is only a finite mass supply to accrete onto the halo because of the periodic boundary

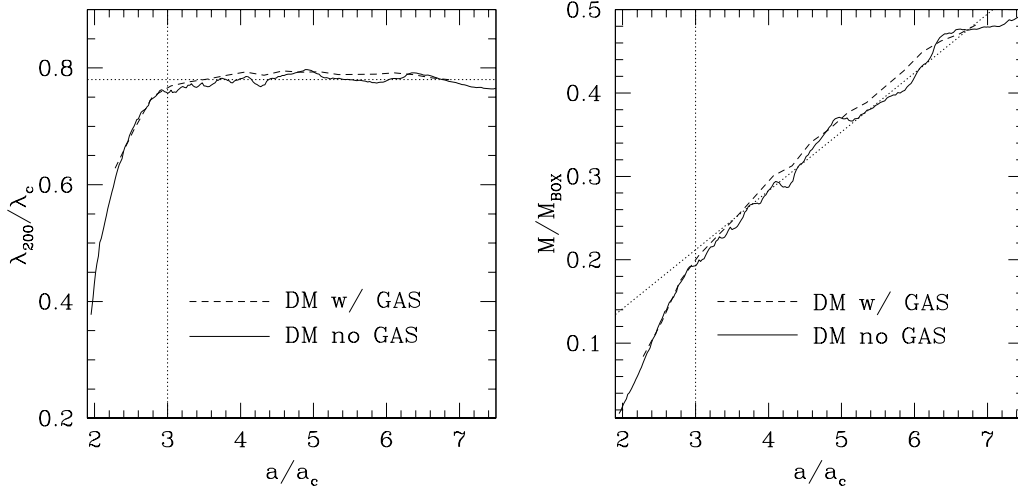


Figure 8: Evolution of the dark matter only halo in the intermediate (self-similar) regime. (left) Virial radius in units of expected caustic radius as defined in the text, and the average in the range $3 < a/a_c < 7.5$ (horizontal dotted line). (right) Halo mass and the linear best-fit (dotted). The vertical dotted lines indicate the virialization epoch at $a = 3a_c$.

conditions. As a consequence, the accretion rate slows after $a/a_c = 7$. This is also expected to occur in halos forming from more realistic initial conditions, given that neighboring density peaks of a similar mass scale prevent any one halo from having the infinite mass supply necessary to sustain this mass accretion rate. In fact, as shown in Fig. 7, the halo can be fit at nearly all times, especially later, by the more general fitting function

$$M(a) = M_\infty \exp[-Sa_f/a], \quad (19)$$

where $S \equiv [d \ln M / d \ln a]_{a_f}$ is the logarithmic slope at $a = a_f$. For $S = 2$, we find a best-fit value of $a_f = 2.5a_c$. This form was first used to fit the evolution of halos formed in CDM simulations ([150]) We have identified three distinct phases in the halo evolution: initial collapse, steady infall, and infall truncation due to finite mass supply. In realistic collapse, we see that the halo evolves continuously from one stage to the next as evidenced by the continuous change in logarithmic slope of the fitting function, given by

$$\frac{d \ln M}{d \ln a} = S \frac{a_f}{a}. \quad (20)$$

In the intermediate stage of collapse, the resemblance to self-similar spherical infall onto a point-mass perturbation is evident in (Fig. 8 and 9). Plotted in Fig. 9 is the dark matter radial dimensionless velocity profile $V(\lambda)$ for different a/a_c as

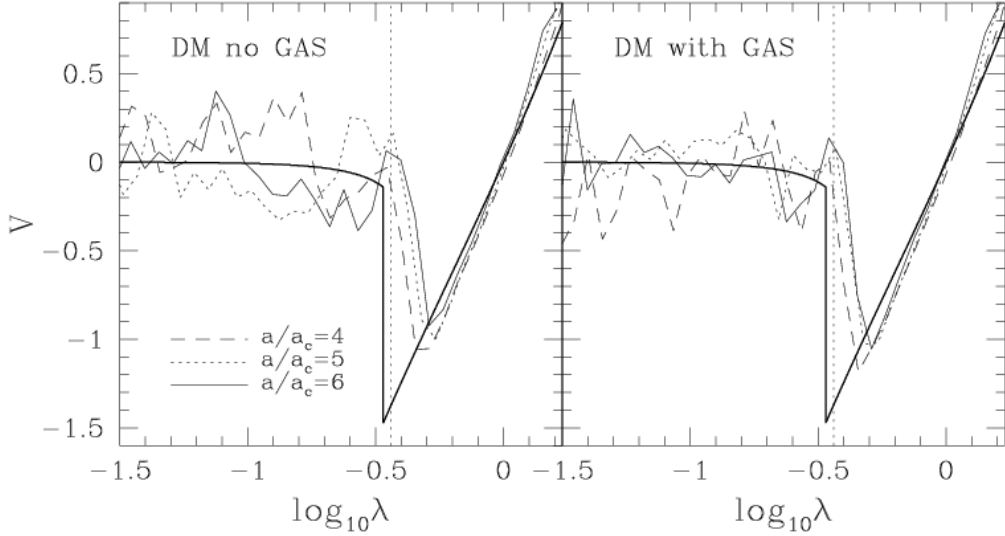


Figure 9: Radial velocity profiles in dimensionless units as in self-similar spherical collapse. The thick solid line is the radial velocity profile for an ideal $\gamma = 5/3$ gas as in [14].

simulated with and without gas. The dimensionless velocity is

$$V \equiv \frac{t}{r_{\text{ta}}(t)} v_r = \frac{2}{3H_7} \left(\frac{a}{a_7} \right)^{1/6} \frac{v_r}{r_{\text{ta},7}}, \quad (21)$$

where we have used the relations $r_{\text{ta}} \propto t^{8/9}$ and $a \propto t^{2/3}$, r_{ta} is the turnaround radius, $a_7 \equiv 7a_c$, $r_{\text{ta},7} \equiv r_{\text{ta}}(a_7)$ is set by finding the radius at which $v_r = 0$ at $a = a_7$, and the Hubble constant $H_7 \equiv H(a = a_7)$. The dimensionless radius is

$$\lambda = \frac{r}{r_{\text{ta}}} = \frac{r}{r_{\text{ta},7}} \left(\frac{a}{7a_c} \right)^{-4/3}. \quad (22)$$

In the case of self-similar infall, this profile does not change with time. As seen in Figure 9, $V(\lambda)$ for the simulated halo follows the self-similar solution closely, with $\lambda_{200}/\lambda_c \simeq 0.78$ (see Fig. 8), where λ_c is the radius at the outermost caustic and is approximately where the shock occurs in the collisional solution, and $\lambda_{200} \equiv r_{200}/r_{\text{ta}}$.

2.5.2 Density Profile

Although the halo generally grows by self-similar accretion for $3 < a/a_c < 7$, the mass density is better fit by an NFW profile with only one free parameter, c . Shown in Fig. 10 is the concentration parameter versus scale factor. We find it can be well-fitted by

$$c = c_f \frac{a}{a_f}, \quad (23)$$

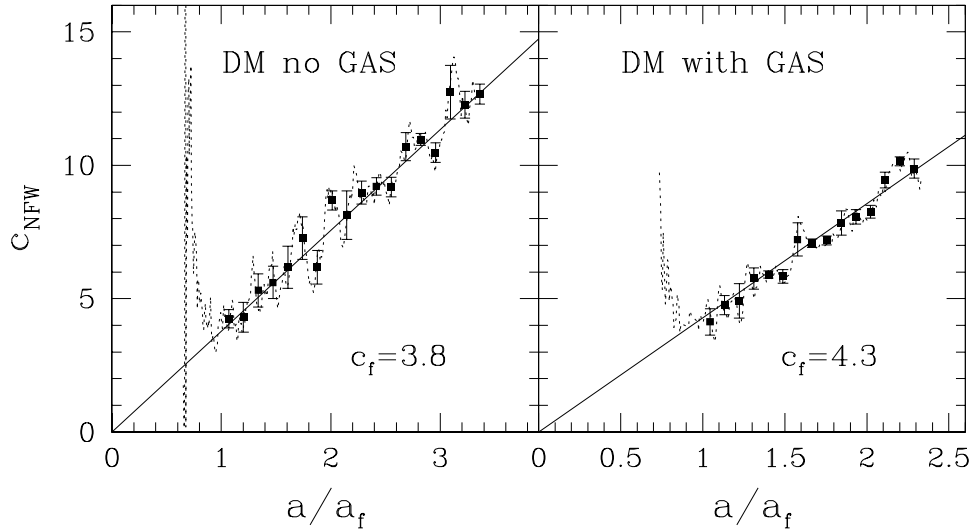


Figure 10: Evolution of concentration parameter of the best-fitting NFW profile for the dark matter halo in simulations with (right) and without (left) gas. Dotted line is the actual evolution, with the filled squares showing the mean concentration binned in scale factor. Errorbars indicate RMS fluctuations within each bin. The solid lines are the best-fitting linear evolution given by $c_{\text{NFW}} = c_f(a/a_f)$, with $a_f = 3a_c$.

where a_f is the scale factor at which the accretion rate becomes proportional to a , marking the end of the collapse phase. The value $a_f = 3a_c$ is used here for both simulation cases and corresponds to the vertical dotted line in Fig. 7. The solid lines in Fig. 10 correspond to the best-fit values $c_f = 4.3$ and $c_f = 3.8$ for the cases with and without gas included, respectively, where each data point was weighted by the goodness of the corresponding NFW profile fit.

This linear evolution was also found by [22] and [150]. In the latter case, they followed the mass accretion and merger histories of individual halos in a high-resolution CDM simulation of halos in the mass range $\approx 10^{11} - 10^{12} M_\odot$. The mass accretion histories allowed them to determine a collapse epoch for each halo, which they correlated with the halo's concentration. They found a best-fit slope for the linear evolution of concentration parameter of $c_f = 4.1$. We conclude that such an evolution of mass and concentration is generic and not limited to halos forming from CDM initial conditions.

3 The Fluid Approximation: 1D Halo Formation From Cosmological Infall

3.1 Self-Similar Gravitational Collapse

3.1.1 Previous analytical models for halo formation: the spherical infall model

Analytical approximations have been developed to model the formation of halos by the 1D growth of spherical cosmological density perturbations, in either a collisionless gas or a fluid. We shall need to refer to some of these solutions to justify our fluid approximation in §3.2. It is necessary to begin, therefore, by briefly recounting this earlier work.

[61] first presented the concept of the so called “secondary infall model (SIM)”. This SIM refers to the effect of the addition of a point mass to a uniform, expanding Friedmann-Robertson-Walker universe as a perturbation which causes the surrounding spherical shells to decelerate relative to the background universe, until they reach a radius of maximum expansion and recollapse. Subsequent work generalized this approach to include spherically-symmetric initial perturbations for which the overdensity profile depends upon radius or mass as a scale-free power-law. Along this line, [48] studied the dynamics of collisionless CDM halos using a self-similar model, adopting a scale-free initial overdensity parametrized by its shape: ε in equation (24). [14] studied a special case of [48] but also extended the analysis to a collisional fluid. [64] showed that a power-law power spectrum would indeed generate a scale-free initial condition, such as was adopted by [48]. They then argued that the resulting nonlinear structure would be described by a power-law profile determined by the shape of the power spectrum.

Previously mentioned works adopted a rather unrealistic condition for the collisionless case, that of purely radial motion. N-body simulations of CDM halo formation find that the virialized region tends toward isotropic random velocities. Some attempts to incorporate tangential velocities within the framework of spherical symmetry have also been made by [9, 65, 122]. Along this line, one may also refer to work by [40, 63, 89, 91] and references therein.

The fluid approximation for collisionless CDM halo formation has emerged recently. [142] showed that one could use fluid-like conservation equations to mimic the radial-only SIM models such as the [48] model. [137] extended this analysis to include tangential motion. The fluid approximation has been used in the literature of stellar dynamics, but its application to CDM halo dynamics is rather new, and as will be described in §3.2, it simplifies the description of dark matter dynamics substantially.

Self-similar spherical infall models have also been used to study the effect of incorporating additional baryonic physics. [1], [15] and [110] have studied the effect of gas cooling on galaxy formation using self-similar models. Because the system

was tuned to maintain self-similarity in the presence of cooling, the cooling function used is not perfectly physical. However, as shown by [1], one can use these models to test one's hydrodynamic code in the presence of cooling. And these models capture the generic behavior of galactic dynamics in the presence of realistic cooling.

Our model [2, 3], which will be described in § 3.4, is the first self-similar model to include the effective heat conduction resulting from SIDM collisionality. It utilizes the fluid approximation to describe SIDM halo dynamics, justifying its validity rigorously. The resulting formalism is similar to that of self-similar cooling models such as [1]. However, the focus is on dark matter physics rather than on baryonic physics. Thus, this is the first self-similar model in the presence of dark-matter-based heat conduction. It may also be used as a testbed for hydrodynamic simulations incorporating heat conduction.

3.1.2 Halo formation from scale-free linear perturbations

In the Einstein-de Sitter (EdS) background universe, an initial linear perturbation whose mass profile is spherically symmetric and has a scale-free, power-law form

$$\frac{\delta M}{M} \propto M^{-\varepsilon} \quad (24)$$

results in structure formation which is self-similar ([48]). Each spherical mass shell around the center expands until it reaches a maximum radius (turnaround radius r_{ta}), and recollapses. For a given ε , we have

$$r_{ta} \propto t^{\xi}, \quad (25)$$

where

$$\xi = \frac{2}{3} \left(\frac{3\varepsilon + 1}{3\varepsilon} \right) \quad (26)$$

([48]). Since there are no characteristic length or time scales for this problem other than the turn-around radius r_{ta} and the Hubble time t , the gravitational collapse which ensues from this scale-free initial condition must be self-similar as long as the background universe is Einstein-de Sitter, in the absence of physical processes which introduce additional scales (e.g. SIDM collisionality).

In general, if the unperturbed matter is a cold fluid, the infall which results from this perturbation is highly supersonic and is terminated by a strong accretion shock which thermalizes the kinetic energy of collapse. The accretion shock radius is guaranteed by self-similarity to be a fixed fraction of $r_{ta}(t)$ at all times. The mean density of the postshock region is, therefore, always a fixed multiple of the cosmic mean matter density. For most cases of interest, this postshock region is close to hydrostatic. For a collisionless gas, a similar description applies as long as the infalling matter initially had small (or no) random motions. In that case, each mass shell collapses supersonically as a single stream until it encounters a region of

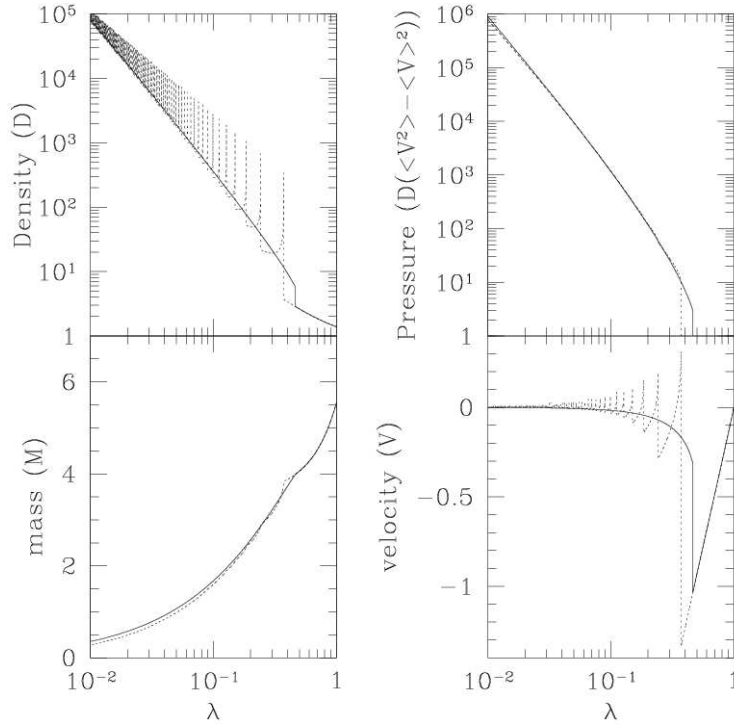


Figure 11: Self-similar collisionless halo formation for $\varepsilon = 1$: Comparison of the skewless-fluid approximation to the exact collisionless solution by [14]. Solid lines represent the solution obtained from fluid approximation in the radial direction, while dotted lines represent the collisionless Bertschinger solution. Spikes in the density plot simply represent infinite values, corresponding to caustics, and therefore there is no physical significance in the height of these spikes. However, spikes in the velocity plot are finite and real. Note that solid lines do not represent the $\gamma = 5/3$ fluid Bertschinger solution.

shell-crossing and density caustics, which encompasses all previously collapsed (i.e. interior) mass shells. All collapsed mass shells inside this region oscillate about the center. The radius of this region of shell-crossing, given by the outermost density caustic, is analogous to the shock radius in the fluid case.

Results for the purely collisionless case were presented for several values of ε by [48] and for $\varepsilon = 1$ by [14] (where the latter included a fluid component, as well). Figures 11 and 12 show the exact similarity solutions we have derived ([3]) for the purely collisionless cases with $\varepsilon = 1$ and $\varepsilon = 1/6$, respectively. As we describe below in § 3.1.3, these values roughly bracket the range relevant to cosmological halos in a CDM universe. We will refer to these solutions again for comparison in deriving our fluid approximation in § 3.2.

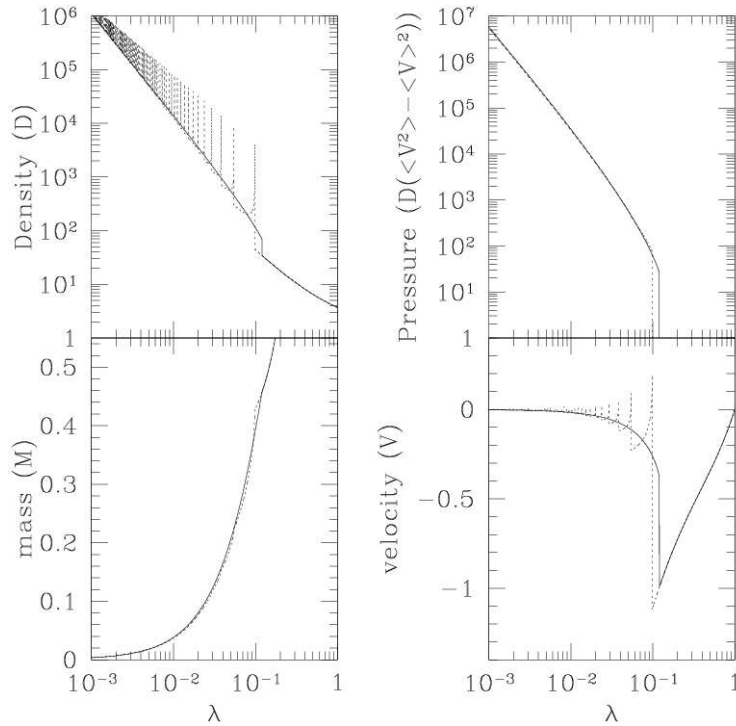


Figure 12: Same as Fig. 11, but $\varepsilon = 1/6$. Note again that solid lines were not generated from the $\gamma = 5/3$ fluid approximation, but rather from the radial-only fluid approximation).

3.1.3 Halo formation from peaks of the Gaussian random noise primordial density fluctuations

The theory of halo formation from peaks in the density field which results from Gaussian-random-noise initial density fluctuations draws an interesting connection between the average density profile around these peaks and the shape of the fluctuation power spectrum. According to [64], local maxima of Gaussian random fluctuations in the density can serve as the progenitors of cosmological structures. They show that high density peaks ($\nu \geq 3$, where ν corresponds to $\nu\sigma_M$ peak) have a simple power-law profile²

$$\Delta_0(r) \propto r^{-(n+3)}, \quad (27)$$

where $\Delta_0(r)$ is the accumulated overdensity inside radius r , and n is the effective index of the power spectrum $P(k)$ approximated as a power-law $P(k) \propto k^n$ at

²[11] also get a similar result: local density maxima have a triaxial density profile, but as ν increases it becomes more and more spherical with a profile converging to equation (27).

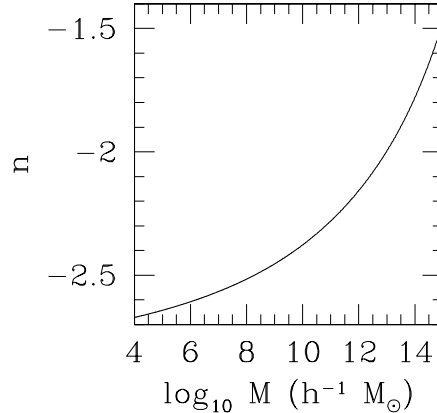


Figure 13: Effective index of the power spectrum ($P(k) \propto k^n$) vs. halo mass for the Λ CDM universe.

wavenumber k which corresponds to the halo mass through

$$M = \frac{4\pi}{3} \bar{\rho}_0 R^3, \quad (28)$$

where $\bar{\rho}_0$ is the present cosmic mean matter density and R is the comoving, spatial top-hat filter radius³. The overdensity $\Delta_0(r)$ is equivalent to the fractional mass perturbation $\delta M/M$ inside radius r ,

$$\Delta_0(r) = \delta M/M \propto M^{-\frac{n+3}{3}}. \quad (29)$$

From equations (24) and (29), we deduce that the power-law power spectrum naturally generates a scale-free initial condition with

$$\varepsilon = (n + 3)/3. \quad (30)$$

According to this model, halos of a given mass M originate from density perturbations given by equation (29) with n determined by the primordial power spectrum after it is transferred according to the parameters of the background universe and the nature of the dark matter. We plot this effective n as a function of halo mass in Fig. 13 for the currently-favored Λ CDM universe. The value of $n \simeq -2.5$ is a reasonable approximation for galactic halos [i.e. $n \simeq -2.5 \pm 0.1$ for $M \simeq 10^{8 \pm 2} M_{\odot}$, while $n \simeq -2.5 \pm 0.2$ for M in the range from $10^3 M_{\odot}$ to $10^{11} M_{\odot}$]. For halos in the cluster mass range, $M \sim 10^{15} M_{\odot}$, $n \simeq -1.5$.

³As long as one is concerned about the average profile, equation (27) holds for any value of ν . For small ν , however, random dispersion around this average profile becomes substantial, limiting the generality of equation (27).

3.2 Fluid Approximation of Collisionless CDM Halo Dynamics

This approach is used to simplify our understanding of the formation of CDM halos. We show that the fluid conservation equations for a gas with adiabatic index $\gamma = 5/3$ are a good approximation to the dynamics of CDM halos and self-interacting dark matter halos, which will be treated in detail in §3.4. This may bother some readers since, strictly speaking, the collisionless nature of CDM prohibits the use of such an approximation. However, a couple of simple assumptions enable us to treat CDM halo dynamics with the usual fluid conservation equations. For a more detailed description, see [3].

We first assume spherical symmetry, and define the average of physical quantities as follows:

$$\rho = \int f d^3v, \quad (31)$$

$$\langle A \rangle \equiv \frac{\int A f d^3v}{\int f d^3v} = \frac{1}{\rho} \int A f d^3v, \quad (32)$$

$$u \equiv \langle v_r \rangle, \quad (33)$$

$$p_r \equiv \rho \langle (v_r - \langle v_r \rangle)^2 \rangle, \quad (34)$$

$$p_\theta \equiv \rho \langle (v_\theta - \langle v_\theta \rangle)^2 \rangle = \rho \langle v_\theta^2 \rangle, \quad (35)$$

$$p_\phi \equiv \rho \langle (v_\phi - \langle v_\phi \rangle)^2 \rangle = \rho \langle v_\phi^2 \rangle, \quad (36)$$

where f is the distribution function defined such that $f(\mathbf{r}, \mathbf{v}) d^3r d^3v =$ mass within an infinitesimal volume $d^3r d^3v$ at (\mathbf{r}, \mathbf{v}) , ρ is the density, $\langle A \rangle$ is the average value of a certain quantity A , u is the radial bulk velocity, p_r is the “effective radial pressure”, and p_θ is the “effective tangential pressure”. Note that $\langle v_\theta \rangle = \langle v_\phi \rangle = 0$ and $p_\theta = p_\phi$ because of spherical symmetry. Anisotropy in the velocity dispersion occurs in general for collisionless systems – i.e. $p_r \neq p_\theta$, or anisotropy parameter $\beta \neq 0$, where $\beta \equiv 1 - \frac{p_\theta}{p_r}$ – implying that p_r and p_θ should be treated separately. In a highly collisional system, which is well described by fluid conservation equations, $p_r = p_\theta$ and the usual pressure $p = p_r = p_\theta$.

A self-gravitating system of collisionless particles can be described by the collisionless Boltzmann equation

$$\frac{df}{dt} \equiv \frac{\partial f}{\partial t} + \mathbf{v} \cdot \nabla f - \nabla \Phi \cdot \frac{\partial f}{\partial \mathbf{v}} = 0. \quad (37)$$

In spherical symmetry, $f = f(|\mathbf{r}|, \mathbf{v})$, equation (37) becomes

$$\begin{aligned} 0 &= \frac{\partial f}{\partial t} + v_r \frac{\partial f}{\partial r} + \left(\frac{v_\theta^2 + v_\phi^2}{r} - \frac{\partial \Phi}{\partial r} \right) \frac{\partial f}{\partial v_r} \\ &\quad + \frac{1}{r} (v_\phi^2 \cot \theta - v_r v_\theta) \frac{\partial f}{\partial v_\theta} \\ &\quad - \frac{v_\phi}{r} (v_r + v_\theta \cot \theta) \frac{\partial f}{\partial v_\phi}, \end{aligned} \quad (38)$$

where Φ satisfies the Poisson equation, $\nabla^2\Phi = 4\pi G\rho$ [16]. By multiplying equation (38) by $v_r^m v_\theta^n$, where m, n are integers, and integrating over velocity d^3v , we can form a set of moment equations. Moment equations from the lowest order are

$$\frac{\partial\rho}{\partial t} + \frac{\partial}{r^2\partial r}(r^2(\rho u)) = 0, \quad (39)$$

$$\frac{\partial}{\partial t}(\rho u) + \frac{\partial}{\partial r}(p_r + \rho u^2) + \frac{2}{r}(p_r - p_\theta + \rho u^2) = -\rho\frac{Gm}{r^2}, \quad (40)$$

$$\rho\frac{D}{Dt}\left(\frac{p_r}{2\rho}\right) + p_r\frac{\partial u}{\partial r} = \Gamma_1, \quad (41)$$

$$\rho\frac{D}{Dt}\left(\frac{p_\theta}{2\rho}\right) + \frac{p_\theta u}{r} = \Gamma_2, \quad (42)$$

⋮

where m is the mass enclosed by a shell at radius r , $\frac{D}{Dt} \equiv \frac{\partial}{\partial t} + u\frac{\partial}{\partial r}$, and

$$\Gamma_1 = \frac{\rho}{r}\left\langle 2(v_r - \langle v_r \rangle)v_\theta^2 \right\rangle - \frac{1}{2r^2}\frac{\partial}{\partial r}\left(r^2\rho\left\langle (v_r - \langle v_r \rangle)^3 \right\rangle\right), \quad (43)$$

$$\Gamma_2 = -\frac{1}{4r^4}\frac{\partial}{\partial r}\left(r^4\rho\left\langle (v_r - \langle v_r \rangle)v_\theta^2 \right\rangle\right). \quad (44)$$

Equations (39-42) are conservation equations of mass, momentum, “radial” energy, and angular momentum, respectively. Note that equations (39)-(44) are all in exact form, and the hierarchy of equations is not closed in principle.

Now we make a further simplification that the distribution of v_r is skewless – v_θ and v_ϕ are naturally skewless because of spherical symmetry. In other words, we assume that v_r has a symmetric distribution around $\langle v_r \rangle$. It is not straightforward to show that Γ_1 and Γ_2 are negligible in equations (41) and (42). However, we demonstrate that the assumption of “skewlessness” in the fluid approximation yields results which are in good agreement with the purely collisionless CDM structure for specific examples. Equations (39) - (41) with the condition $p_\theta = 0$ and $\Gamma_1 = 0$ can be used to solve purely radial problems, such as the self-similar spherical infall problems with similarity solutions by [14] ($\varepsilon = 1$) and [48] ($\varepsilon = 1/6$). Comparisons of the fluid approximation in these cases, as shown in Figures 11 and 12, reveal an excellent agreement with the true collisionless solutions. The difference observed at caustics – places where the density becomes infinite – is negligible, because caustics do not affect the overall dynamics of the halo. Since the skew-free assumption naturally neglects dynamically unimportant structure (e.g. caustics) while accurately reproducing the profile of the exact solution in these radial cases, it may also be applied to describe CDM halos, in which particles also have a tangential motion.

The final assumption is that the velocity distribution is isotropic, or $p_r = p_\theta$. This is an empirical assumption: CDM halos in cosmological N-body simulations

show mild anisotropy. For instance, [27] show that CDM halos in their numerical simulation can be well-fitted by a fitting formula

$$\beta(r) = \beta_m \frac{4r}{r^2 + 4}, \quad (45)$$

where r is in units of r_{200} , and $\beta_m \approx 0.5$ in N-body simulations [27, 31].

With these assumptions – spherical symmetry, skew-free velocity distribution and isotropic velocity dispersion – and with the operation (equation 41) + 2×(equation 42), the usual energy conservation equations are obtained. They are

$$\frac{\partial \rho}{\partial t} + \frac{\partial}{\partial r} (r^2 (\rho u)) = 0, \quad (46)$$

$$\frac{\partial}{\partial t} (\rho u) + \frac{\partial}{\partial r} (p + \rho u^2) + \frac{2}{r} \rho u^2 = -\rho \frac{Gm}{r^2}, \quad (47)$$

$$\frac{D}{Dt} \left(\frac{3p}{2\rho} \right) = -\frac{p}{\rho} \frac{\partial}{\partial r} (r^2 u), \quad (48)$$

which are identical to the fluid conservation equations for a $\gamma = 5/3$ gas in spherical symmetry.

In this section, we showed how one could use the usual fluid conservation equations to approximate collisionless CDM halo dynamics. §3.3 and 3.4 describe its practical application.

3.3 Halo Formation by Non-Self-Similar Infall: Mass Assembly History and the Origin of CDM N-body Halo Profiles

N-body simulations of CDM have not only found a universal halo density profile, but have also found that the masses and concentrations of individual N-body CDM halos grow over time according to simple universal formulae [150]. Very similar results were also found for N-body simulations of halos formed by the instability of cosmological pancakes (see §2). In what follows we use the fluid approximation to show that this universal time-dependent halo density profile can be understood as the dynamical outcome of continuous infall according to the universal mass accretion history [4].

3.3.1 Models and Initial Conditions

We attempt to understand the form and evolution of dark matter halos with three spherically-symmetric models; halted infall, radial orbits, and a fluid approximation. Each model assumes that the mass M_{vir} within an overdensity Δ_{vir} follows the relation given by [150]

$$M_{\text{vir}}(a) = M_{\infty} \exp[-Sa_f/a], \quad (49)$$

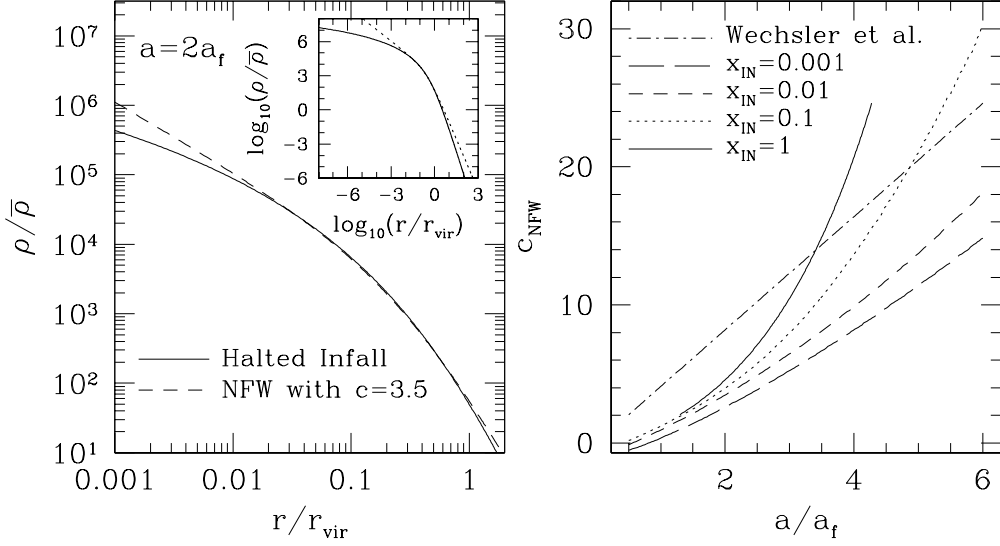


Figure 14: (left) Density profile from halted infall model along with best-fitting NFW profile for this profile at present. Inset in upper-right shows same over much larger range. (right) Evolution of NFW concentration parameter in the halted infall model, compared with empirical relation of [150] for CDM N-body halos. Different line types indicate different ranges $x_{\text{in}} < x < 1$, within which halo was fit to an NFW profile, where $x \equiv r/r_{\text{vir}}$, $r_{\text{vir}} \equiv r_{200}$.

where S is the logarithmic mass accretion rate $d \ln M_{\text{vir}} / d \ln a$ when $a = a_f$. Here and in [150], $S = 2$. Such a relation is claimed to be a good fit to the evolution of halos of different masses and formation epochs. We use $\Delta_{\text{vir}} = 200$, so that the halo has a mass M_{200} and radius r_{200} . We have found an initial perturbation profile consistent with equation (14) (for EdS),

$$\frac{\delta M}{M} \equiv \frac{M - \bar{M}}{\bar{M}} = \delta_i \ln \frac{M}{M_\infty}, \quad (50)$$

where δ_i depends on the initial scale factor a_i , a_f , and δ_{vir} , and \bar{M} is the unperturbed mass. The parameter $b = 1$ if pressure or shell crossing are not present outside of r_{vir} . If they are present outside the halo however, the initial perturbation is not guaranteed to lead to the correct mass accretion rate. In our radial orbit and fluid approximation calculations below, where shell crossing and pressure are indeed present outside of r_{vir} , we have found that the resulting mass is close to that of equation (49) if b is allowed to vary as a fitting parameter ($b = 1(0.7)$ in the fluid approximation (radial orbits) calculations).

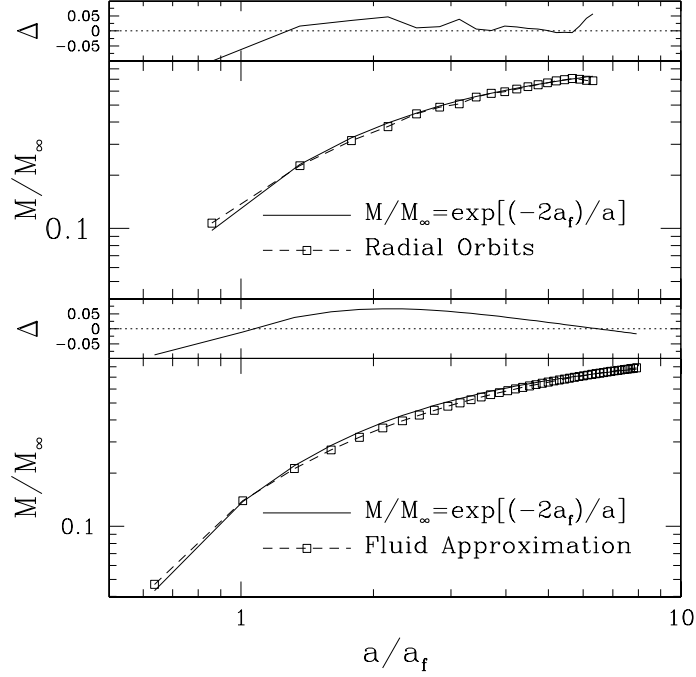


Figure 15: Evolution of mass for the radial orbits (top) and fluid approximation (bottom) simulations, compared with the empirical relation of [150] for CDM N-body results. Shown above each are the fractional deviations $\Delta \equiv (M_{\text{exact}} - M)/M$.

3.3.2 Halted Infall Model

In the simplest model, we have assumed that infalling shells come to an abrupt halt upon crossing into the halo, so that the velocity is zero for $r < r_{\text{vir}}$. The mass of the halo is

$$M_{\text{vir}}(a) = \frac{4\pi}{3} \delta_{\text{vir}} \bar{\rho} r_{\text{vir}}^3, \quad (51)$$

where $\bar{\rho}$ is the cosmic mean mass density at that epoch. Mass continuity implies the density ρ_{vir} just inside the virial radius is related to the rate of halo mass and radius increase according to

$$\frac{dM_{\text{vir}}}{da} = 4\pi \rho_{\text{vir}} r_{\text{vir}}^2 \frac{dr_{\text{vir}}}{da}. \quad (52)$$

Differentiating equation (51) and combining with equations (49) and (52), one obtains

$$\frac{\rho_{\text{vir}}}{\bar{\rho}_0} = \delta_{\text{vir}} a^{-3} \left[1 + \frac{3a}{S a_f} \right]^{-1}, \quad (53)$$

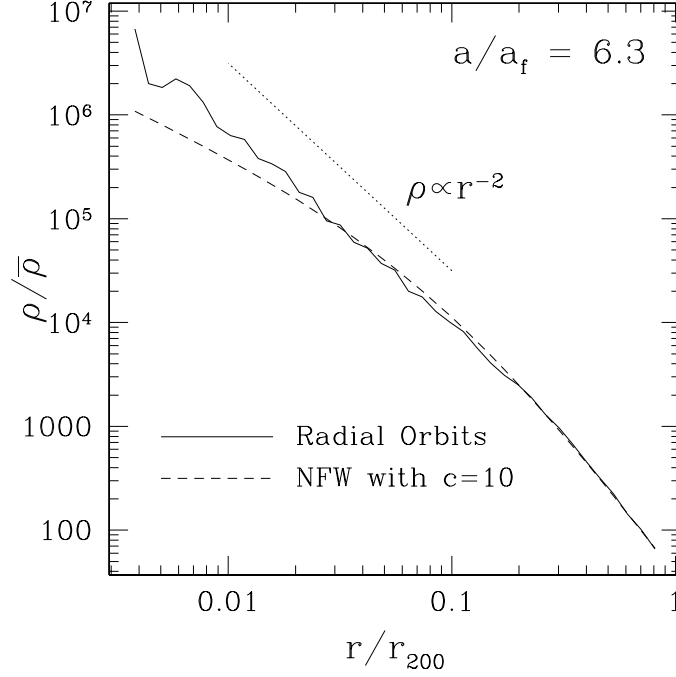


Figure 16: Density profile at the end of the radial orbit simulation.

where $\bar{\rho}_0$ is the mean background density at $a = 1$. The virial radius is given by

$$\frac{r_{\text{vir}}}{r_{\text{vir},0}} = a \exp \left[\frac{-S a_f}{3} \left(\frac{1}{a} - 1 \right) \right]. \quad (54)$$

Equations (53) and (54) are parametric in a , implying a radial density profile $\rho(r) = \rho_{\text{vir}}(r_{\text{vir}})$ that is frozen in place as matter crosses r_{vir} . Taking the limit in which $a \rightarrow \infty$, the outer density profile approaches $\rho \propto r^{-4}$ at late times, consistent with finite mass, while the inner slope becomes asymptotically flat. The NFW profile is

$$\frac{\rho(x)}{\bar{\rho}} = \frac{\delta_{\text{vir}} g(c)}{3x(1+cx)^2}, \quad (55)$$

where

$$g(c) = \frac{c^2}{\ln(1+c) - c/(1+c)}, \quad (56)$$

and $x \equiv r/r_{\text{vir}}$. Combining equations (53) and (55) with $x = 1$, yields an equation for the evolution of concentration with scale factor (see Fig. 14),

$$\frac{a}{a_f} = S \left[\frac{(1+c)^2}{g(c)} - \frac{1}{3} \right]. \quad (57)$$

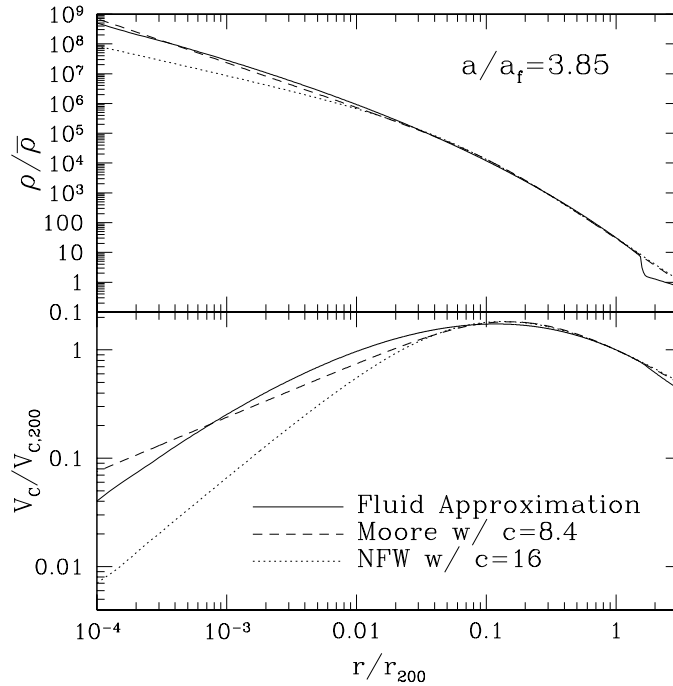


Figure 17: (top) Density profile at the end of the isotropic fluid calculation. (bottom) Circular velocity profile.

3.3.3 Radial Orbits Model

We use a finite-difference spherical mass shell code to follow the evolution of a small amplitude initial perturbation given by equation (50), which is chosen so that the resulting virial mass will evolve according to equation (49). The shell code has an inner reflecting core and the results presented here used 20,000 shells. The resulting evolution of halo mass and the comparison of the halo density profile with the NFW profile are shown in Figures 15 and 16.

3.3.4 Fluid Approximation Model

As mentioned earlier in §3.2, the collisionless Boltzmann equation in spherical symmetry yields fluid conservation equations ($\gamma = 5/3$) when random motions are isotropic. Halos in N-body simulations have somewhat radially-biased random motion, but the bias is small, especially in the center. Outside the virialized halo, in the infall region, the radial bias is irrelevant, since the motion is highly supersonic and random motions do not affect the dynamics there. This isotropic fluid model is therefore a better approximation to halo formation in N-body simulations than one with purely radial motion. We use a 1-D, spherical, Lagrangian hydrodynamics code

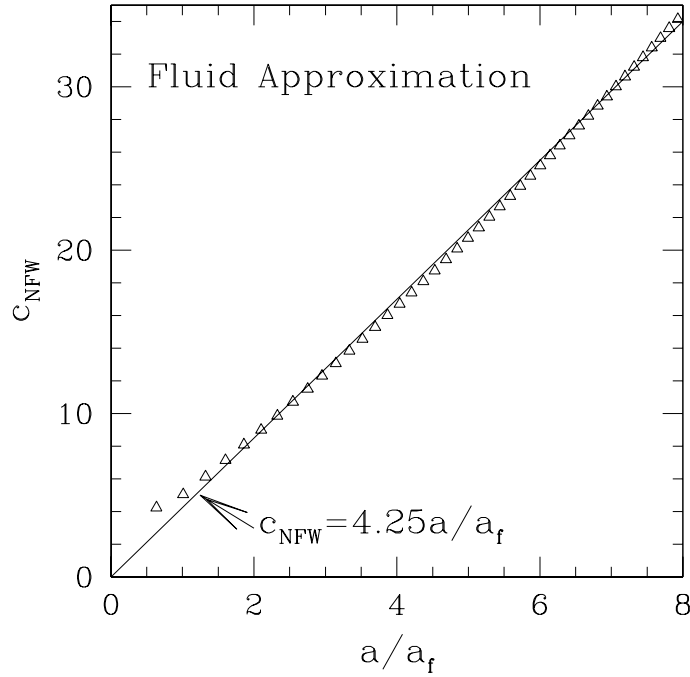


Figure 18: Evolution of concentration parameter with scale factor in the isotropic fluid calculation.

as in [143], using 1,000 zones logarithmically spaced in mass. The initial conditions were chosen in the same way as those for the radial orbit model (Eq. (50)), with zero initial temperature. Results are plotted in Figures 15-18.

3.3.5 Results

Our results can be summarized as follows:

- The halted infall model of §3.3.2 does not reproduce the linear evolution of concentration parameter with scale factor reported by [150], but can be fit by an NFW profile over a limited range of radii and scale factors (Fig. 14).
- We have derived an initially linear perturbation profile that is a good model for the spherically-averaged initial condition that leads to the Lagrangian mass evolution of CDM halos found in N-body simulations by [150].
- Starting from this perturbation, the radial orbit model of section 3.3.3 fails to reproduce the inner slope of the NFW profile, approaching $\rho \propto r^{-2}$ instead, consistent with the argument of [120] (Fig. 16).

- The fluid approximation of §3.3.4, however, leads to a halo that is well-fitted by the NFW and Moore profiles for all radii resolved by N-body simulations ($r/r_{200} \geq 0.01$) (Fig. 17).
- In addition, the evolution of the NFW concentration parameter in the fluid approximation is a close match to that of [150], with $c_{\text{NFW}} = 4.25a/a_f$ a good fit (Fig. 18); $c_{\text{NFW}} = 4.1a/a_f$ was the relation reported by [150].

The fluid approximation model reproduces the N-body results remarkably well, once the mass accretion history is given. We are thus led to conclude that complicated merging processes are not necessary in order to understand the overall structure and evolution of the halo mass distribution, and that it is largely determined by the mass accretion history.

3.4 Structure of Self-Interacting Dark Matter Halos

As we will demonstrate below, halo models with a small flat core, such as the Truncated Isothermal Sphere (TIS) halo equilibrium model described in § 4 agree well with the statistical properties of observed halos and with the averaged properties of simulated halos. However, the dynamical origin of such an equilibrium structure and the particular question of how the flat density core can form are not addressed by an equilibrium analysis. Halos in high-resolution N-body simulations in the Λ CDM model, on the other hand, show cuspy density profiles.

Among several suggestions made to resolve this problem, self-interacting dark matter (SIDM) has drawn substantial attention. It was suggested by [135] that the purely collisionless nature of CDM be replaced by SIDM which interacts by non-gravitational, microscopic interaction (e.g. elastic scattering). Various attempts have been made to incorporate SIDM in semi-analytical studies (e.g. [10]) as well as in N-body simulations (e.g. [25, 36, 85, 154]), and they all show that flat density cores can arise. However, new theoretical problems have arisen for these SIDM halos: 1) study of “isolated” (i.e. no cosmological infall) halos revealed unstable cores ([25, 85]) and 2) cosmological N-body simulations ([36, 154]) showed a more prominent flattening effect for high-mass halos ($M_{\text{halo}} \simeq 10^{12} M_{\odot}$) than for low-mass halos ($M_{\text{halo}} \simeq 10^9 - 10^{10} M_{\odot}$), which appears to contradict observations which show that the flattening effect is most prominent for dwarfs and low surface brightness (LSB) galaxies with $M_{\text{halo}} \simeq 10^9 - 10^{10} M_{\odot}$.

The semi-analytical study by [10] applied the fluid approximation to an isolated halo, properly accounting for the effective “conduction” arising from the SIDM collisionality. They showed that SIDM halos could have a lifetime long enough to survive in a Hubble time, if initially the scattering mean free path is much greater than the size of the halos. However, as was found in [25, 85], the scattering mean free path can be smaller than the halo size if the scattering cross-section is large enough. In this case, *isolated* SIDM halos would still be unstable.

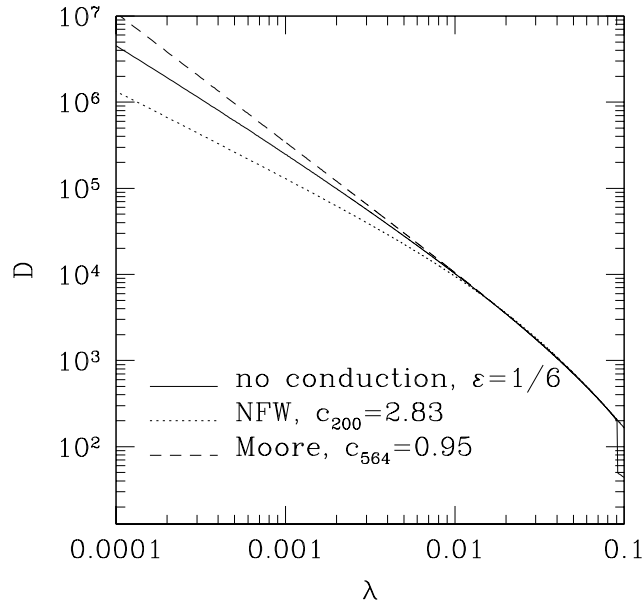


Figure 19: Halo density profile produced by fluid approximation with $\varepsilon = 1/6$ for standard CDM halos, compared to the best-fitting NFW and Moore profiles. The adiabatic solution, whose inner slope is about -1.27 , is a good fit to density profiles of CDM halos from N-body simulations.

We show that these problems can be naturally resolved [2, 3]. We partially adopt the formalism by [10] and improve upon it by properly including cosmological infall. We have thereby derived an analytical, cosmological similarity solution. Our approach is as follows. As shown in § 3.1.3, the power spectrum in the mass range of dwarfs and LSBs is well described by a power law $P(k) \propto k^n$ with $n \simeq -2.5$. From equation (29), we then have

$$\delta M/M \propto M^{-1/6}. \quad (58)$$

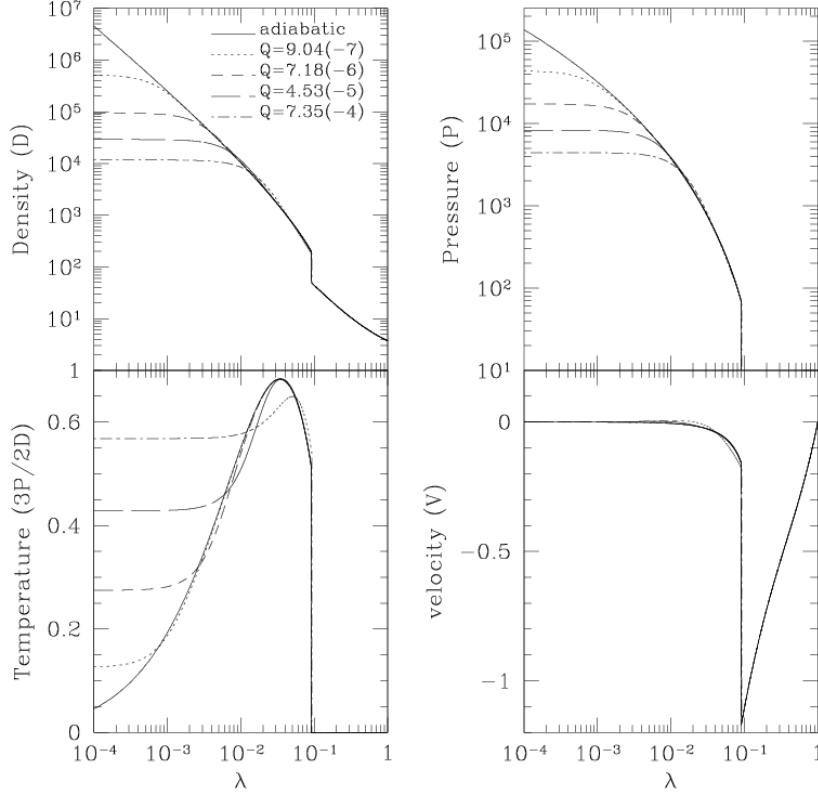
This also results in

$$r_{\text{ta}} \propto t^2, \quad (59)$$

where r_{ta} refers to a “turn-around” radius at which radial velocity vanishes. For any value of n , r_{ta} serves as a natural length scale for self-similar accretion.

This is not true for SIDM halos because the SIDM interaction brings in a new length scale which does not in general preserve this self-similarity. However, $n = -2.5$ is a magic number which preserves the self-similarity because in this case the new length scale is always a fixed fraction of the halo size. Specifically, SIDM introduces a conductive heat flux ([10])

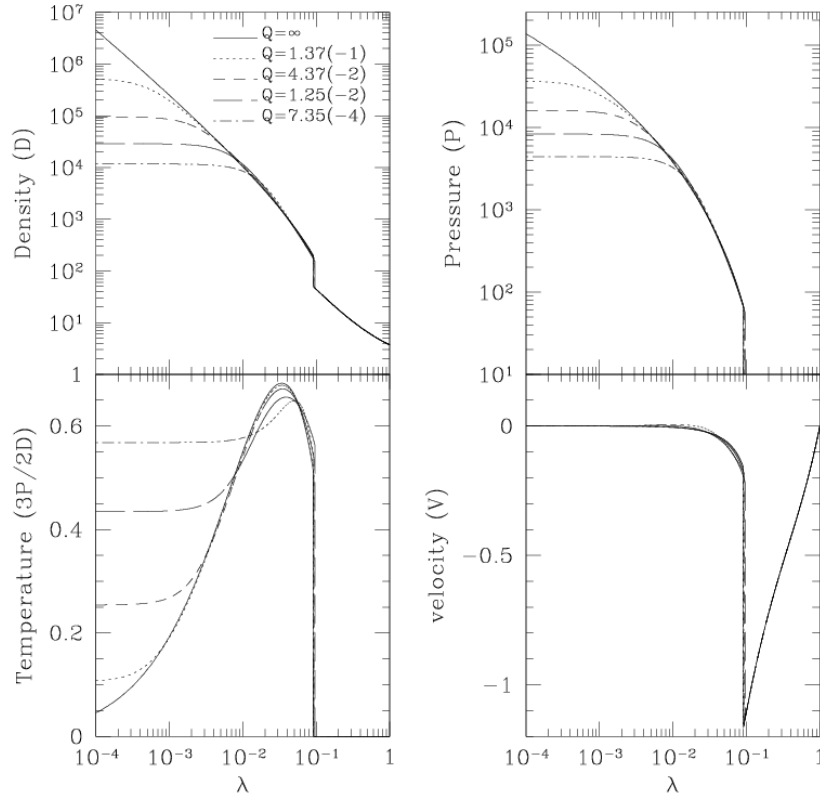
$$f = -\frac{3ab\sigma}{2} \sqrt{\frac{p}{\rho}} \left(a\sigma^2 + \frac{4\pi G}{p} \right)^{-1} \frac{\partial}{\partial r} \left(\frac{p}{\rho} \right) \quad (60)$$

Figure 20: Profiles of the low- Q solutions.

where σ is the interaction cross-section, ρ is the density, and $p = \rho \langle v - \langle v \rangle \rangle^2$ is the effective “pressure” ([2, 3] considered an elastic scattering case, in which $a = 2.26$ and $b = 1.002$). The thermal energy changes according to $\rho \frac{\partial e}{\partial t} \propto r_{\text{ta}}^2 t^{-5}$, while the conductive heating rate is $\nabla \cdot \mathbf{f} \propto r_{\text{ta}}^3 t^{-7}$. Self-similarity is preserved only when these terms have the same time dependence, or $r_{\text{ta}} \propto t^2$. From eq (25), this condition is equivalent to $n = -2.5$.

As shown in §3.1.3, dwarfs and LSBs are well described by self-similar solutions with this requirement. This implies that the core of an SIDM halo in that mass range would be stable, since the core’s size would grow in proportion to the virial radius r_v , or the turnaround radius r_{ta} . In other words, the collapse of halo cores predicted for isolated SIDM halos is entirely prevented by cosmological infall, which resolves the issue of stability of SIDM halo cores.

Before treating soft-core solutions, we describe properties of this self-similar solution without SIDM collisionality, i.e. the case for $f = 0$. The solution obtained by applying the fluid approximation – equations (46 - 48) – to the $\varepsilon = 1/6(n =$


 Figure 21: Profiles of the high- Q solutions.

-2.5) case yields a profile which resembles CDM halos in many aspects. First, as shown in Figure 19, it has a density cusp with a logarithmic slope ≈ -1.27 at $4 \times 10^{-3} < r/r_{200} < 1.4 \times 10^{-2}$, which is between -1 (NFW profile) and -1.5 (Moore profile)⁴. Second, the temperature profile is very similar to that of CDM halos. The temperature is zero at the center, rises to a maximum as radius increases until a point where the temperature starts to drop again (see the solid line in the temperature plot of Figure 20). This validates the use of our model for the study of SIDM halos and even makes it possible to correctly calculate the physical effect of SIDM collisionality.

In the presence of SIDM collisionality, similarity solutions reveal soft-cores. Different solutions arise for different values of the dimensionless collisionality parameter $Q \equiv \sigma \rho_b r_s$, where ρ_b is the cosmic mean matter density and r_s is the effective shock

⁴This solution is well-fitted by NFW profiles with very low concentration parameter $c \approx 3$. $\varepsilon = 1/6$ corresponds to a fast mass accretion rate, $d \ln M / d \ln a = 6$, which is typical for the earliest epoch of mass accretion for standard CDM halos at $a/a_c < 1$. Therefore, this solution can be said to capture the very early formation epoch of CDM halos.

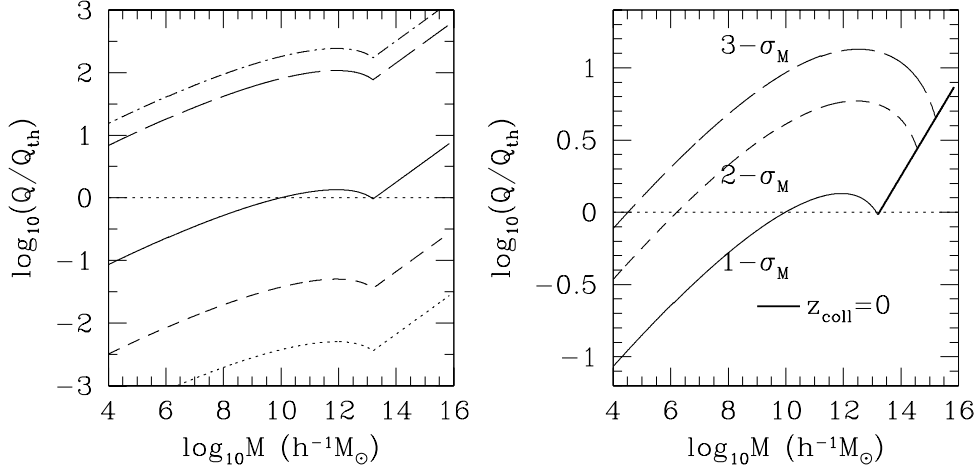


Figure 22: Collisionality parameter Q vs. halo mass M . (left) “Typical” halos, well represented statistically by a $1 - \sigma_M$ fluctuation. Different curves correspond to different scattering cross section σ ($\sigma = 0.56, 5.6, 200, 1.2 \times 10^4, 2.7 \times 10^4$ from bottom to top). (right) Different $\nu - \sigma_M$ fluctuations for $\sigma = 200 \text{ cm}^2 \text{ g}^{-1}$.

radius. Q is constant during the matter-dominated epoch, $z \geq 1$, because $\rho_b \propto t^{-2}$ and $r_v \propto t^2$.

Fig. 20 and Fig. 21 show profiles for different Q 's. One would naively expect that as Q (σ) increases, the central density decreases because of the increasing flattening effect. However, if Q is too large, the mean free path between collisions is smaller than the size of the halo, which reduces the flattening effect. Therefore, there are two opposite regimes, low- Q (long mean free path; Fig 20) and high- Q (short mean free path; Fig 21), which are separated by some threshold Q_{th} . We found that $Q_{\text{th}} = 7.35 \times 10^{-4}$.

The behavior of high- Q solutions also gives us a clue as to how a constant cross section σ may still resolve the problem 2). By using the Press-Schechter formalism, [2, 3] relate Q to the halo mass M . When one matches $Q(M \simeq 10^9 - 10^{10} M_{\odot})$ to Q_{th} , which is well-fitted by the empirical rotation fitting formula for dwarfs and LSBs (described in the following paragraph), one finds that $\sigma \simeq 200 \text{ cm}^2 \text{ g}^{-1}$ and collisionality increases as mass increases, which indicates that halos more massive than dwarfs and LSBs will have *less* density-flattening. This argument is consistent with previous N-body simulations by [154] and [36]: they used $\sigma \simeq 0.1 - 10 \text{ cm}^2 \text{ g}^{-1}$, which is in the low- Q regime. In the low Q regime, increasing Q means more density-flattening. They simply did not push σ to higher values, which would have covered the high- Q regime (See Fig. 22).

Since the Q_{th} solution shows the most prominent density-flattening effect, it can

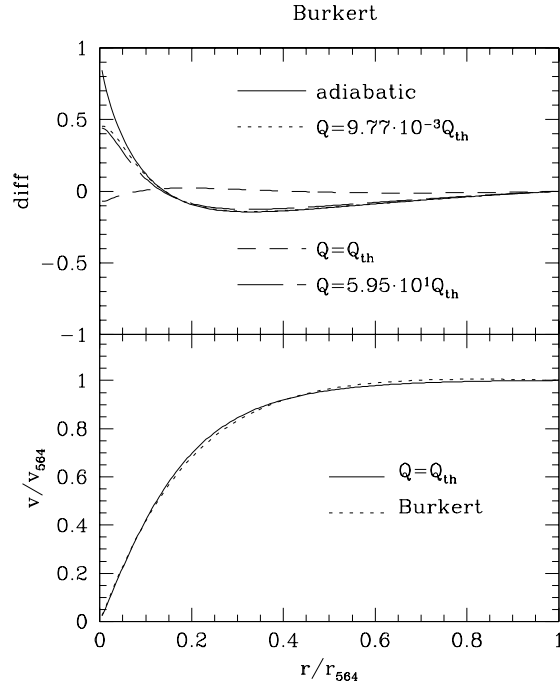


Figure 23: Rotation curve fitting: The Q_{th} solution is the one that is best-fitted by the Burkert profile.

be said to be the most relaxed state possible for SIDM halos. We found that in fact the solution with $Q = Q_{\text{th}}$ is well described by the TIS profile [3]. We fitted rotation curves of various Q solutions with the empirical rotation curve fitting formula found by Burkert ([24]; Burkert profile) and found that the $Q = Q_{\text{th}}$ profile is best fit by the Burkert profile (See Fig. 23). As shown in [71], the TIS profile is also well-fitted by the Burkert profile. The fact that Q_{th} is best fit by the Burkert profile (and therefore the TIS profile) suggests that in fact Q_{th} is the most relaxed system among the various Q solutions, since the requirement for TIS, the minimum energy, is usually met by the most relaxed system.

4 The Truncated Isothermal Sphere (TIS) Model

We have developed an analytical model for the postcollapse equilibrium structure of virialized objects which condense out of a cosmological background universe, either matter-dominated or flat with a cosmological constant [128, 71]. The model is based upon the assumption that cosmological halos form from the collapse and virialization of “top-hat” density perturbations and are spherical, isotropic, and isothermal. This leads to a unique, nonsingular TIS, the minimum-energy solution

Table 1: A comparison of three approximations for the postcollapse equilibrium structure of top-hat density perturbations in a low density universe.

	SUS ^a	SIS ^b	TIS (SCDM; Λ CDM, $z = 0$)
η/η_{SUS}	1	0.833	1.11;1.07
T/T_{SUS}	1	3	2.16;2.19
ρ_0/ρ_t	1	∞	514;530
$\langle\rho\rangle/\rho_t$	1	3	3.73;3.68
r_t/r_0	– NA –	∞	29.4;30.04
$\Delta_c/\Delta_{c,\text{SUS}}$	1	1.728	0.735;0.774
$K/ W $	0.5	0.75	0.683;0.690

^aA top-hat perturbation of a given mass collapses at a given redshift in a background universe with given values of Ω_0 and λ_0 ; all of these values are held fixed in this comparison of the three approximations.

^bThese SIS numbers are an approximation which ignores the small modification of the Lane-Emden equation solution to take account of $\Lambda \neq 0$, but accounts for the more important effects of $\Lambda \neq 0$ on top-hat evolution, energy conservation and the virial theorem.

of the Lane-Emden equation (suitably modified for non-zero cosmological constant $\Lambda \neq 0$). The size r_t and velocity dispersion σ_V are unique functions of the mass and redshift of formation of the object for a given background universe. Our TIS density profile flattens to a constant central value, ρ_0 , which is roughly proportional to the critical density of the universe at the epoch of collapse, with a small core radius $r_0 \approx r_t/30$ (where $\sigma_V^2 = 4\pi G\rho_0 r_0^2$ and $r_0 \equiv r_{\text{King}}/3$, for the ‘‘King radius’’ r_{King} , defined by [16], p. 228). The density profiles for gas and dark matter are assumed to be the same (no bias), with gas temperature $T = \mu m_p \sigma_V^2 / k_B$. While this TIS density profile is obtained numerically by solving a differential equation, it is well-fitted by the following approximation:

$$\rho(r) = \rho_0 \left(\frac{A}{a^2 + r^2/r_0^2} - \frac{B}{b^2 + r^2/r_0^2} \right), \quad (61)$$

where $A = 21.38$, $B = 19.81$, $a = 3.01$, $b = 3.82$ [128, 71].

These TIS results differ from those of the more familiar approximations in which the virialized sphere resulting from a top-hat perturbation is assumed to be either the standard uniform sphere (SUS) or else a singular isothermal sphere (SIS). We summarize their comparison in Fig. 24 and Table 1, where η is the final radius of the virialized sphere in units of the top-hat radius r_m at maximum expansion (i.e. $\eta_{\text{SUS}} = 0.5$), $\rho_t \equiv \rho(r_t)$, $\langle\rho\rangle$ is the average density of the virialized spheres, $\Delta_c = \langle\rho\rangle/\rho_{\text{crit}}(t_{\text{coll}})$, and $K/|W|$ is the ratio of total kinetic (i.e. thermal) to gravitational potential energy of the spheres.

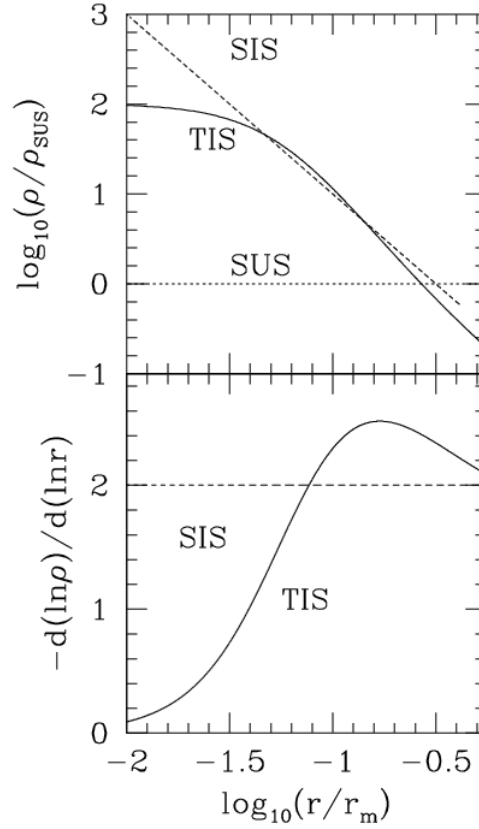


Figure 24: (top) Density profile of TIS which forms from the virialization of a top-hat density perturbation in a matter-dominated universe. Radius r is in units of r_m - the top-hat radius at maximum expansion. Density ρ is in terms of the density ρ_{SUS} of the SUS approximation for the virialized, post-collapse top-hat. (bottom) Logarithmic slope of density profile.

For all cases of current astronomical interest, an excellent approximation to the exact results in [71] (Paper II) for the dependence of the TIS halo parameters on the halo mass, collapse redshift and the background universe is given by [71] according to

$$r_m = 337.7 \left(\frac{M_0}{10^{12} M_\odot} \right)^{1/3} [F(z_{\text{coll}})]^{-1} h^{-2/3} \text{ kpc}, \quad (62)$$

$$r_t = 187.2 \left(\frac{M_0}{10^{12} M_\odot} \right)^{1/3} [F(z_{\text{coll}})]^{-1} h^{-2/3} \text{ kpc}, \quad (63)$$

$$r_0 = 6.367 \left(\frac{M_0}{10^{12} M_\odot} \right)^{1/3} [F(z_{\text{coll}})]^{-1} h^{-2/3} \text{ kpc}, \quad (64)$$

$$T = 7.843 \times 10^5 \left(\frac{\mu}{0.59} \right) \left(\frac{M_0}{10^{12} M_\odot} \right)^{2/3} F(z_{\text{coll}}) h^{2/3} \text{ K}, \quad (65)$$

$$\sigma_V^2 = 1.098 \times 10^4 \left(\frac{M_0}{10^{12} M_\odot} \right)^{2/3} F(z_{\text{coll}}) h^{2/3} \text{ km}^2 \text{ s}^{-2}, \quad (66)$$

$$\begin{aligned} \rho_0 &= 1.799 \times 10^4 [F(z_{\text{coll}})]^3 \rho_{\text{crit}}(z=0) \\ &= 3.382 \times 10^{-25} [F(z_{\text{coll}})]^3 h^2 \text{ g cm}^{-3}. \end{aligned} \quad (67)$$

where

$$F(z_{\text{coll}}) \equiv \left[\frac{h(z_{\text{coll}})}{h} \right]^2 \frac{\Delta_{\text{c,TIS}}(z_{\text{coll}}, \lambda_0)}{\Delta_{\text{c,TIS}}(\lambda_0 = 0)} = \left[\frac{\Omega_0}{\Omega(z_{\text{coll}})} \frac{\Delta_{\text{c,SUS}}}{18\pi^2} \right]^{1/3} (1 + z_{\text{coll}}). \quad (68)$$

For the EdS case, $F = (1 + z_{\text{coll}})$, while for an open, matter-dominated universe and a flat universe with a cosmological constant, $F \rightarrow \Omega_0^{1/3} (1 + z_{\text{coll}})$ at early times [i.e. $x \rightarrow 0$]. Here μ is the mean molecular weight, where $\mu = 0.59$ (1.22) for an ionized (neutral) gas of H and He with $[He]/[H] = 0.08$ by number. $\Delta_{\text{c,SUS}}$ is well-approximated by $\Delta_{\text{c,SUS}} = 18\pi^2 + c_1 x - c_2 x^2$, where $x \equiv \Omega(z_{\text{coll}}) - 1$, $\Omega(z_{\text{coll}}) = \Omega_0 (1 + z)^3 [h/h(z)]^2$, where $[h(z)/h]^2 = \Omega_0 (1 + z)^3 + \lambda_0$ (or $\Omega_0 (1 + z)^3 + (1 - \Omega_0)(1 + z)^2$) and $c_1 = 82$ (60) and $c_2 = 39$ (32) for the flat (open) cases, $\Omega_0 + \lambda_0 = 1$ ($\Omega_0 < 1$, $\lambda_0 = 0$), respectively [21].

4.1 TIS Model vs. Numerical CDM Simulations

The TIS model reproduces many of the average properties of the halos in numerical CDM simulations quite well, suggesting that it is a useful approximation for the halos which result from more realistic initial conditions:

(1) The TIS mass profile agrees well with the fit to N-body simulations by [107] (“NFW”) (i.e. fractional deviation of $\sim 20\%$ or less) at all radii outside of a few TIS core radii (i.e. outside King radius or so), for NFW concentration parameters $4 \leq c_{\text{NFW}} \leq 7$ (Fig. 25). The flat density core of the TIS halo differs from the singular cusp of the NFW profile at small radii, but this involves only a small fraction of the halo mass, thus not affecting their good agreement outside the core. As a result, the TIS central density ρ_0 can be used to characterize the core density of cosmological halos, even if the latter have singular profiles like that of NFW, as long as we interpret ρ_0 , in that case, as an average over the innermost region.

(2) The TIS halo model predicts the internal structure of X-ray clusters found by gas-dynamical/N-body simulations of cluster formation in the CDM model. Our TIS model predictions, for example, agree astonishingly well with the mass-temperature and radius-temperature virial relations and integrated mass profiles derived empirically from the simulations of cluster formation by [46, 96] (EMN). Apparently, these simulation results are not sensitive to the discrepancy between

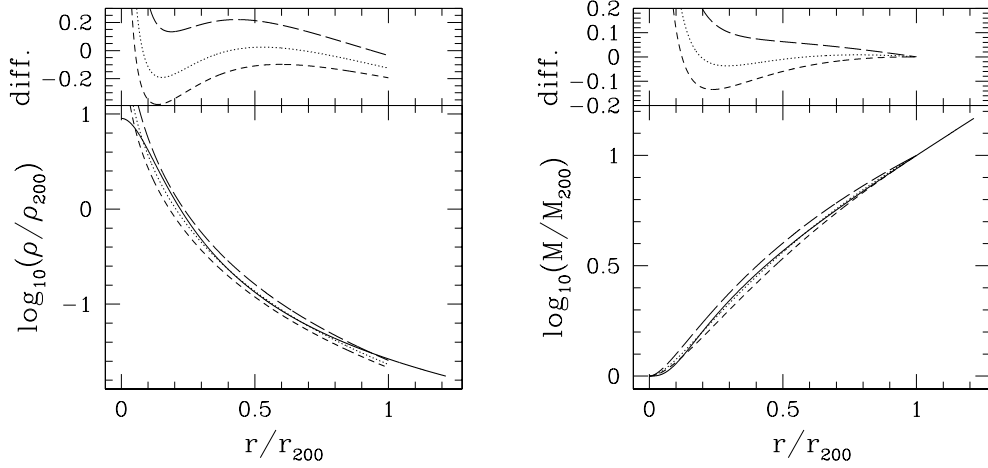


Figure 25: Profiles of density (left) and integrated mass (right), for TIS (solid) and NFW with $c_{\text{NFW}} = 4$ (short-dashed), 5 (dotted) and 7 (long-dashed) with same (r_{200}, M_{200}) .

our prediction of a small, finite density core and the N-body predictions of a density cusp for clusters in CDM. Let X be the average overdensity inside radius r (in units of the cosmic mean density) $X \equiv \langle \rho(r) \rangle / \bar{\rho}$. The radius-temperature virial relation is defined as $r_X \equiv r_{10}(X)(T/10 \text{ keV})^{1/2} \text{ Mpc}$, and the mass-temperature virial relation by $M_X \equiv M_{10}(X)(T/10 \text{ keV})^{1/2} h^{-1} 10^{15} M_{\odot}$. A comparison between our predictions of $r_{10}(X)$ and the results of EMN is given in Fig. 26. EMN obtain $M_{10}(500) = 1.11 \pm 0.16$ and $M_{10}(200) = 1.45$, while our TIS solution yields $M_{10}(500) = 1.11$ and $M_{10}(200) = 1.55$.

(3) The TIS halo model also successfully reproduces the mass - velocity dispersion relation for clusters in CDM N-body simulations and its dependence on redshift for different background cosmologies. N-body simulation of the Hubble volume $[(1000 \text{ Mpc})^3]$ by the Virgo Consortium [45] yields the following empirical relation:

$$\sigma_V = (1080 \pm 65) \left[h(z) M_{200} / 10^{15} M_{\odot} \right]^{0.33} \text{ km/s}, \quad (69)$$

where M_{200} is the mass within a sphere with average density 200 times the cosmic mean density, and $h(z) = h_0 \sqrt{\Omega_0(1+z)^3 + \lambda_0}$ is the redshift-dependent Hubble constant (assuming a flat background universe). Our TIS model predicts:

$$\sigma_V = 1103 \left[h(z) M_{200} / 10^{15} M_{\odot} \right]^{1/3} \text{ km/s}, \quad (70)$$

in excellent agreement with simulations.

(4) The TIS model successfully predicts the average virial ratio, $K/|W|$, of halos in CDM simulations. An equivalent TIS quantity, $GM_{200}/(r_{200}\sigma_V^2) = 2.176$, is

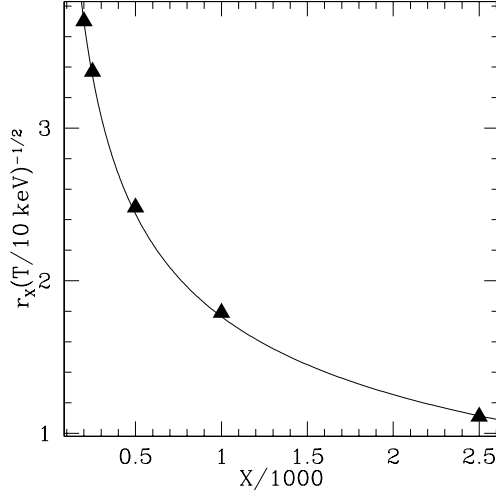


Figure 26: Cluster radius-temperature virial relation for CDM simulation results (at $z = 0$) as fit by EMN (triangles) and as predicted by TIS (solid curve).

plotted for dwarf galaxy minihalos at $z = 9$ in Fig. 27, for simulations described in [125] and [69], showing good agreement between TIS and N-body halo results. A similar plot, but of $K/|W|$ for such halos, was shown by [77] based upon N-body simulations, in which the average $K/|W|$ is close to 0.7, as predicted by the TIS model (Table 1). Those authors were apparently unaware of this TIS prediction since they compared their results with the SUS value of $K/|W|$, 0.5, and interpreted the discrepancy incorrectly as an indication that their halos were not in equilibrium.

4.2 TIS Model vs. Observed Halos

(1) The TIS profile matches the mass profiles of dark-matter-dominated dwarf galaxies deduced from their observed rotation curves [70]. Equation (61) can be integrated to yield an analytical fitting formula for the TIS rotation curve, as well, given by

$$\frac{v(r)}{\sigma_V} = \left\{ A - B + \frac{1}{\zeta} \left[bB \tan^{-1} \left(\frac{\zeta}{b} \right) - aA \tan^{-1} \left(\frac{\zeta}{a} \right) \right] \right\}^{1/2}, \quad (71)$$

where $\zeta = r/r_0$ and $v(r) = (GM[\leq r]/r)^{1/2}$. The observed rotation curves of dwarf galaxies are well fit by a density profile with a finite density core given by [24]:

$$\rho(r) = \frac{\rho_{0,B}}{(r/r_c + 1)(r^2/r_c^2 + 1)} \quad (72)$$

for which the rotation curve is given by

$$\frac{v_B(r)}{v_{*,B}} = \left\{ \frac{\ln [(\zeta_B + 1)^2(\zeta_B^2 + 1)] - 2 \tan^{-1}(\zeta_B)}{\zeta_B} \right\}^{1/2}, \quad (73)$$

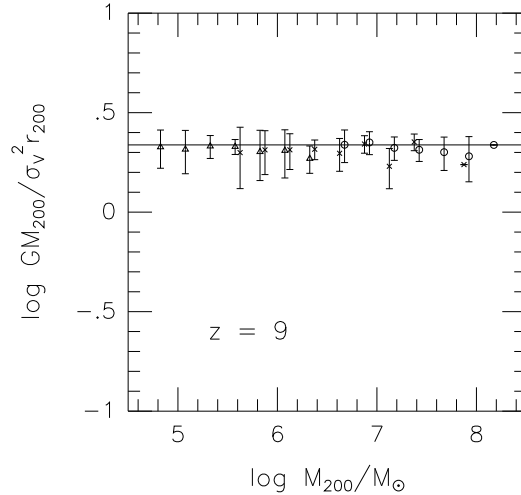


Figure 27: Virial relation $GM_{200}/(\sigma_V^2 r_{200})$ predicted by the TIS model (horizontal line) vs. mass for halos from N-body simulations [125] [with 1σ error bars].

where $\zeta_B \equiv r/r_{0,B}$ and $v_{*,B} \equiv (\pi G \rho_{0,B} r_{0,B}^2)^{1/2}$. The TIS model gives a nearly perfect fit to this profile (Fig. 28), with best fit parameters $\rho_{0,B}/\rho_{0,\text{TIS}} = 1.216$, $r_c/r_{0,\text{TIS}} = 3.134$. This best-fit TIS profile correctly predicts v_{max} , the maximum rotation velocity, and the radius, r_{max} , at which it occurs in the Burkert profile: $r_{\text{max},B}/r_{\text{max},\text{TIS}} = 1.13$, and $v_{\text{max},B}/v_{\text{max},\text{TIS}} = 1.01$. (i.e. excellent agreement).

(2) The TIS halo model can explain the mass profile with a flat density core measured by [146] for cluster CL 0024+1654 at $z = 0.39$, using the strong gravitational lensing of background galaxies by the cluster to infer the cluster mass distribution [126] (see, however [34] for an alternative view on the structure of this cluster). The TIS model not only provides a good fit to the projected surface mass density distribution of this cluster within the arcs (Fig. 29), but also predicts the overall mass, and a cluster velocity dispersion in close agreement with the value $\sigma_v = 1150$ km/s measured by [41].

4.3 Making Tracks on the Cosmic Virial Plane

The TIS model yields $(\rho_0, \sigma_V, r_t, r_0)$ uniquely as functions of (M, z_{coll}) . This defines a “cosmic virial plane” in (ρ_0, r_0, σ_V) -space and determines halo size, mass, and collapse redshift for each point on the plane. In hierarchical clustering models like CDM, M is statistically correlated with z_{coll} . This determines the distribution of points on the cosmic virial plane. We can combine the TIS model with the Press-Schechter (PS) approximation for $z_{\text{coll}}(M)$ – typical collapse epoch for halo of mass M – to predict correlations of observed halo properties.

According to the PS approximation, the fraction of matter in the universe which is condensed into objects of mass $\geq M$ at a given epoch is $f_{\text{coll}}(\geq M) =$

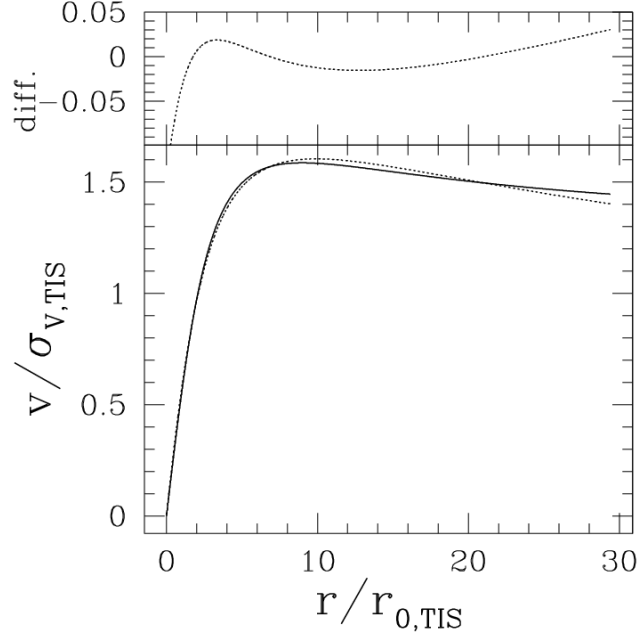


Figure 28: Rotation Curve Fit. Solid line = Best fit TIS; Dashed line = Burkert profile.

$\text{erfc}(\nu/2^{1/2})$, where $\nu \equiv \delta_{\text{crit}}/\sigma(M)$, $\sigma(M)$ is the standard deviation of the density fluctuations at that epoch, according to linear theory, when filtered on mass scale M , and δ_{crit} is the fractional overdensity of a top-hat perturbation when this linear theory is extrapolated to the time of infinite collapse in the exact nonlinear solution. The “typical” collapse epoch for a given mass is that for which $\sigma(M) = \delta_{\text{crit}}$ (i.e. $\nu = 1$). For a given z_{coll} , this defines a typical mass scale: $M_{\star} \equiv M(\nu = 1)$.

If we approximate the power-spectrum of density fluctuations at high redshift (e.g. just after recombination) as a power-law in wavenumber k , $P(k) \propto k^n$, and define a mass $M \propto k^{-3}$, then $F \propto M^{-(3+n)/6}$ if $n = n_{\text{eff}} \equiv -3(2y_F + 1)$, where $y_F \equiv (d \ln F / d \ln M)_{\text{exact}}$ at the relevant mass scale. For all masses in the EdS case and for masses which collapse early in the low-density, matter-dominated and flat, universes, y_F reduces to $y_{\sigma} \equiv (d \ln \sigma / d \ln M)_{\text{exact}}$, and $(1 + z_{\text{coll}}) \propto \sigma(M) \propto M^{-(3+n)/6}$, where $\sigma(M)$ is evaluated at the same cosmic time for all masses. The dependence of n_{eff} and z_{coll} on M for 1- σ fluctuations is shown in Figure 31 for Λ CDM, along with the approximate n_{eff} which results if y_F is replaced by y_{σ} , which shows that the latter is a very good approximation for all masses $M < 10^{12} M_{\odot} h^{-1}$.

(1) The combined (TIS+PS) model explains the observed correlation of the maximum circular velocity v_{max} and its location r_{max} in the rotation curves of dwarf

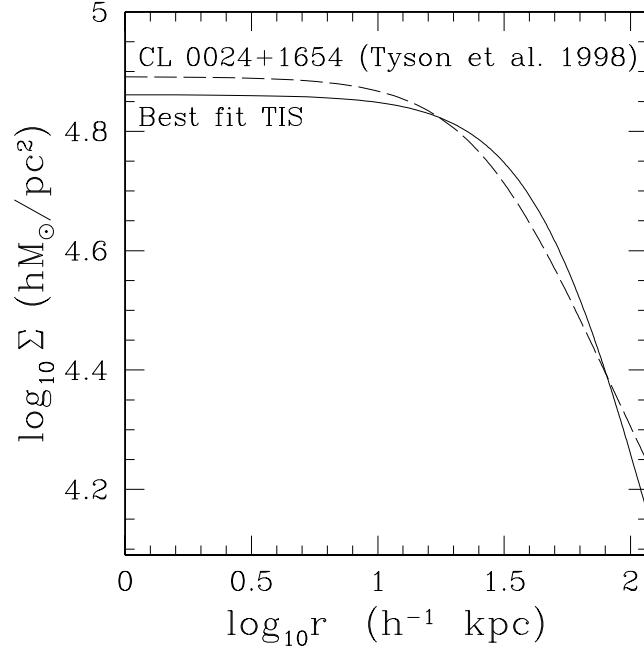


Figure 29: Projected surface density of cluster CL 0024+1654 inferred from lensing measurements, together with the best-fit TIS model.

spiral and LSB galaxies, with preference for the currently favored Λ CDM model with no tilt of the power spectrum of the primordial density fluctuations [70] (Fig. 30). According to [103], the observed $v_{\max} - r_{\max}$ correlation can be expressed as follows:

$$v_{\max} = 9.81(r_{\max}/1 \text{ kpc})^{2/3} \text{ kms}^{-1}. \quad (74)$$

Our results for the Λ CDM case indicate that the galaxies which make up the $v_{\max} - r_{\max}$ data points in Figure 30 collapsed at redshifts $1 < z_{\text{coll}} < 6$ with masses in the range $8 \times 10^9 < M_0/(M_{\odot} h^{-1}) < 3 \times 10^{11}$. Hence, the precollapse fluctuation growth rate is approximately EdS, and we can let $\Omega(z_{\text{coll}}) = 1$. In that case, $(1 + z_{\text{coll}}) \propto \sigma(M) \propto M^{-(3+n)/6}$, $r_{\max} \propto M^{(5+n)/6} \Omega_0^{-1/3}$ and $v_{\max} \propto M^{(1-n)/12} \Omega_0^{1/6}$, which combine to yield

$$v_{\max} = v_{\max,*} (r_{\max}/r_{\max,*})^{(1-n)/[2(5+n)]}, \quad (75)$$

where $v_{\max,*}$ and $r_{\max,*}$ are for a $1\text{-}\sigma$ fluctuation of fiducial mass M_* , with $(1 + z_{\text{coll}}) = (1 + z_{\text{rec}})\sigma(M_*, z_{\text{rec}})/\delta_{\text{crit}}$, where $\delta_{\text{crit}} = 1.6865$ and $\sigma(M_*, z_{\text{rec}})$ is the value of $\sigma(M_*)$ evaluated at the epoch of recombination z_{rec} [i.e. early enough that $(1 + z)\sigma$ is independent of z]. Over the relevant mass range $M = 10^{10 \pm 1} h^{-1} M_{\odot}$, $n_{\text{eff}} \approx -2.4 \pm 0.1$ for our Λ CDM case. For $M_* = 10^{10} h^{-1} M_{\odot}$, our COBE-normalized, flat Λ CDM case ($\Omega_0 = 0.3, h = 0.65$) yields $(1 + z_{\text{rec}})\sigma(M_*, z_{\text{rec}}) = 5.563$, so $(1 + z_{\text{coll}}) = 3.30$,

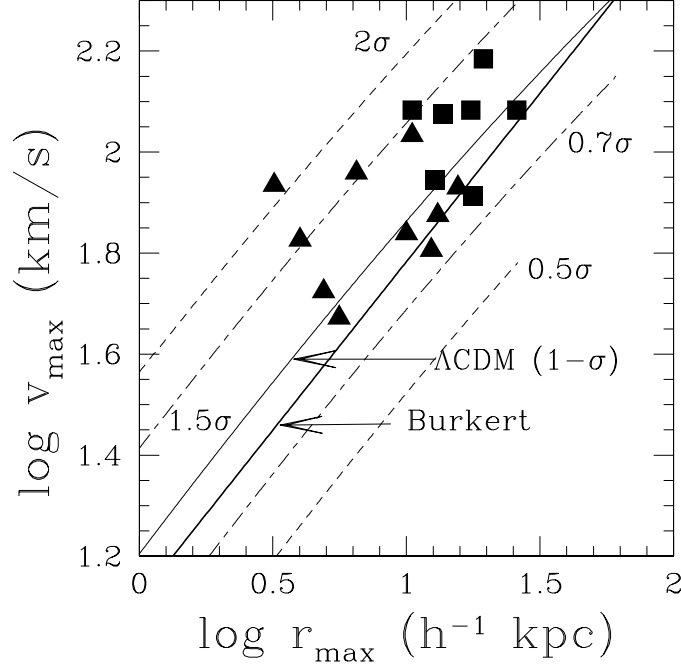


Figure 30: v_{\max} - r_{\max} correlation predicted by (TIS+PS) model for Λ CDM [COBE normalized, $\Omega_0 = 1 - \lambda_0 = 0.3, h = 0.65$; no tilt, i.e. primordial power-spectrum index $n_p = 1$), for halos formed from $\nu - \sigma$ fluctuations, as labelled with ν -values. All curves are (TIS+PS) results, except curve labelled “Burkert” is a fit to data [24]. Observed dwarf galaxies (triangles) and LSB galaxies (squares) from [88].

$v_{\max,*} = 53.2 \text{ km s}^{-1}$ and $r_{\max,*} = 5.59 h^{-1} \text{ kpc}$. With these values and $n_{\text{eff}} = -2.4$, equation (75) yields the TIS model analytical prediction

$$v_{\max} = (13.0 \text{ km s}^{-1})(r_{\max}/1 \text{ kpc})^{0.65}, \quad (76)$$

remarkably close to the observed relation in equation (74).

(2) The TIS+PS model also predicts the correlations of central mass and phase-space densities, ρ_0 and $Q \equiv \rho_0/\sigma_V^3$, of dark matter halos with their velocity dispersions σ_V , with data for low-redshift dwarf spheroidals to X-ray clusters again most consistent with Λ CDM with no tilt [127] (Fig. 32).⁵ A fully analytical approximation for these correlations was also derived in [127] by combining the TIS+PS model with the power-law model for $P(k)$ described above, which yields $\rho_0 \propto M^{-(n+3)/2}$,

⁵There have also been claims that $\rho_0 = \text{const}$ for all cosmological halos, independent of their mass, as expected for certain types of SIDM [49, 78]. This claim, however, is not supported by most current data (Fig. 32).

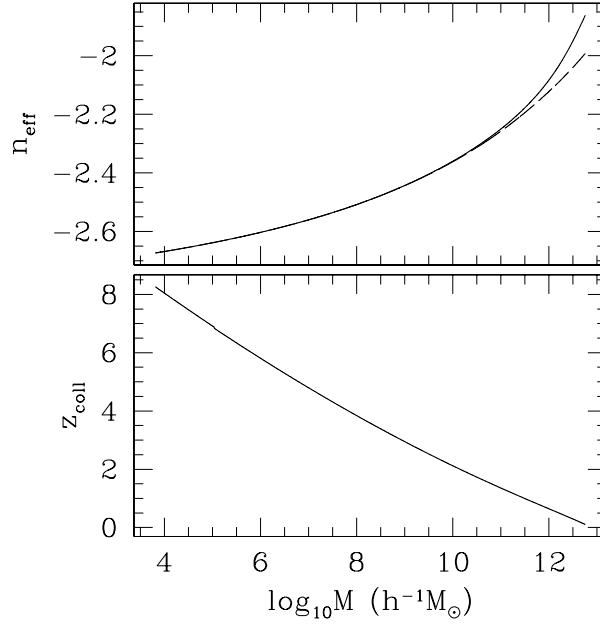


Figure 31: (a)(upper) Effective logarithmic slope, n_{eff} , of the density fluctuation power spectrum versus halo mass $M = M_*$ (i.e. for $1\text{-}\sigma$ fluctuations) for ΛCDM , based upon y_F (solid curve) and the approximation which uses y_σ , instead (dashed). (b) (lower) Typical collapse redshift z_{coll} for halos of mass M_* in ΛCDM .

$\sigma_V \propto M^{(1-n)/12}$, and $Q \propto M^{-(n+7)/4}$. These combine to give

$$Q = Q_*(\sigma_V/\sigma_{V,*})^{\alpha-3}, \quad (77)$$

and

$$\rho_0 = \rho_{0,*}(\sigma_V/\sigma_{V,*})^\alpha, \quad (78)$$

where $\alpha \equiv 6(n+3)/(n-1)$, except that $\alpha = 0$ for $M > M_*(z=0)$ (e.g. for untilted ΛCDM $M_*(z=0) \approx 10^{13}M_\odot$), for which $z_{\text{coll}} = 0$ is assumed.

Similarly, we can compare different flavors of the ΛCDM model, with no tilt ($n_p = 1$), slight tilts ($n_p = 0.9$ or 1.1) and with the “running” power-spectrum index suggested by the first year Wilkinson Microwave Anisotropy Probe results [134] $\left[n_p(k) = 0.93 - 0.015 \ln\left(\frac{k}{0.05 \text{ Mpc}^{-1}}\right)\right]$ (Fig. 33). In this case the untilted ΛCDM model is again moderately preferred.

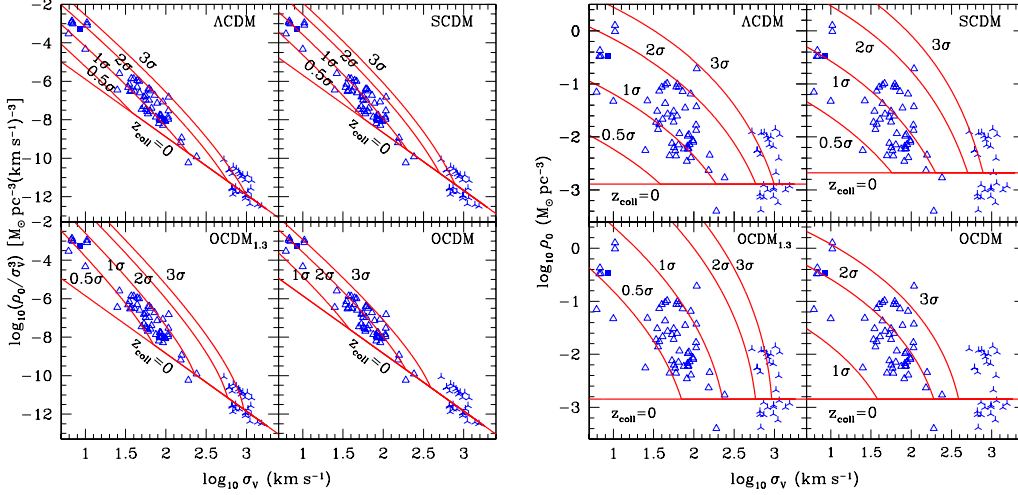


Figure 32: (a) (left) Maximum phase-space density $Q = \rho_0/\sigma_V^3$ versus velocity dispersion σ_V for halos observed today, as predicted for various CDM universes by the TIS model combined with the Press-Schechter approximation (TIS + PS) (solid curves) for halos formed from ν - σ fluctuations, as labelled with the values of ν , for $\nu = 0.5, 1, 2$, and 3 . In each panel, lines representing halos of different mass which collapse at the same redshift are shown for the case $z_{\text{coll}} = 0$, as labelled. Each panel represents different assumptions for the background universe and primordial density fluctuations, as labelled: COBE-normalized Λ CDM ($\lambda_0 = 0.7$, $\Omega_0 = 0.3$) (upper left), cluster-normalized SCDM ($\Omega_0 = 1$) (upper right), and COBE-normalized OCDM ($\Omega_0 = 0.3$) (lower panels), all assuming $h = 0.7$ and primordial power spectrum index $n_p = 1$ (i.e. untilted), except for $\text{OCDM}_{1.3}$, for which $n_p = 1.3$. Data points represent observed galaxies and clusters, taken from the following sources: (1) 49 late-type spirals of type Sc-Im and 7 dSph galaxies from [86, 87] (open triangles); (2) Local Group dSph Leo I from [95] (filled square); (3) 28 nearby clusters, σ_V from [59] and [76], and ρ_0 from [97] (crosses). (b) (right) Same as (a), except for ρ_0 vs. σ_V .

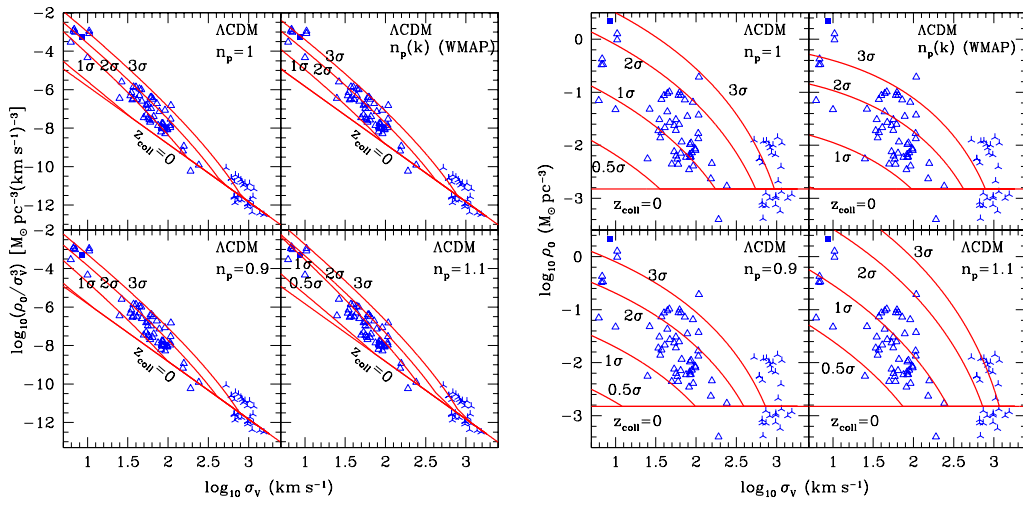


Figure 33: Same as Fig. 32, but for ΛCDM variants: (top left) untilted ΛCDM ($n_p = 1$), (top right) ΛCDM with running power-spectrum index $n_p = n_p(k)$ according to the best WMAP fit, (bottom left) ΛCDM with $n_p = 0.9$, and (bottom right) ΛCDM with $n_p = 1.1$.

5 Gravitational lensing by CDM halos: Singular vs. nonsingular profiles

5.1 INTRODUCTION

The gravitational lensing of distant sources has in recent years become one of the most powerful tools in observational cosmology [13, 133]. Since the effects of gravitational lensing depend upon the redshift of the source, the cosmological background, and the distribution of matter in the universe, they can be used to constrain the cosmological parameters and the primordial power spectrum of density fluctuations from which structure originates. In addition, many of the effects produced by gravitational lenses, such as image multiplicity, separations, and time delay, depend strongly upon the matter distribution inside the lenses. Hence, measurements of these effects can provide a unique tool for probing the matter distribution inside collapsed objects like galaxies and clusters, providing the only direct measurement of their dark matter content, and constraining the theory of their formation and evolution.

Until recently, the internal structure of halos adopted in lensing studies was generally some gravitational equilibrium distribution, either singular or nonsingular (e.g., King model, singular isothermal sphere, pseudo-isothermal sphere), not necessarily motivated directly by the theory of cosmological halo formation [17, 62, 72, 73, 83, 104, 114, 115, 116, 121, 145, 155]. As the theory of halo formation in the CDM model has advanced in recent years, however, the halo mass profiles adopted for lensing models have been refined to reflect this theory. Numerical simulations of large-scale structure formation in Cold Dark Matter (CDM) universes predict that galaxies and clusters have a singular density profile which approaches a power law $\rho \propto r^{-n}$ at the center, with the exponent n ranging from 1 to 1.5 [30, 53, 54, 55, 58, 67, 100, 102, 107, 108, 74, 81, 112, 144]. These results are in apparent conflict with observations of rotation curves of dark-matter-dominated dwarf galaxies and low surface brightness galaxies, which favor a flat-density core [26, 99, 100, 118]. On the scale of clusters of galaxies, observations of strong gravitational lensing of background galaxies by foreground clusters also favor the presence of a finite-density core in the centers of clusters [146, 57, 123].

Lensing by the two kinds of halo mass profiles, singular versus flat-core, will be different. This has led to attempts to predict the differences expected if the halos have the singular cusp of the Navarro-Frenk-White (NFW) or Moore profiles or else a profile with a flat core [79, 83, 90, 121, 140, 153]. Several authors have studied the effect of lensing by halos with a flat-density core [72, 73, 83, 114, 115, 116] or by NFW or Moore profiles that have been generalized, so that the inner slope of the density profile is arbitrary [79, 90, 121, 153]. These particular density profiles are essentially mathematical conveniences without physical motivation. There is no underlying theoretical model in these cases that was used to predict the value of the core radius or the departure of the inner slope of the density profile from the value

found by N-body simulations of CDM. By contrast, the TIS model is based on a set of physical assumptions concerning the origin, evolution, and equilibrium structure of halos in CDM universes. Observations of gravitational lenses have the potential to distinguish between the TIS profile and singular ones like the NFW profile, as several observable properties of gravitational lenses will be strongly affected by the presence, or absence of a central cusp in the density profile. One example of an important observable that can distinguish between various density profiles is the parity of the number of images. Lenses with nonsingular density profiles, such as the TIS, obey the *odd number theorem*. The number of images of a given source is always odd, unless the source is extended and saddles a caustic (see [124], p. 172). Lenses with singular profiles, like the singular isothermal sphere, the NFW profile, or the Moore profile, need not obey this theorem, even for point sources. Most observed multiple-image gravitational lenses have either 2 or 4 images, and this may argue against profiles with a central core [121]. There are, however, other possible explanations for the absence of a third or fifth image. That image tends to be very close to the optical axis, and might be hidden behind the lens itself. Also, it is usually highly demagnified, and might be too faint to be seen.

In this section, we derive all the lensing properties of the TIS. We also compare the TIS with three other density profiles: The Navarro-Frenk-White (NFW) density profile, the Singular Isothermal Sphere (SIS), and the Schwarzschild Lens⁶. To compare the lensing properties of these various lens models, we focus on one particular cosmological model, the currently favored COBE-normalized Λ CDM model with $\Omega_0 = 0.3$, $\lambda_0 = 0.7$, and $H_0 = 70 \text{ km s}^{-1} \text{ Mpc}^{-1}$ (this model is also cluster-normalized).

5.2 THE DENSITY PROFILES

5.2.1 The Radial Density Profiles

We will compute the lensing properties of halos with the TIS density profile, as well-approximated by equation (61), and compare them with the properties derived for three comparison profiles. The first one is the Navarro, Frenk, and White (NFW) density profile,

$$\rho(r) = \frac{\rho_{\text{NFW}}}{(r/r_{\text{NFW}})(r/r_{\text{NFW}} + 1)^2}, \quad (79)$$

where ρ_{NFW} is a characteristic density and r_{NFW} is a characteristic radius. We will also consider the Singular Isothermal Sphere (SIS) density profile,

$$\rho(r) = \frac{\sigma_V^2}{2\pi G r^2}, \quad (80)$$

where σ_V is the velocity dispersion and G is the gravitational constant. This model might not represent actual halos very well, but it is a well-studied profile that has

⁶A point mass

important theoretical value. Finally, for completeness, we will also consider the Schwarzschild lens,

$$\rho(r) = M_{\text{Sch}}\delta^3(r) \quad (81)$$

where M_{Sch} is the lens mass and δ^3 is the three-dimensional delta function.

In order to compare the predictions for halo lensing for different halo density profiles, we must relate the parameters which define one profile to those which define another. For this purpose, we shall use the same approach as [152]. The virial radius r_{200} of a halo located at redshift z is defined, as usual, as being the radius inside which the mean density is equal to 200 times the critical density $\rho_c(z) \equiv 3H^2(z)/8\pi G$ at that redshift [where $H(z)$ is the Hubble parameter]. The mass M_{200} inside that radius is given by

$$M_{200} = \frac{800\pi\rho_c(z)r_{200}^3}{3}. \quad (82)$$

When comparing the lensing properties of different density profiles, we will consider halos that are located at the same redshift $z = z_L$ (the lens redshift) and have the same value of r_{200} . By definition, these halos will also have the same value of M_{200} . By stretching the terminology, we will refer to M_{200} as “the mass of the halo.” This point needs to be discussed. For the Schwarzschild lens, M_{200} is indeed the mass of the halo. The SIS density profile drops as r^{-2} at large r , and the mass therefore diverges unless we introduce a cutoff. The halo mass will then be equal to M_{200} only if the cutoff is chosen to be r_{200} . The NFW density profile drops as r^{-3} , hence the total mass diverges logarithmically, and this profile also needs a cutoff. The TIS density profile drops asymptotically as r^{-2} , but the TIS model includes a cutoff. This cutoff is located a radius $r_t \approx 1.2r_{200}$, and the mass inside the cutoff is $M_t = 1.168M_{200}$. In any case, a rigorous definition of the halo mass would require an unambiguous determination of the boundary between the halo and the background matter (such determination exists only for the TIS model), as well as dealing with the fact that the assumption of spherical symmetry that enters in these models most likely breaks down for real halos at large enough radii. Treating M_{200} as the actual mass of the halo is the best compromise.

For a given halo mass M_{200} , redshift z , and cosmological background model, the density profiles for the SIS and Schwarzschild lens are fully determined. For the SIS, we integrate equation (80) between $r = 0$ and $r = r_{200}$, and get

$$M_{200} = \frac{2\sigma_V^2 r_{200}}{G}. \quad (83)$$

Combining equations (82) and (83), we get

$$\sigma_V = \left[\frac{100\pi G^3 \rho_c(z) M_{200}^2}{3} \right]^{1/6}. \quad (84)$$

For the Schwarzschild lens, M_{Sch} is simply given by M_{200} .

For the NFW profile, the concentration parameter c must be specified in addition to the parameters M_{200} and z . The value of c is not completely independent of the other parameters since there is a statistical expectation that c is correlated with M_{200} and z . However, for any individual halo, c is not known a priori. To determine c for a given halo, we will use the typical value expected from the statistical correlation of c with halo mass and the redshift of observation of the halo, $z_{\text{obs}} = z_L$, according to the formalism of [44]. Once the value of c is known, we can compute the parameters of the profile. The characteristic radius of the NFW profile is given by

$$r_{\text{NFW}} = r_{200}/c, \quad (85)$$

and the characteristic density ρ_{NFW} is given by

$$\rho_{\text{NFW}} = \frac{200c^3\rho_c(z)}{3[\ln(1+c) - c/(1+c)]}. \quad (86)$$

The TIS halo is uniquely specified by the central density ρ_0 and core radius r_0 . These parameters are functions of the mass M_{200} and redshift z , but in this case, z is not the redshift z_L where the halo is located, but rather the collapse redshift z_{coll} where the halo formed, which can be larger than z_L . We will assume that a TIS halo which formed at some $z_{\text{coll}} \geq z_L$ did not evolve between z_{coll} and z_L . For a given M_{200} and z_{coll} , the parameters ρ_0 and r_0 are determined as follows. The central density ρ_0 depends only on z_{coll} ,

$$\rho_0 = 1.8 \times 10^4 \rho_c(z_{\text{coll}}), \quad (87)$$

while $M_t = 1.167M_{200} = 772.6\rho_0 r_0^3$, or

$$r_0 = 1.51 \times 10^{-3} (M_{200}/\rho_0)^{1/3}. \quad (88)$$

Fig. 34 shows a comparison of the various profiles, for halos with the same values of r_{200} and M_{200} (the TIS curve is for $z_{\text{coll}} = z_L$).

The equations describing the lensing properties of the Schwarzschild lens, the singular isothermal sphere, and the NFW profile can be found in the literature. For brevity, we will not repeat these equations here. We refer the reader to [124] for the Schwarzschild lens (§8.1.2) and the singular isothermal sphere (§8.1.4), and to [29] and [152] for the NFW profile.

5.2.2 The Interior Mass Profile

The projected surface density is given by

$$\Sigma(\xi) = \int_{-\infty}^{\infty} \rho(r) dz, \quad (89)$$

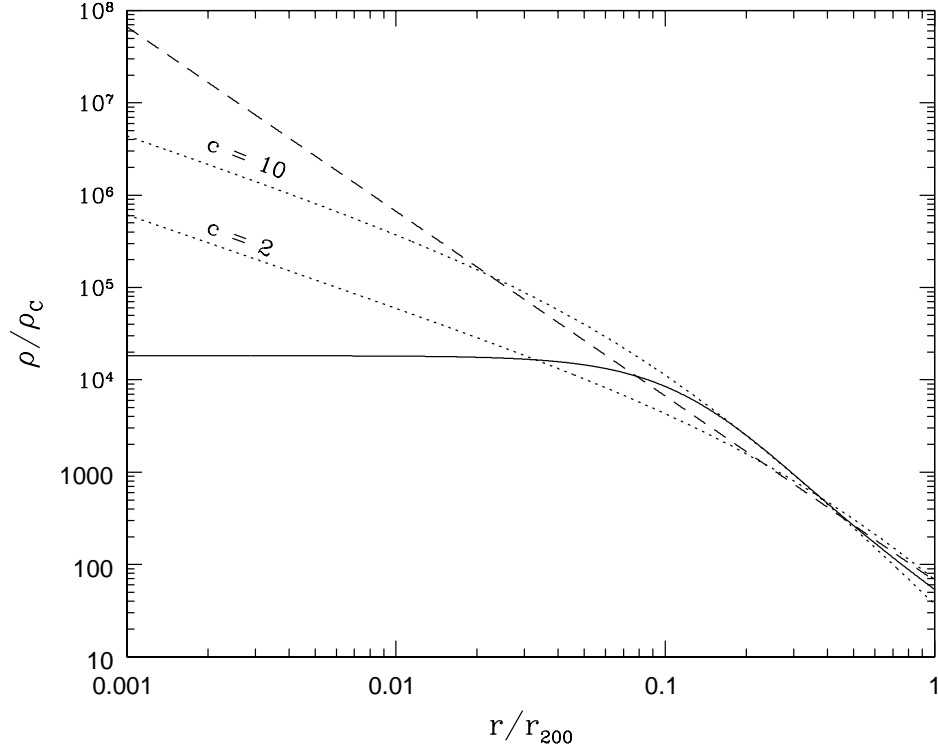


Figure 34: Radial density profiles, for 4 different halos with the same values of r_{200} and M_{200} . Solid curve: TIS; dotted curves: NFW profiles with concentration parameters $c = 2$ and 10 (as labeled); dashed curve: SIS.

where ξ is the projected distance from the center of the halo, and $z = (r^2 - \xi^2)^{1/2}$. For the TIS, we substitute equation (61) in equation (89), and get

$$\Sigma_{\text{TIS}}(\xi) = \pi \rho_0 r_0^2 \left[\frac{A}{(a^2 r_0^2 + \xi^2)^{1/2}} - \frac{B}{(b^2 r_0^2 + \xi^2)^{1/2}} \right] \quad (90)$$

[68, 106]. For spherically symmetric lenses, one important quantity is the interior mass $M(\xi)$ inside a cylinder of projected radius ξ centered around the center of the lens. This quantity is given by

$$M(\xi) = 2\pi \int_0^\xi \Sigma(\xi') \xi' d\xi'. \quad (91)$$

we substitute equation (90) in equation (91), and get

$$M_{\text{TIS}}(\xi) = 2\pi^2 \rho_0 r_0^3 \left[A(a^2 + \xi^2/r_0^2)^{1/2} - B(b^2 + \xi^2/r_0^2)^{1/2} - Aa + Bb \right]. \quad (92)$$

Fig. 35 shows a comparison of $M(\xi)$ for various halos with the same values of r_{200} and M_{200} .

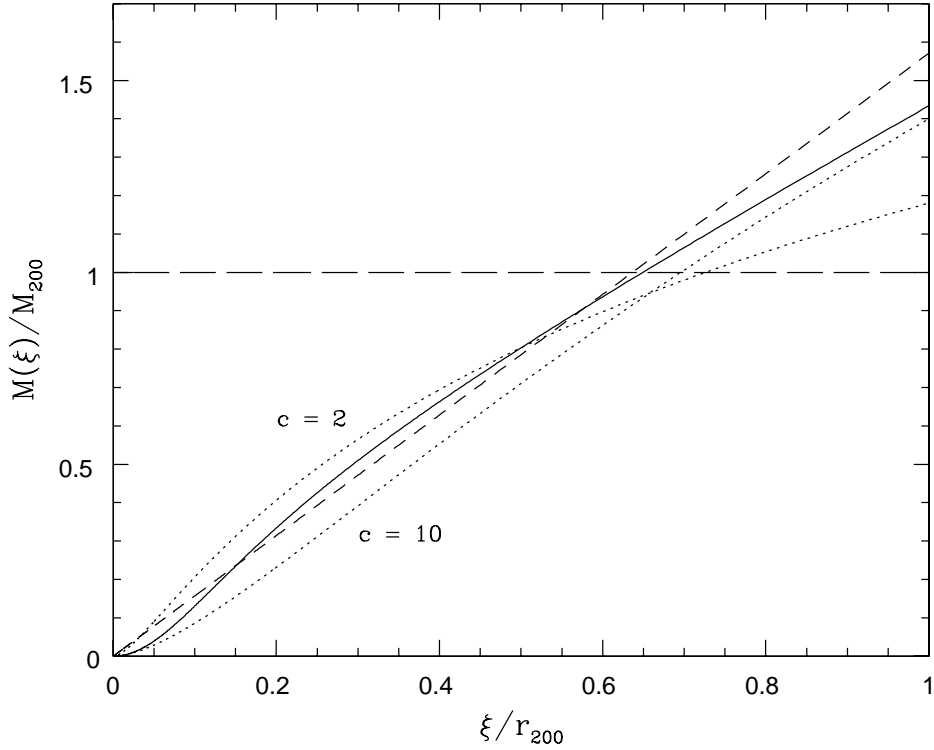


Figure 35: Interior mass profiles, for 5 different halos with the same values of r_{200} and M_{200} . Solid curve: TIS; dotted curves: NFW profiles with concentration parameters $c = 2$ and 10 (as labeled); short-dashed curve: SIS; long-dashed curve: Schwarzschild lens.

5.3 THE LENS EQUATION

Fig. 36 illustrates the lensing geometry. The quantities η and ξ are the position of the source on the source plane and the image on the image plane, respectively, $\hat{\alpha}$ is the deflection angle, and D_L , D_S , and D_{LS} are the angular diameter distances between observer and lens, observer and source, and lens and source, respectively. The lens equation is

$$\eta = \frac{D_S}{D_L} \xi - D_{LS} \hat{\alpha} \quad (93)$$

([124], eq. [2.15b]). Notice that since the lens is axially symmetric, we can write the quantities η , ξ , and $\hat{\alpha}$ as scalars instead of 2-component vectors. We nondimensionalize the positions and deflection angle, as follows:

$$y = \frac{D_L \eta}{D_S r_0}, \quad (94)$$

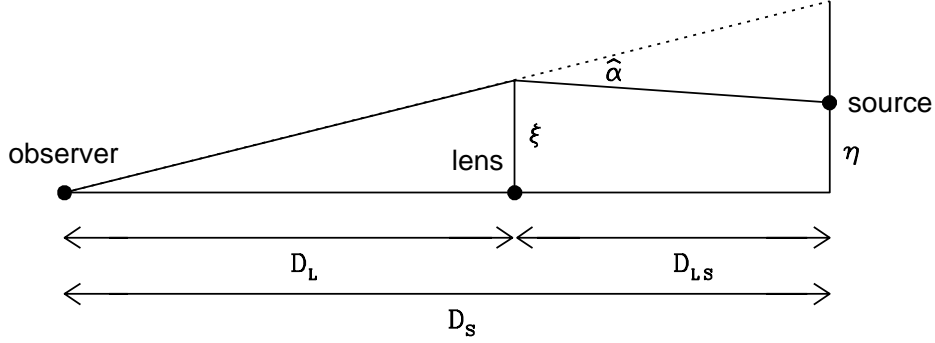


Figure 36: The lensing geometry: the dots indicate the location of the observer, lensing galaxy, and source. ξ and η are the positions of the image and the source, respectively, and $\hat{\alpha}$ is the deflection angle. The angular diameter distances D_L , D_{LS} , and D_S are also indicated.

$$x = \frac{\xi}{r_0}, \quad (95)$$

$$\alpha = \frac{D_L D_{LS} \hat{\alpha}}{D_S r_0}. \quad (96)$$

The lens equation reduces to

$$y = x - \alpha(x). \quad (97)$$

The deflection angle is given by

$$\alpha(x) = \frac{M(r_0 x)}{\pi r_0^2 \Sigma_{\text{crit}} x}. \quad (98)$$

([124], eq. [8.3]), where Σ_{crit} is the critical surface density, given by

$$\Sigma_{\text{crit}} = \frac{c^2 D_S}{4\pi G D_L D_{LS}}, \quad (99)$$

where c is the speed of light. We substitute equation (92) into equation (98), and get

$$\alpha_{\text{TIS}}(x) = \frac{2ab\kappa_c}{(Ab - Ba)x} \left[A(a^2 + x^2)^{1/2} - B(b^2 + x^2)^{1/2} - Aa + Bb \right]. \quad (100)$$

where κ_c is the central convergence of the TIS, defined by

$$\kappa_c \equiv \frac{\Sigma(\xi = 0)}{\Sigma_{\text{crit}}} = \frac{\pi \rho_0 r_0}{\Sigma_{\text{crit}}} \left(\frac{A}{a} - \frac{B}{b} \right) \quad (101)$$

(see also [28]).

5.4 CRITICAL CURVES AND CAUSTICS

The lensing properties of a halo depend on its radial density profile $\rho(r)$, the redshift z_L where it is located, the source redshift z_S , and the source position η . In the remainder of this section, we will simplify the problem by fixing the redshifts z_L and z_S . We are primarily interested here in lensing by cluster-scale halos. Most of these halos are located in the redshift range $0.2 \leq z_L \leq 0.6$, and none are located at redshift $z_L > 0.6$. [151] In what follows, we will assume that halos are located at $z_L = 0.5$. We will also assume that the source is located at redshift $z_S = 3$. This is not a very constraining assumption, because the lensing properties vary weakly with the source redshift for $z_S \gg 1$.

For the Schwarzschild lens, SIS, and NFW profile, the density profile $\rho(r)$ is fully determined by the values of M_{200} and z_L . For the TIS, we also need to specify the collapse redshift z_{coll} . We will consider three particular values, $z_{\text{coll}} = 0.5, 1.0$, and 1.5 .

5.4.1 Solutions

The determination of the critical curves is quite trivial for axially symmetric lenses. Tangential and radial critical curves are defined respectively by

$$\frac{m(x_t)}{x_t^2} \equiv \frac{\alpha(x_t)}{x_t} = 1, \quad (102)$$

$$\left[\frac{d(m/x)}{dx} \right]_{x=x_r} \equiv \left[\frac{d\alpha}{dx} \right]_{x=x_r} = 1. \quad (103)$$

([124] eq. [8.3]), where $m(x) = M(r_0 x) / \pi r_0^2 \Sigma_{\text{crit}}$ is the dimensionless interior mass. For the Schwarzschild lens and the SIS, the solutions are $x_t = 1$, and there are no real solutions for x_r . For the NFW and TIS models, equations (102) and (103) have to be solved numerically for x_t and x_r . The solutions for the TIS are plotted in Fig. 37, as functions of κ_c . Also plotted is the radial caustic radius y_r , obtained by substituting the value of x_r into equation (97). (The value of y_r we obtain is actually negative, because the source and image are on opposite sides of the lens. The actual radius of the caustic circle, then, is the absolute value of y_r .) Both x_t and $|y_r|$ increase rapidly with κ_c , while the value of x_r levels off. Fig. 38 shows the angular radii of the tangential and radial critical circles, $\theta_r = \xi_r / D_L$ and $\theta_t = \xi_t / D_L$, in arc seconds as functions of the mass of the lens. For spherically symmetric lenses, multiple images (and thus critical circles) are possible only if the central convergence $\kappa(0) \equiv \Sigma(0) / \Sigma_{\text{crit}}$ exceeds unity ([124], p. 236, theorem [e]). For the Schwarzschild lens, SIS, and NFW profile, the central convergence diverges, hence these profiles can always produce multiple images. But for the TIS, the central convergence $\kappa(0) \equiv \kappa_c$ is finite, and multiple images can be produced only if $\kappa_c > 1$. This explains the sharp low-mass cutoff seen in Fig. 38 for the TIS (solid curves).

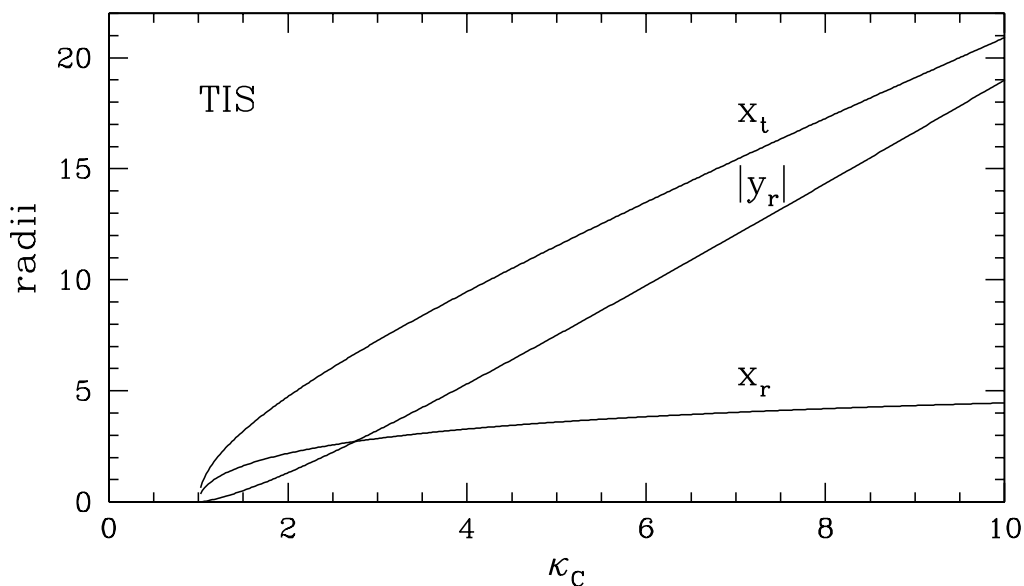


Figure 37: Radii of the radial critical circle, x_r , tangential critical circle, x_t , and radial caustic, y_r , versus κ_c , for the TIS.

The value of θ_t for the Schwarzschild lens is called the Einstein radius θ_E . It is often used to estimate the characteristic scale of image features caused by strong lensing (e.g. ring radius, radial location of arc, image separations) and to estimate the size of the region within which the mass responsible for that strong lensing must be concentrated. Since lensing halos are not actually point masses, however, the angular radius θ_{ring} of the actual Einstein ring which results if the source is located along the line of sight through the lens center will usually differ from the Einstein radius θ_E , assuming that the lens mass distribution is actually capable of producing a ring. As we see in Fig. 38, θ_E significantly exceeds θ_t for all profiles considered (TIS, NFW profile, and SIS) for all masses considered. Hence, a mass estimate based on assuming that the scale of image features is of order θ_E will underestimate the actual mass of the lens, unless the lens happens to be a Schwarzschild lens.

A source located behind the lens will produce multiple images if $y < y_r$. The angular cross section for multiple imaging is therefore

$$\sigma_{\text{m.i.}} = \pi \left(\frac{\eta_r}{D_S} \right)^2 = \pi \left(\frac{y_r \xi_0}{D_L} \right)^2. \quad (104)$$

In Fig. 39, we plot the ratio of the cross sections for the NFW and TIS profiles. At low masses, $M < 5 \times 10^{15} M_\odot$ for $z_{\text{coll}} = 0.5$, $M < 1.2 \times 10^{15} M_\odot$ for $z_{\text{coll}} = 1.0$, $M < 3 \times 10^{14} M_\odot$ for $z_{\text{coll}} = 1.5$, the ratios are less than unity, indicating that a distribution of lenses described by the NFW profile would be more likely to produce

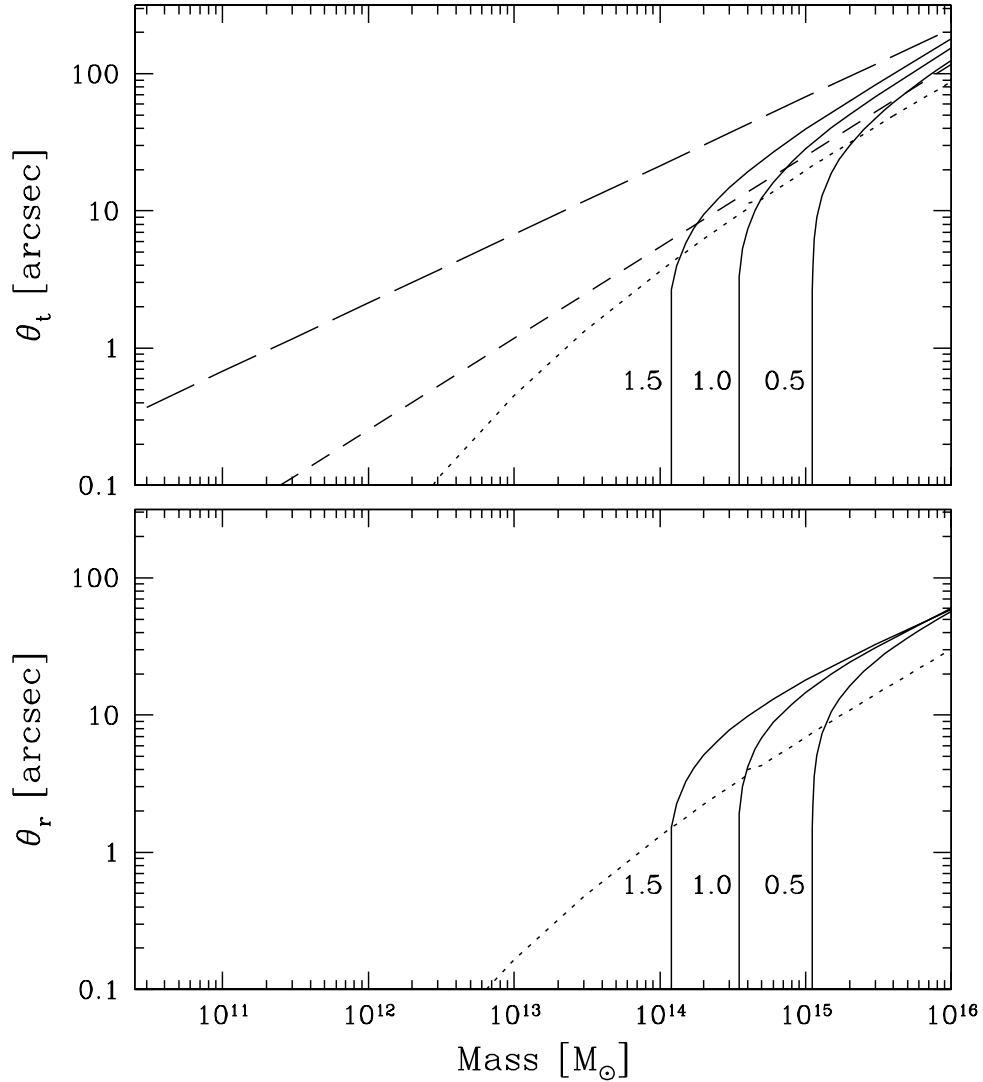


Figure 38: Angular radius of the tangential critical curve (top) and radial critical curve (bottom), versus lens mass, for the TIS (solid curves), the NFW profile (dotted curves), the SIS (short dashed curves) and the Schwarzschild lens (long dashed curves). For the TIS, the values of z_{coll} are indicated.

cases with multiple images than if the same distribution is described by the TIS model. This trend is reversed at higher masses, and a TIS is more likely to produce multiple images than a NFW profile of the same mass.

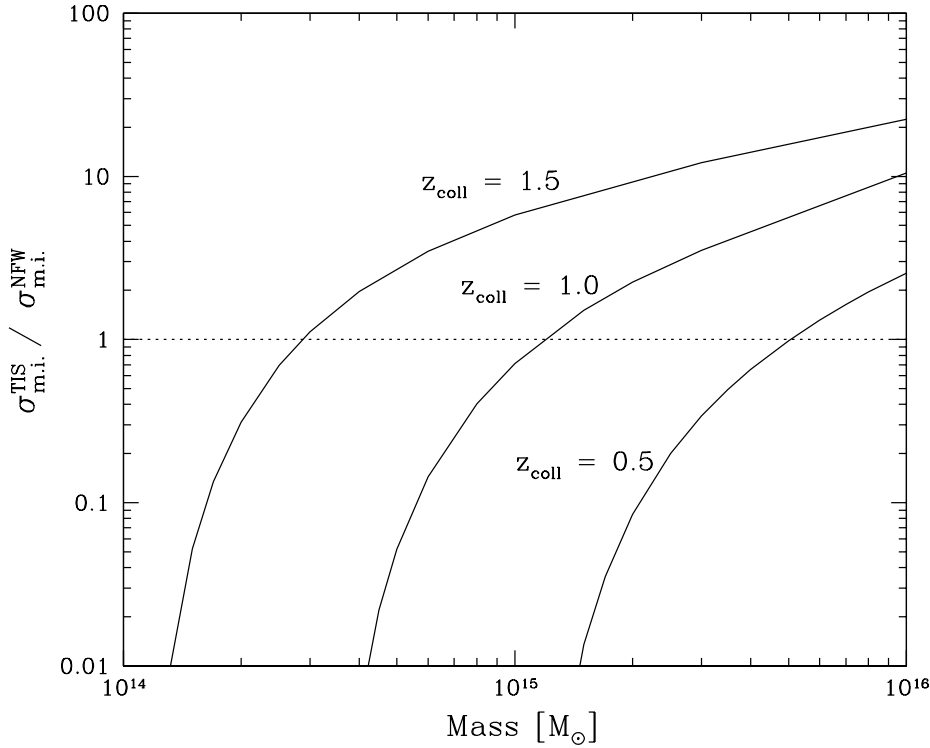


Figure 39: Ratio of the cross sections for multiple imaging by the TIS and the NFW profile, versus lens mass. The values of z_{coll} for the TIS are indicated.

5.4.2 Illustrative Example

Using a simple ray-tracing algorithm, we computed the image(s) of a circular source of diameter $\Delta y = 1$, created by a TIS with central convergence $\kappa_c = 4.015$. The results are shown in Fig. 40 for 6 different locations of the source, ranging from $y = 8.0$ to $y = 0.0$. For each case, the left panel shows the source and the caustic circle ($y_r = 5.640$) on the source plane, and the right panel shows the image(s), the radial critical circle ($x_r = 3.334$), and the tangential critical circle ($x_t = 9.783$) on the image plane. At $y = 8.0$, only one image appears. At $y = 5.4$, the source overlaps the caustic, and a second, radially-oriented image appears on the radial critical circle. At $y = 4.8$, the source is entirely inside the caustic, and the second image splits in two images, located on opposite sides of the radial critical circle, forming with the original image a system of 3 aligned images. As the source moves toward $y = 0$, the central image moves toward $x = 0$ and becomes significantly fainter, while the other images move toward the tangential critical circle and become bright, elongated arcs. At $y = 0$, the two arcs have merged to form an Einstein ring located on top of the tangential critical circle, while the central image, very faint, is

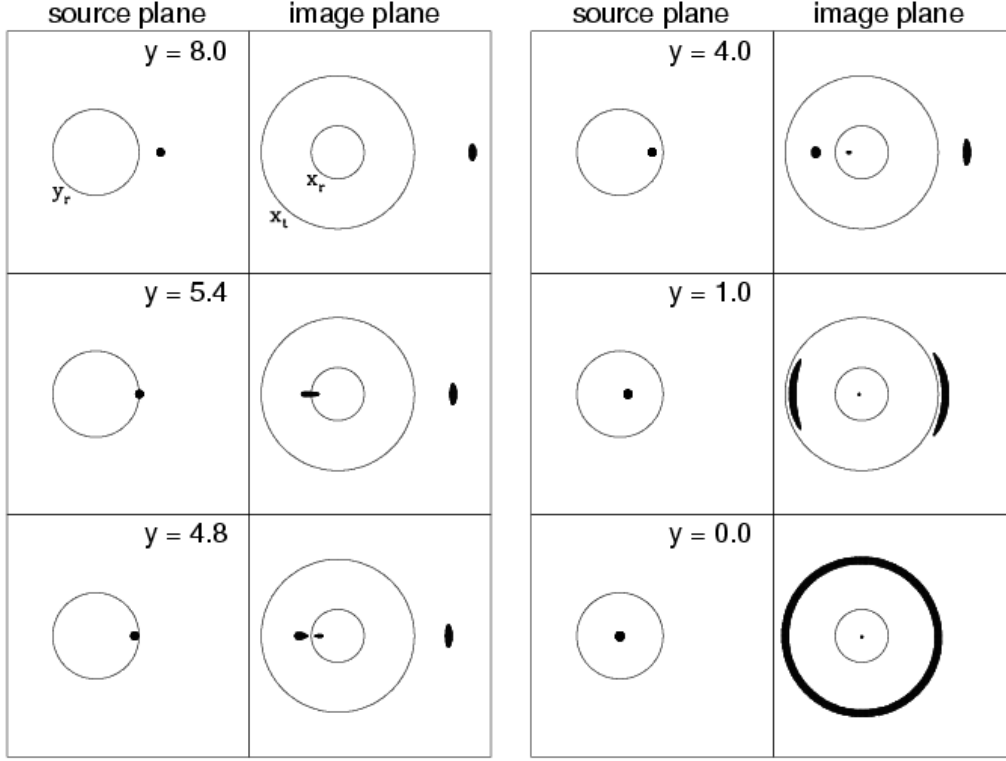


Figure 40: Images of a circular source. Each pair of panels shows the source plane in the left panel, with the caustic, and the image plane in the right panel, with the radial (inner) and tangential (outer) critical circles. The position y of the source on the source plane is indicated. We used $\kappa_c = 4.015$, and a source of diameter $\Delta y = 1$.

still visible in the center.

5.5 IMAGE SEPARATION AND MAGNIFICATION

The locations of the images are computed by solving the lens equation (97). For the TIS, this equation must be solved numerically. In Fig. 41, we plot the separation between the two outer images as a function of the source location. The plot only extends to $y/y_r = 1$, since larger values of y only produce one image. The solid and dotted curves show the separations for the TIS and NFW profile, respectively, with various values of κ_c and $\kappa_s \equiv \rho_{\text{NFW}} r_{\text{NFW}} / \Sigma_{\text{crit}}$. The separation is fairly insensitive to the source location, and stays within $\sim 15\%$ of the Einstein ring diameter $\Delta x = 2x_t$ for all values of κ_c and κ_s considered. The dashed line in Fig. 41 shows the separation for the SIS, which is independent of y . For all profiles considered, the

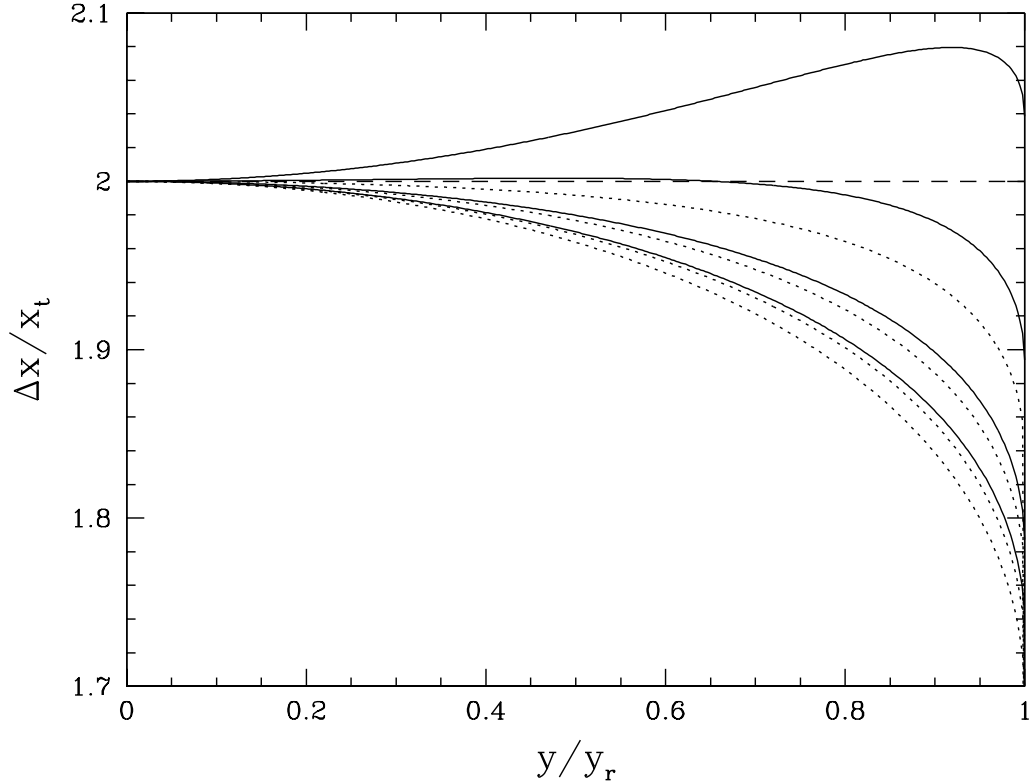


Figure 41: Separation Δx between the two outer images, in units of the tangential critical radius x_t , versus source location y in units of the caustic radius y_r . The solid curves, from top to bottom, corresponds to TIS with $\kappa_c = 10, 5, 2.5,$ and $1.2,$ respectively. The dotted curves, from top to bottom, corresponds to NFW profiles with $\kappa_s = 1.0, 1.0, 0.5,$ and $0.2,$ respectively. The dashed line corresponds to the SIS. Results for the Schwarzschild lens are not plotted.

image separation is always of order the Einstein ring diameter, independently of the source location. This is particularly convenient for theoretical studies, when the actual source location can be ignored [93].

The magnification of an image located at position x on the lens plane is given by

$$\mu = \left(1 - \frac{m}{x^2}\right)^{-1} \left[1 - \frac{d}{dx} \left(\frac{m}{x}\right)\right]^{-1} = \left(1 - \frac{\alpha}{x}\right)^{-1} \left(1 - \frac{d\alpha}{dx}\right)^{-1} \quad (105)$$

([124], eq. [8.17]). We computed the magnification of the images produced by halos of masses $10^{13}, 10^{14}, 3 \times 10^{14},$ and $10^{15} M_\odot$. Fig. 42 shows the total magnification. The dotted curves show the results for a NFW profile. As y (or η) decreases, the magnification slowly increases, until the source reaches the radial caustic $y = y_r$. At that moment, a second image, with infinite magnification appears on the radial

critical curve (for clarity, we truncated those infinite “spikes” in Fig. 42). As y keeps decreasing, that second image splits into two images, and the total magnification becomes finite again, until the source reaches $y = 0$, and an Einstein ring with infinite magnification appears on the tangential critical curve. Of course, these infinite magnifications are not physical, since they can only occur for point sources. The total magnification is always larger than unity, and always larger when 3 images are present.

The solid curves in Fig. 42 shows the results for the TIS. At low masses, there is no radial caustic (See Fig. 38), and only one image appears. Because of the presence of a flat density core, the magnification is nearly constant if the path of the rays goes near the center of the core. For instance, for the case $M_{200} = 10^{13} M_{\odot}$ (top left panel of Fig. 42), $r_0 > 10$ kpc, hence, over the range of η being plotted, we are way inside the core. As the mass increases, the magnification increases, until a radial caustic forms. This happens at $M_{200} = 1.11 \times 10^{15} M_{\odot}$ for $z_{\text{coll}} = 0.5$, $M_{200} = 3.5 \times 10^{14} M_{\odot}$ for $z_{\text{coll}} = 1.0$, and $M_{200} = 1.2 \times 10^{14} M_{\odot}$ for $z_{\text{coll}} = 1.5$ according to Fig. 38. At this point, the TIS has the ability to form three images, and the results become qualitatively similar to the ones for the NFW profile.

The short-dashed and long-dashed curves in Fig. 42 shows the results for the SIS and the Schwarzschild lens, respectively. Because of the absence of radial caustic, the magnification always varies smoothly with source position, and the only divergence occurs at $\eta = 0$, where an Einstein ring forms.

For a given mass, the Schwarzschild lens always produces a stronger magnification than a SIS or NFW profile, unless the source is very close to the radial caustic of the NFW profile, where a “spike” of infinite magnification forms. The magnifications produced by the SIS and NFW profile tend to be similar. If the NFW profile produces only one image (that is, we are on the right hand side of the dotted spike in Fig. 42), the SIS produces a larger magnification than the NFW profile. But if the NFW profile produces 3 images, then the total magnification exceeds the one produced by the SIS. As for the TIS, at low masses, where only one image forms, the magnification is much smaller than for the other profiles. But at large masses, where multiple images can form, the magnification becomes comparable to the one for the other profiles, and can even exceed the magnification produced by the Schwarzschild lens.

5.6 WEAK LENSING

Weak lensing usually refers to the magnification and distortion of the image of a background source by a foreground lens. Unlike strong lensing, weak lensing normally does not produce multiple images of single sources. The detection of coherent distortion patterns in the sky has been used to constrain the mass of clusters. The first detections were reported by [19, 35, 47, 132, 147], followed by many others (see [13] and references therein). More recently, the distortion pattern produced by individual galaxies has also been detected [20, 39, 42, 50, 60, 66, 105].

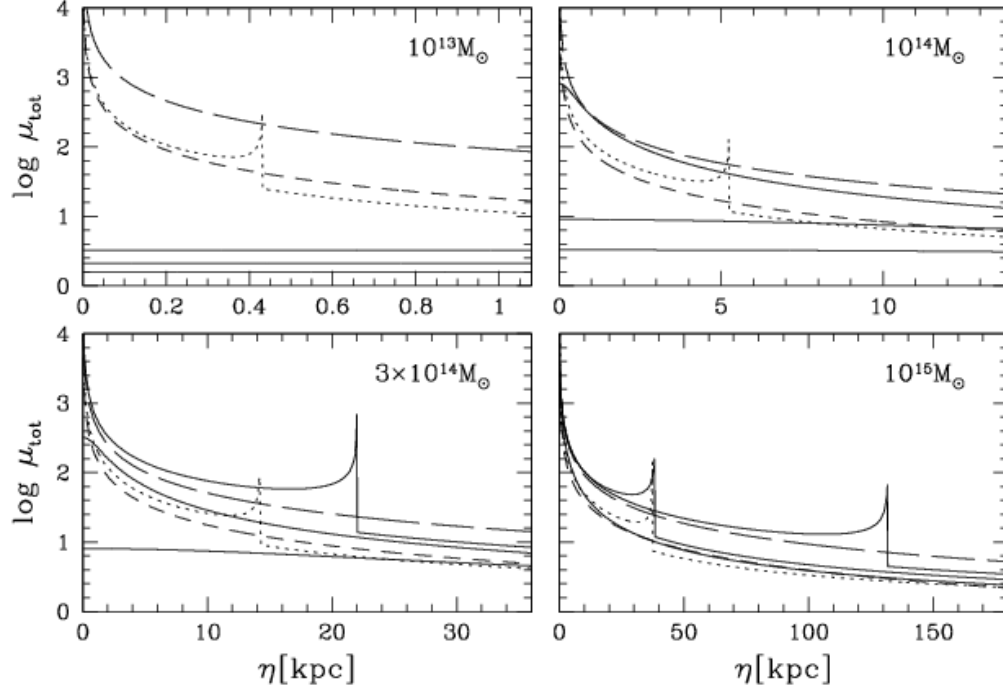


Figure 42: Total magnification μ_{tot} versus source location η for lenses of masses $10^{13} - 10^{15} M_{\odot}$, for the TIS (solid curves), the NFW profile (dotted curves), the SIS (short dashed curves) and the Schwarzschild lens (long dashed curves). For the TIS, the curves, from top to bottom, correspond to $z_{\text{coll}} = 1.5, 1.0,$ and $0.5,$ respectively.

Following the approach of [152], we use as measure of the distortion produced by a lens the average shear $\bar{\gamma}$ inside a distance $\xi = r_{200}$ from the lens center. In practice, this quantity would be evaluated by averaging the shear of all images observed inside r_{200} , after having eliminated foreground sources. We estimate this quantity by integrating the shear over the projected area of the cluster. The average shear inside radius x is given by

$$\bar{\gamma}(x) = \frac{2}{x^2} \int_0^x x' \gamma(x') dx' = \frac{2}{x^2} \int_0^x x' \left[\frac{m(x')}{x'^2} - \kappa(x') \right] dx', \quad (106)$$

where $\kappa(x') = \Sigma(x')/\Sigma_{\text{crit}}$ is the convergence. After some algebra, we get

$$\bar{\gamma}_{\text{TIS}}(x) = \frac{2ab\kappa_c}{(Ab - Ba)x^2} \left\{ Aa \left[\left(1 + \frac{x^2}{a^2} \right)^{1/2} - 1 - 2 \ln \frac{1 + (1 + x^2/a^2)^{1/2}}{2} \right] \right\}$$

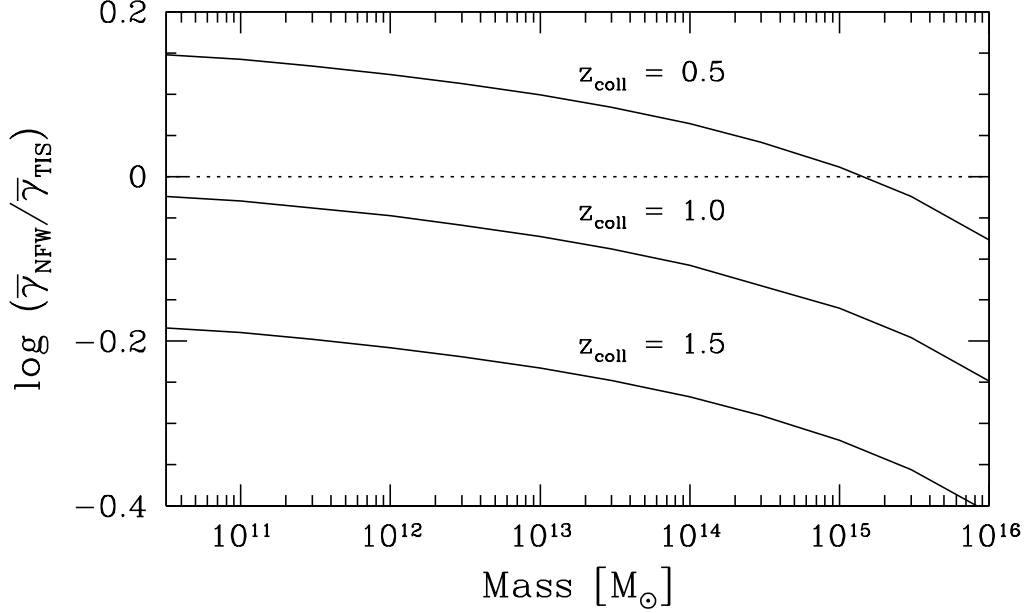


Figure 43: Ratio of the average shear inside radius r_{200} for the NFW profile and the TIS profile, versus mass of the halo. The values of z_{coll} for the TIS are indicated.

$$- Bb \left[\left(1 + \frac{x^2}{b^2} \right)^{1/2} - 1 - 2 \ln \frac{1 + (1 + x^2/b^2)^{1/2}}{2} \right] \quad (107)$$

We evaluate this expression at $r = r_{200}$, or equivalently $x = r_{200}/r_0 \equiv \eta_{200} = 24.2$. It reduces to

$$\bar{\gamma}_{\text{TIS}}(r_{200}) = 408.67 \frac{\rho_c r_{200}}{\Sigma_{\text{crit}}}, \quad (108)$$

where we used equation (87) to eliminate ρ_0 .

In Fig. 43 we plot the ratio $\bar{\gamma}_{\text{NFW}}/\bar{\gamma}_{\text{TIS}}$ versus mass. The ratios are larger at lower collapse redshifts z_{coll} , and also decrease with increasing mass. This reflects the fact that as the mass increases, the concentration parameter c of the NFW profile decreases, while the ratio r_{200}/r_0 for the TIS remains fixed at 24.2. This figure can be *qualitatively* compared with the top left panel of Fig. 3 in [152]. We reach essentially the same conclusion as these authors, namely that using the average shear to estimate the mass of lensing halos can lead to considerable errors if the wrong density profile is assumed. For $z_{\text{coll}} = 0.5$, we find $\bar{\gamma}_{\text{NFW}}/\bar{\gamma}_{\text{TIS}} > 1$ at small mass, and therefore the mass of a TIS would be underestimated if the lens is incorrectly assumed to follow a NFW profile. At high mass, the true mass of a TIS would be overestimated. For $z_{\text{coll}} = 1.0$ and 1.5 , $\bar{\gamma}_{\text{NFW}}/\bar{\gamma}_{\text{TIS}} < 1$ at all masses

considered, down to $3 \times 10^{10} M_{\odot}$, and therefore the true mass of a TIS would always be overestimated.

5.7 DISCUSSION

In the previous two sections, we derived the effects of strong and weak lensing, respectively. Here, “strong lensing” refers to case with multiple images, arcs, or rings, while “weak lensing” refers to the magnification and shear of single images. We can divide the observed cases of strong lensing in two groups. The first group contains the “arc second” cases: multiple-image systems with image separations of order arc seconds, or rings with radii of that order [84].⁷ In most cases, the lens is a single, massive galaxy, with possibly some additional contribution from the environment in which this galaxy is located ([145]; see, however, [113]). A classic example is Q0957+561, the first gravitational lens to be discovered. The second group contains the “arc minute” cases, in which the lens is an entire cluster of galaxies. These lenses produce mostly giant arcs, with radii in the range $15'' - 60''$ (see Table 1 of [151]). The most famous case is the cluster CL 0024+1654, which produces multiple arcs.

We showed that for all profiles considered, the image separation is weakly dependent on the source location (Fig. 41), when multiple images actually form. If we neglect this dependence, the image separation $\Delta\theta \approx 2\theta_t$ can be read off the top panels of Fig. 38. We see immediately that galaxy-size objects cannot produce arc-second separations if they are described by the TIS or the NFW profile (under the assumption described in §2 that c for NFW halos is the typical value for halos at $z_{\text{obs}} = z_L$). The TIS does not produce multiple images unless the mass is of order $10^{14} M_{\odot}$ or above. The NFW profile can produce multiple images for any mass, but a separation $\Delta\theta > 1''$ requires a mass of order $10^{13} M_{\odot}$. Even the SIS needs a mass in excess of $10^{12} M_{\odot}$ to produce arc-second separations. At the cluster scale, all profiles are capable of producing arc-minute separations. In this limit, for a given mass, the separation is larger for the Schwarzschild lens and smaller for the NFW profile (because of the small concentration parameter at large mass). The separations are comparable for the SIS and TIS for $z_{\text{coll}} = z_L$, but for $z_{\text{coll}} > z_L$ the separation tends to be larger for the TIS than the SIS. As we indicated in the introduction, the TIS and NFW profile are applicable to dwarf galaxies and clusters of galaxies, but might not be applicable to ordinary galaxy-scale objects because baryonic processes are neglected. Hence, the inability of the TIS and NFW profiles to produce arc seconds separations with galaxy-size lenses is not a concern.

Let us now focus on the TIS, and perform a simple calculation to estimate the probability that a TIS can produce multiple images. To compute κ_c , we substitute equations (82), (87), and (88) in equation (101). For the particular cosmological model (Λ CDM) and redshifts ($z_S = 3$, $z_L = 0.5$) we have considered in this paper,

⁷See <http://cfa-www.harvard.edu/castles>.

we get

$$\kappa_c = 480.75 \frac{\rho_c^{2/3}(z_L)}{\Sigma_{\text{crit}}(z_L)} \left[\frac{\rho_c(z_{\text{coll}})}{\rho_c(z_L)} \right]^{2/3} M_{200}^{1/3} = 0.968 \left[\frac{\rho_c(z_{\text{coll}})}{\rho_c(z_L)} \right]^{2/3} M_{15}^{1/3}, \quad (109)$$

where $M_{15} \equiv M_{200}/10^{15} M_\odot$. Strong lensing requires $\kappa_c \geq 1$. Setting $\kappa_c = 1$, $z_{\text{coll}} = z_L$, and solving for M_{200} , we get $M_{200} = 1.102 \times 10^{15} M_\odot$. The requirement for strong lensing then becomes

$$M_{15} \geq M_{15,\text{min}}, \quad (110)$$

where

$$M_{15,\text{min}} \leq 1.102. \quad (111)$$

Hence, in the worst case scenario, a halo that formed at the latest possible collapse redshift $z_{\text{coll}} = z_L$, the required mass is about $10^{15} M_\odot$. That value drops quite rapidly with increasing z_{coll} , down to about $1.2 \times 10^{14} M_\odot$ for $z_{\text{coll}} = 1.5$ (see Fig. 38). For the cosmological model we consider, 1- σ density fluctuations collapsing at redshift $z_{\text{coll}} = (0.5, 1.0, 1.5)$ have masses of about $M_{15} = (2 \times 10^{-3}, 4 \times 10^{-4}, 9 \times 10^{-5})$. Such ‘‘typical’’ objects will not be capable of producing multiple images of a source at redshift $z_S = 3$, since the resulting values $\kappa_c = (0.122, 0.127, 0.120)$ are smaller than unity. This simply indicates that multiple images are not produced by typical objects, which is certainly consistent with the fact that fewer than 30 arc-minutes, multiple-image systems have been observed. It is remarkable that the value of κ_c for typical objects is nearly independent of z_{coll} . It just happens the the dependences of $\rho_c(z_{\text{coll}})$ and M_{15} in equation (109) nearly cancel out when M_{15} is set to the typical value at that redshift.

Increasing κ_c above unity would require an object about 500 times more massive than a typical object at the same redshift. Objects of this mass are rare but do exist. We can make a simple estimate of how atypical such a massive object is. Over most of the mass range of cosmological interest (from small galaxies to clusters of galaxies) the CDM power spectrum can be roughly approximated by a power law $P(k) \propto k^n$, where k is the wavenumber and $n \approx -2$. The rms density fluctuation δ_{rms} is then given by $\delta_{\text{rms}} \approx k^{3/2} P^{1/2}(k) \propto k^{1/2}$. At a given redshift, different values of the wavenumber k correspond to different mass scales M according to $M \propto k^{-3}$. The relation between rms density fluctuation and mass scale at fixed epoch is therefore approximated by

$$\delta_{\text{rms}} \propto M^{-1/6}. \quad (112)$$

Increasing the mass by a factor of 500 therefore reduces δ_{rms} by a factor of $500^{1/6} \approx 2.8$. Because of the reduction in δ_{rms} , a 1- σ fluctuation ($\delta = \delta_{\text{rms}}$) at this higher mass will no longer collapse by the same redshift (it will collapse later), but a 2.8- σ fluctuation ($\delta = 2.8\delta_{\text{rms}}$) will. Such fluctuations are rare, but not vanishingly rare. In Gaussian statistics, the probability that a randomly located point in space is

inside a $2.8\text{-}\sigma$ density fluctuation (i.e. $\delta \geq 2.8\delta_{\text{rms}}$) is about 1/200. Hence, one of every 200 halos would be capable of producing multiple images (of course, whether any halo actually produces multiple images depends on the location of the sources).

To give a specific example of a cluster-mass lens with $z_{\text{coll}} > z_L$, consider the case of the cluster CL 0025+1654. [126] showed that the mass-model derived by [146] to explain their lensing data for CL 0024+1654 at $z = 0.39$ is very well-fitted by a TIS halo with $\rho_0 \approx 0.064h^2 M_\odot \text{pc}^{-3}$ and $r_0 \approx 20h^{-1} \text{kpc}$. This central density implies that the halo collapse redshift is $z_{\text{coll}} \approx 2.5$ (i.e. $z_{\text{coll}} \gg z_L$). The halo mass is then $M_{200} = 661.6\rho_0 r_0^3 = 4.84 \times 10^{14} M_\odot$ (for $h = 0.7$), and equation (109) gives $\kappa_c = 4.8 \gg 1$. It is therefore not surprising that this cluster produces strong lensing.

5.8 SUMMARY

We have derived the lensing properties of cosmological halos described by the TIS model. The solutions depend on the background cosmological model through the critical surface density Σ_{crit} , which is a function of the cosmological parameters and the source and lens redshifts, and the TIS parameters ρ_0 and r_0 , which are functions of the mass and collapse redshift of the halo, and the cosmological parameters. By expressing the surface density of the halo in units of Σ_{crit} and the distances in units of r_0 , all explicit dependences on the cosmological model disappear, and the solutions are entirely expressible in terms of two dimensionless parameters, the central convergence κ_c and the scaled position y of the source. We have computed solutions for the critical curves and caustics, the image separations, and the total magnification. The ability of the TIS to produce strong lensing (multiple images and rings) depends entirely on κ_c . If $\kappa_c < 1$, only one image can form. If $\kappa_c > 1$, either one or three images can form, depending on whether the source is located outside or inside the radial caustic. When three images are produced, the central one is usually very faint, being highly demagnified. The angular separation between the two outermost images depends strongly on κ_c , but only weakly on the source location.

For comparison, we derived (or extracted from the literature) the lensing properties of three comparison models: the NFW profile, the singular isothermal sphere, and the Schwarzschild lens. Unlike the TIS, all of these profiles have a central singularity, which allows them to produce multiple images at any mass, provided that the source is sufficiently aligned with the lens. In practice, image separations large enough to be resolved can be achieved by galactic-mass objects only for the Schwarzschild lens, and by supergalactic-mass objects for all profiles.

We applied the TIS model to the currently-favored Λ CDM universe, to calculate the central convergence κ_c expected for TIS halos of different masses and collapse epochs. We found that high-redshift sources (e.g. $z_S \approx 3$) will be strongly lensed by TIS halos (i.e. $\kappa_c > 1$) only for cluster-mass halos, assuming that these halos formed at the redshift they are observed. As equation (109) shows, the halo mass required for strong lensing can be decreased by increasing the formation redshift

of the halo. However, as the formation redshift increases, the typical halo mass decreases, leading to a near-cancellation of the effect: the value of κ_c for a typical halo is about 0.12, independent of the collapse redshift. From this, we showed that a halo described by a TIS must form out of a $\sim 2.8 - \sigma$ fluctuation to be capable of producing strong lensing ($\kappa_c > 1$), no matter when the halo formed. Notice that weak lensing (magnification and shear of single images) does not require $\kappa_c > 1$, and can be caused by halos of any mass.

This work was supported by the Research and Training Network "The Physics of the Intergalactic Medium" set up by the European Community RTN under the contract HPRN-CT2000-00126 RG29185, NASA grants NAG5-10825, NAG5-10826, NNG04G177G and Texas Advanced Research Program grant 3658-0624-1999. MAA is grateful for the support of a DOE Computational Science Graduate Fellowship.

References

- [1] Abadi, M. G., Bower, R. G. & Navarro, J. F. 2000, MNRAS, 314, 759
- [2] Ahn, K. & Shapiro, P. R. 2003, JKAS, 36, 89
- [3] Ahn, K. & Shapiro, P. R. 2004, in preparation
- [4] Alvarez, M. A., Ahn, K., & Shapiro, P. R. 2003, RevMexAA SC, 18, 4
- [5] Alvarez, M. A., Shapiro, P. R., & Martel, H. 2000, RevMexAA SC, 10, 214
- [6] Alvarez, M. A., Shapiro, P. R., & Martel, H. 2001, AIP Conf.Proc., 586, 938
- [7] Alvarez, M. A., Shapiro, P. R., & Martel, H. 2003, RevMexAA SC, 17, 39
- [8] Avila-Reese, V., Colin, P., Valenzuela, O., D'Onghia, E., Firmani, C. 2001, ApJ, 559, 516
- [9] Avila-Rees, V., Firmani, C. & Hernández, X. 1998, ApJ, 505, 37
- [10] Balberg, S., Shapiro, S. L. & Inagaki, S. 2002, ApJ, 568, 475
- [11] Bardeen, J. M., Bond, J. R., Kaiser, N. & Szalay, A. S. 1986, ApJ, 304, 15
- [12] Barnes, J., & Efstathiou, G. 1987, ApJ, 319, 575
- [13] Bartelmann, M., & Schneider, P. 2001, Phys.Rep., 340, 291
- [14] Bertschinger, E. 1985, ApJ, 58, 39
- [15] Bertschinger, E. 1989, ApJ, 340, 666

- [16] Binney, J., & Tremaine, S.: *Galactic Dynamics* (Princeton University Press, Princeton 1987)
- [17] Blandford, R. D., Saust, A. B., Brainerd, T. G., & Villumsen, J. V. 1991, MNRAS, 251, 600
- [18] Bode, P., Ostriker, J.P., Turok, N. 2001, ApJ, 556, 93
- [19] Bonnet, H., Mellier, Y., & Fort, B. 1994, ApJ, 427, L83
- [20] Brainerd, T. G., Blandford, R. D., & Smail, I. 1996, ApJ, 466, 623
- [21] Bryan, G.L. & Norman, M.L. 1998, ApJ, 495, 80
- [22] Bullock, J.S., Kolatt, T.S., Sigad, Y., Somerville, R.S., Kravtsov, A.V., Klypin, A.A., Primack, J.R., Dekel, A., 2001, MNRAS, 321, 559
- [23] Bullock, J. S., Dekel, A., Kolatt, T. S., Kravtsov, A. V., Klypin, A. A., Porciani, C., & Primack, J. R. 2001, ApJ, 555, 240
- [24] Burkert, A. 1995, ApJ, 447, L25
- [25] Burkert, A. 2000, ApJ, 534, L143
- [26] Burkert, A. & Silk, J. 1999, in Dark Matter in Astrophysics and Particle Physics, Proceedings of the second International Conference on Dark Matter in Astrophysics and Particle Physics, eds. H. V. Klapdor-Kleingrothaus and L. Baudis (Philadelphia: Institute of Physics Publishers), p. 375
- [27] Carlberg, R. G., Yee, H. K. C., Ellingson, E., Morris, S. L., Abraham, R., Gravel, P., Pritchet, C. J., Smecker-Hane, T., Hartwick, F. D. A., Hesser, J. E., Hutchings, J. B. & Oke, J. B. 1997, ApJ, 485, L13
- [28] Chiba, T. & Takahashi, R. 2001, unpublished (astro-ph/0106273 v1)
- [29] Chiba, T. & Takahashi, R. 2002, Prog.Theor.Phys., 107, L625
- [30] Cole, S. & Lacey, C. 1996, MNRAS, 281, 716
- [31] Colin, P., Klypin, A. A., & Kravtsov, A. V. 2000, ApJ, 539, 561
- [32] Colin, P., Avila-Reese, V., Valenzuela, O. 2000, ApJ, 542, 622
- [33] Colin, P., Klypin, A., Valenzuela, O., & Gottlöber, S. 2003, astro-ph/0308348
- [34] Czoske, O., Moore, B., Kneib, J.-P., Soucail, G. 2002, A&A, 386, 31
- [35] Dahle, H., Maddox, S. J., & Lilje, P. B. 1994, ApJ, 435, L79

- [36] Davé, R., Spergel, D. N., Steinhardt, P. J. & Wandelt, B. D. 2001, *ApJ*, 547, 574
- [37] de Blok, W.J.G., McGaugh, S.S., Bosma, A., & Rubini, V.C. 2001, *ApJ*, 552, L23
- [38] de Blok, W.J.G., & Bosma, A. 2002, *A&A*, 385, 816
- [39] Dell'Antonio, I., & Tyson, J. A. 1996, *ApJ*, 473, L17
- [40] Del Popolo, A., Gembera, M., Recami, E. & Spedicato, E. 2000, *A&A*, 353, 427
- [41] Dressler, A., & Smail, I., Poggianti, B.M., Butcher, H., Couch, W.J., Ellis, R.S., Oemler, A., Jr. 1999, *APJS*, 122, 51
- [42] Ebbels, T. 1998, Ph.D. thesis, Cambridge Univ.
- [43] Eke, V.R., Navarro, J.F., Frenk, C.S. 1998, *ApJ*, 503, 569
- [44] Eke, V. R., Navarro, J. F., & Steinmetz, M. 2001, *ApJ*, 554, 114
- [45] Evrard, A.E. et al. 2002, *ApJ*, 573, 7
- [46] Evrard, A.E., Metzler, C.A., & Navarro, J.F. 1996, *ApJ*, 469, 494
- [47] Fahlman, G., Kaiser, N., Squires, G., & Woods, D. 1994, *ApJ*, 437, 56
- [48] Fillmore, J.A., Goldreich, P. 1984, *ApJ*, 281, 1
- [49] Firmani, C., D'Onghia, E., Chincarini, G., Hernandes, X., & Avila-Reese, V. 2000, *MNRAS*, 321, 713
- [50] Fischer, P. et al. 2000, *AJ*, 120, 1198
- [51] Flores, R.A., & Primack, J.R. 1994, *ApJ*, 427, L1
- [52] Frenk, C. S. et al. 1999, *ApJ*, 525, 554
- [53] Fukushige, T., & Makino, J. 1997, *ApJ*, 477, L9
- [54] Fukushige, T., & Makino, J. 2001, *ApJ*, 557, 533
- [55] Fukushige, T., & Makino, J. 2003, *ApJ*, 588, 674
- [56] Fukushige, T., Kawai, A., & Makino, J. 2004, *ApJ*, 606, 625
- [57] Gavazzi, R., Fort, B., Mellier, Y., Pelloz, R., & Dantel-Fort, M. 2003, *A&A*, 403, 11

- [58] Ghigna, S., Moore, B., Governato, F., Lake, G., Quinn, T., & Stadel, J. 2000, *ApJ*, 544, 616
- [59] Girardi, M., Giuricin, G., Mardirossian, F., Mezzetti, M., Boschin, W. 1998, *ApJ*, 505, 74
- [60] Griffiths, R. E., Casertano, S., Im, M., & Ratnatunga, K. U. 1996, *MNRAS*, 282, 1159
- [61] Gunn, J. E. & Gott, J. R. 1972, *ApJ*, 176, 1
- [62] Hinshaw, G., & Krauss, L. M. 1987, *ApJ*, 320, 468
- [63] Hiotelis N. 2002, *A&A*, 382, 84
- [64] Hoffman, Y. & Shaham, J. 1985, *ApJ*, 297, 16
- [65] Hozumi, S., Burkert, A. & Fujiwara, T. 2000, *MNRAS*, 311, 377
- [66] Hudson, M. J., Gwyn, S. D. J., Dahle, H., & Kaiser, N. 1998, *ApJ*, 503, 531
- [67] Huss, A., Jain, B., & Steinmetz, M. 1999, *MNRAS*, 308, 1011
- [68] Iliev, I. T. 2000, PhD Thesis (University of Texas at Austin)
- [69] Iliev, I. T., Scannapieco, E., Martel, H., & Shapiro, P. R. 2003, *MNRAS*, 341, 81
- [70] Iliev, I.T. & Shapiro, P.R. 2001a, *ApJ*, 546, L5
- [71] Iliev, I.T., & Shapiro, P.R. 2001b, *MNRAS*, 325, 468 (Paper II)
- [72] Jaroszyński, M. 1991, *MNRAS*, 249, 430
- [73] Jaroszyński, M. 1992, *MNRAS*, 255, 655
- [74] Jing, Y., & Suto, Y. 2000, *ApJ*, 526, L69
- [75] Jing, Y., & Suto, Y. 2002, *ApJ*, 574, 538
- [76] Jones, C. & Forman, W. 1999, *ApJ*, 511, 65
- [77] Jang-Condell, H., & Hernquist 2001, *ApJ*, 548, 68
- [78] Kaplinghat, M., Knox, L., & Turner, M.S. 2000, *Phys.Rev.Lett.*, 85, 3335
- [79] Keeton, C. R., & Madau, P. 2001, *ApJ*, 549, L29
- [80] Klypin, A. A., Kravtsov, A. V., Valenzuela, O., & Prada, F. 1999, *ApJ*, 522, 82

- [81] Klypin, A., Kravtsov, A. V., Bullock, J. S., & Primack, J. R. 2001, *ApJ*, 554, 903
- [82] Knebe, A., Devriendt, J.E.G., Mahmood, A., Silk J. 2002, *MNRAS*, 329, 813
- [83] Kochanek, C. S. 1995, *ApJ*, 453, 545
- [84] Kochanek, C. S., Falco, E. E., Impey, C., Lahár, J., McLeod, B., & Rix, H.-W. 1998, CASTLE Survey Gravitational Lens Data Base (Cambridge:CfA)
- [85] Kochanek, C. S. & White, M. 2001, *ApJ*, 559, 531
- [86] Kormendy, J. & Freeman, K. C.: 'Scaling laws for dark matter halos in late-type and dwarf spheroidal galaxies'. In *Ringberg Proceedings 1996 Workshop*, eds. R. Bender, T. Buchert, P. Schneider, & F. von Feilitzsch (MPI, Munich 1996), pp. 13 - 15
- [87] Kormendy, J. & Freeman K.C. 2004, in preparation
- [88] Kravtsov, A.V., Klypin, A.A., Bullock, J.S., & Primack, J.R. 1998 *ApJ*, 502, 48
- [89] Kull, A. 1999, *ApJ*, 516, L5
- [90] Li, L.-X., & Ostriker, J. P. 2002, *ApJ*, 566, 652
- [91] Lokas, E.L., Hoffman, Y. 2000, *ApJ*, 542, L139
- [92] Lokas, E.L., Mamon, G.A. 2001, *MNRAS*, 321, 155
- [93] Martel, H., Premadi, P., & Matzner, R. 2002, *ApJ*, 570, 17
- [94] Martel, H., Shapiro, P.R. 2001, *RevMexSC*, 10, 101
- [95] Mateo, M., Olszewski, E.W., Vogt, S.S., & Keane, M.J. 1998, *ApJ*, 116, 2315
- [96] Mathiesen, B.F., & Evrard A.E. 2001, *ApJ*, 546, 100
- [97] Mohr, J.J., Mathiesen, B.F., & Evrard A.E. 1999, *ApJ*, 517, 627
- [98] Moore, B. 1994, *Nature*, 370, 629
- [99] Moore, B., 2001, in AIP Conf. Series 586, Relativistic Astrophysics, Proceedings of the 20th Texas Symposium, eds. J. C. Wheeler & H. Martel, p. 73
- [100] Moore, B., Governato, F., Quinn, T., Stadel, J., & Lake, G. 1998, *ApJ*, 499, L5
- [101] Moore, B., Ghigna, S., Governato, F., Lake, G., Quinn, T., Stadel, J., & Tozzi, P. 1999, *ApJ*, 524, L19

- [102] Moore, B., Quinn, T., Governato, F., Stadel, J., & Lake, G. 1999, *MNRAS*, 310, 1147
- [103] Mori M. & Burkert A. 2000, 538, 559
- [104] Narayan, R., & White, S. D. M. 1988, *MNRAS*, 231, 97
- [105] Natarajan, P., Kneib, J.-P., Smail, I., & Ellis, R. S. 1998, *ApJ*, 499, 600
- [106] Natarajan, P., & Lynden-Bell, D. 1997, *MNRAS*, 286, 268
- [107] Navarro, J.F, Frenk, C. S., White, S. D. M. 1996, *ApJ*, 462, 563
- [108] Navarro, J. F., Frenk, C. S., & White, S. D. M. 1997, *ApJ*, 490, 493
- [109] Navarro, J. F., Hayashi, E., Power, C., Jenkins, A. R., Frenk, C. S., White, S. D. M., Springel, V., Stadel, J., & Quinn, T. R. 2004, *MNRAS*, 349, 1039
- [110] Owen, J. J., Weinberg, D. H. & Villumsen, J. V. 1998, astro-ph/9805097
- [111] Owen, J.M., Villumsen, J.V., Shapiro, P.R., Martel, H., 1998, *ApJS*, 116, 155
- [112] Power, C., Navarro, J. F., Jenkins, A., Frenk, C. S., White, S. D. M., Springel, V., Stadel, J., & Quinn, T. 2003, *MNRAS*, 338, 14
- [113] Premadi, P., & Martel, H. 2004, *ApJ*, in press
- [114] Premadi, P., Martel, H., & Matzner, R. 1998, *ApJ*, 493, 10
- [115] Premadi, P., Martel, H., Matzner, R., & Futamase, T. 2001a, *ApJ Suppl.*, 135, 7
- [116] Premadi, P., Martel, H., Matzner, R., & Futamase, T. 2001b, *P.A.S.Aus.*, 18, 201
- [117] Press, W.H., & Schechter, P. 1974, *ApJ*, 187, 425
- [118] Primack, J. R., Bullock, J. S., Klypin, A. A., & Kravtsov, A. V. 1999, in *ASP Conf. Ser. 182, Galaxy Dynamics*, ed. D. R. Merritt, M. Valluri, and J. A. Sellwood (San Francisco: ASP)
- [119] Ricotti, M. 2003, *MNRAS*, 344, 1237
- [120] Richstone, D.O. & Tremaine, S. 1984, *ApJ*, 286, 27
- [121] Rusin, D., & Ma, C.-P. 2001, *ApJ*, 549, L33
- [122] Ryden, B. S. & Gunn, J. E. 1987, *ApJ*, 318, 15
- [123] Sand, D.J., Treu, T., Smith, G.P., & Ellis, R.S. 2004, *ApJ*, 604, 88

- [124] Schneider, P., Ehlers, J., & Falco, E. E. 1992, *Gravitational Lenses* (New York: Springer)
- [125] Shapiro P.R.: ‘Cosmological Reionization’. In: *Proceedings of the 20th Texas Symposium on Relativistic Astrophysics and Cosmology*, eds. H. Martel and J. C. Wheeler, (AIP Conference Series, v.586, 2001), pp. 219-232
- [126] Shapiro, P.R., & Iliev, I.T. 2000, *ApJ*, 542, L1
- [127] Shapiro, P.R., & Iliev, I.T. 2002, *ApJ*, 565, L1
- [128] Shapiro, P.R., Iliev, I.T., & Raga, A.C. 1999, *MNRAS*, 307, 203 (Paper I)
- [129] Shapiro, P.R., Martel, H., Villumsen, J.V., Owen, J.M., 1996, *ApJS*, 103, 269
- [130] Shapiro, P.R. & Struck-Marcell 1985, *ApJS*, 57, 205
- [131] Simon, J.D., Bolatto, A.D., Leroy, A., & Blitz, L. 2003, *ApJ*, 596, 957
- [132] Smail, I., Ellis, R. S., Fitchett, M. J., & Edge, D. 1995, *MNRAS*, 273, 277
- [133] Soucail, G. 2001, in *AIP Conf. Series 586, Relativistic Astrophysics, Proceedings of the 20th Texas Symposium*, eds. J. C. Wheeler & H. Martel, p. 233
- [134] Spergel, D. N. et al. 2003, *ApJS*, 148, 175
- [135] Spergel, D. N. & Steinhardt, P. J. 2000, *PRL*, 84, 3760
- [136] Springel, V., Yoshida, N., White, S.D.M. 2001, *NewA*, 6, 79
- [137] Subramanian, K., Cen, R. & Ostriker, J. P. 2000, *ApJ*, 538, 528
- [138] Swaters, R.A., Madore, B.F., van den Bosch, F.C., & Balcells, M. 2003, *ApJ*, 583, 732
- [139] Swaters, R.A., Verheijen, M.A.W., Bershady, M.A., & Anderson, D.R. 2003, *ApJ*, 587, L19
- [140] Takahashi, R., & Chiba, T. 2001, *ApJ*, 563, 489
- [141] Tasitsiomi, A., Kravtsov, A. V., Gottlöber, S., & Klypin, A. A. 2004, *ApJ*, 607, 125
- [142] Teyssier, R., Chieze, J.-P. & Alimi, J.-M. 1997, *ApJ*, 480, 36
- [143] Thoul, A. A. & Weinberg, D.H. 1995, *ApJ*, 442, 480
- [144] Tormen, G. , Bouchet, F. R., & White, S. D. M. 1997, *MNRAS*, 286, 865
- [145] Turner, E. L., Ostriker, J. P., & Gott, J. R. 1984, *ApJ*, 284, 1

- [146] Tyson J.A., Kochanski, G.P., & Dell'Antonio I.P. 1998, ApJ, 498, L107
- [147] Tyson, J. A., Wenk, R. A., & Valdes, F. 1990, ApJ, 349, L1
- [148] Valinia, A., Shapiro, P.R., Martel, H., Vishniac, E.T. 1997, ApJ, 479, 46
- [149] van den Bosch, F. C. 2002, MNRAS, 331, 98
- [150] Wechsler R.H., Bullock, J.S., Primack, J.R., Kravtsov, A.V., & Dekel, A. 2002, ApJ, 568, 52
- [151] Williams, L. L. R., Navarro, J. F., & Bartelmann, M. 1999, ApJ, 527, 535
- [152] Wright, C. O., & Brainerd, T. G. 2000, ApJ, 534, 34
- [153] Wyithe, J. S. B., Turner, E. L., & Spergel, D. N. 2001, ApJ, 555, 504
- [154] Yoshida, N., Springel, V., White, S. D. M. & Tormen, G. 2000, ApJ, 544, L87
- [155] Young, P., Gunn, J. E., Kristian, J., Oke, J. B., & Westphal, J. A. 1980, ApJ, 241, 507
- [156] Zhao, D.H., Mo, H.J., Jing, Y.P., & Borner, G., 2003, 339, 12

This figure "fig1a.jpg" is available in "jpg" format from:

<http://arxiv.org/ps/astro-ph/0409173v1>